

MICROSEISMIC UNIVERSITY OF OKLAHOMA FRACTURES

GRADUATE COLLEGE

A THESIS APPROVED FOR THE
MEWBURN'S SCHOOL OF PETROLEUM AND GEOLOGICAL ENGINEERING

MICROSEISMIC MAPPING OF HYDRAULIC FRACTURES


A THESIS

SUBMITTED TO THE GRADUATE FACULTY

in partial fulfillment of the requirements for the

Degree of

MASTER OF SCIENCE



Dr. Carl H. Sondergeld, Chair



Dr. Chandra S. Rai

By


IROH ISAAC ASO

Norman, Oklahoma

2009

Dr. Richard F. Sigal

BU
THESIS
ASO
Cop. 2

MICROSEISMIC MAPPING OF HYDRAULIC FRACTURES

A THESIS APPROVED FOR THE
MEWBOURNE SCHOOL OF PETROLEUM AND GEOLOGICAL ENGINEERING

BY

[REDACTED]

Dr. Carl H. Sondergeld, Chair

[REDACTED]

Dr. Chandra S. Rai

[REDACTED]

Richard F. Sigal

© Copyright by IIR

All Rights Reserved.

To the Most High God,

the Beginning and End,

of all knowledge.

© Copyright by IROH ISAAC ASO 2009

All Rights Reserved.

ACKNOWLEDGEMENTS

I will like to express my profound gratitude to the chairman (Dr. Carl Sondergeld) and members (Dr. Chander Rai and Richard Siegal) of my thesis committee for allowing me to use the Integrated Core Characterization Center (IC³) research group and providing me with resources and support to complete my successful completion of my thesis. I also thank the staff of IC³ - Gary Speers, Scott Hymowitz, and others for letting me set up my experiments and providing valuable technical assistance throughout the course of my work. I thank Mohammed Yassin for his assistance with scanning electron microscopy and constructive critiques of my work, and thank my colleagues at the research group for being like brothers and sisters to me.

To the Most High God,
the Beginning and End
of all knowledge.

Also, I am grateful to the entire members of staff and faculty of the Petroleum Engineering School of Petroleum and Geological Engineering (MPGEE), especially those that have taught me. Specifically, I will like to mention Dr. Rogers - for introducing me to rock mechanics - and Dr. Shah - for teaching me reservoir characterization. The two fields of study were helpful for me as I embarked on my thesis research.

Last but not least, I thank my family and friends for their support and encouragement throughout my academic program.

ACKNOWLEDGEMENTS

I will like to express my profound gratitude to the chairman (Dr. Carl Sondergeld) and members (Drs. Chandra Rai and Richard Sigal) of my thesis committee for admitting me into the Integrated Core Characterization Center (IC³) research group and providing me with the resources and support I needed for the successful completion of this work. I also thank the staff of IC³ - Gary Stowe, Bruce Spears and Luis Hernandez – for helping set up my experiments and providing valuable technical support at every juncture of my work. I thank Mohammed Yasser for his assistance with scanning electron microscopy and constructive critiques of my work. I also thank my colleagues at the research group for being like brothers and sister to me.

Also, I am grateful to the entire members of staff and faculty of the Mewbourne School of Petroleum and Geological Engineering (MPGE), especially those that have taught me. Specifically, I will like to mention Dr. Roegiers - for introducing me to rock mechanics - and Dr. Shah - for teaching me reservoir stimulation. The two fields of study were helpful for me as I embarked on my thesis research.

Last but not least, I thank my family and friends for their support and encouragement throughout my academic program.

TABLE OF CONTENTS

Acknowledgements	iv
Table of contents	v
List of table	vii
List of figures	viii
Abstract	xiii
1. Introduction	1
1.1 Background	1
1.2 Motivation	4
1.3 Research objectives	6
1.4 Synopsis	7
2. Hydraulic fracturing and microseismicity	8
2.1 In situ stresses in rocks	8
2.2 Hydraulic fracture mechanics	10
2.3 Hydraulic fracture propagation models	17
2.3.1 Two-dimensional (2D) models	17
2.3.2 Three-dimensional (3D) models	22
2.4 Rock failure mechanisms	22
2.5 Basic theory of microseismicity in rocks	24
2.5.1 Description of microseismic sources.....	25
3. Experimental methodology.....	33
3.1 Equipment and materials.....	33
3.1.1 Pumping unit.....	33
3.1.2 Fluid system.....	34
3.1.3 Acoustic emission (AE) monitoring system.....	34
3.2 Sample characterization.....	39
3.2.1 Circumferential velocity analysis (CVA)	39

3.2.2	Porosity measurement.....	43
3.2.3	Permeability measurement.....	45
3.2.4	Mineralogy measurement.....	45
3.3	Experimental procedure.....	47
3.4	Assessment of fracture morphology.....	61
4.	Results and analyses.....	62
4.1	Pressure and AE responses during fluid injection.....	62
4.2	Analyses of experiment results.....	71
4.2.1	AE event location.....	71
4.2.2	Spatio-temporal determination of permeability from microseismicity.....	81
4.2.3	Focal mechanism solutions (FMS).....	85
4.2.4	Spectral analyses of AE signals.....	102
4.2.5	Source parameters of acoustic emission.....	107
4.2.6	Hydraulic fracture morphology (SEM).....	118
	Conclusion.....	129
	Reference.....	131
	Appendix A.....	140
	Appendix B.....	143
	Table 4.1: Summary of fault parameters for 9 shear AE events associated with experiment 4.....	99
	Table 4.2: Summary of fault parameters for 8 shear AE events and one cluster associated with experiment 7.....	101
	Table 4.10: Summary of fault parameters for 4 shear AE events associated with experiment 8.....	102
	Table 4.11: Summary of fracturing mechanisms for experiments 1-4, 7 & 8.....	103
	Table 4.12: Summary of fracturing mechanisms of shear AE events.....	103

LIST OF TABLES

Table 3.1: Results of circumferential velocity analysis (CVA) of sample E1 – E8.....	43
Table 3.2: Petrophysical and elastic properties of sample E1 – E8.....	46
Table 3.3: FTIR mineralogical compositions of samples E1 to E8 in weight percentages.....	47
Table 3.4: Completion data for hydraulically fractured samples.....	48
Table 3.5: Locations of AE sensor on samples.....	50
Table 3.6: Locations of pencil lead breaks for AE system calibration in Cartesian and cylindrical coordinates.....	52
Table 4.1: Summary of breakdown pressures and number of AE induced during the hydraulic fracturing of samples E1 to E8.....	71
Table 4.2: Deviations of hydraulic fractures from preexisting crack orientations	83
Table 4.3: Parameters for computing permeability, k^* from AE and their results.....	85
Table 4.4: Model parameters and correlation coefficient, R^2 , of the CVA results for samples E1 – E4, E7 and E8.....	89
Table 4.5: summary of fault parameters for 18 shear AE events and 3 clusters associated with experiment 1.....	95
Table 4.6: summary of fault parameters for 3 shear AE events associated with experiment 2.....	96
Table 4.7: Summary of fault parameters for 3 shear AE events associated with experiment 3.....	97
Table 4.8: Summary of fault parameters for 9 shear AE events associated with experiment 4.....	99
Table 4.9: Summary of fault parameters for 8 shear AE events and one cluster associated with experiment 7.....	101
Table 4.10: Summary of fault parameters for 4 shear AE events associated with experiment 8.....	102
Table 4.11: Summary of fracturing mechanisms for experiments 1-4, 7 & 8	103
Table 4.12: Summary of faulting mechanisms of shear AE events	103

LIST OF FIGURES

Figure 2.1: Principal stresses on an element of rock mass at a depth.....	8
Figure 2.2: Stress Components on the borehole wall (Daneshy, 1973).....	10
Figure 2.3: Orientation of a wellbore relative to principal stresses, σ_1 , σ_2 and σ_3	13
Figure 2.4: Static pressurized penny-shaped crack of radius, R	18
Figure 2.5: PKN model (Mack and Warpinski, 2000).....	20
Figure 2.6: KGD model (Mack and Warpinski, 2000).....	21
Figure 2.7: Mohr circle representation.....	23
Figure 2.8: Opening, sliding and tearing modes of crack propagation (Martin and Valko, 2007).....	24
Figure 2.9: Internal discontinuity in a rock of volume, V bounded by a surface, Σ	27
Figure 2.10: Couples on the Cartesian coordinate system constituting the seismic moment tensor.....	29
Figure 2.11: Fault geometry in a geographical coordinate system for earthquake studies.....	30
Figure 2.12: Basic fault geometry and beach ball representations (source: http://geology.about.com/library/bl/blbeachball.htm).....	33
Figure 3.1: Quizix TM SP-5200 pumping unit used for hydraulic fracturing experiments.....	34
Figure 3.2: Broadband acoustic emission transducer (B1025).....	36
Figure 3.3: calibration of AE transducer (B1025).....	36
Figure 3.4: Field Module (FM-1 TM) unit manufactured by Digital Wave®, Inc.....	37
Figure 3.5: ICS-645 Simplified block diagram (modified from DaqScribe Technology, Inc., 2003).....	38
Figure 3.6: Block diagram of AE monitoring system.....	39
Figure 3.7: Schematic of circumferential velocity analysis (CVA) showing the P-wave piezoelectric transducers (hatched portions) located diametrically across a sample.....	40
Figure 3.8: Apparatus for circumferential velocity analysis (CVA).....	41
Figure 3.9: CVA results of sample E1 – E8.....	43

Figure 3.10: Automatic Klinkenberg permeameter/porosimeter (AP-608) for measuring sample porosity and permeability as a function of confining pressure up to 10, 000 psi..	44
Figure 3.11: Boyle's law method of porosity determination. Rock sample is placed inside the rubber boot and pressurized (Cone and Kersey, 1992).....	45
Figure 3.12: Apparatus for the measuring mineral composition.....	47
Figure 3.13: Samples under preparation before hydraulic fracturing.....	48
Figure 3.14: 3-D plan and side views of a 4-in diameter sample completed with 0.12 in ID mini-casing.....	49
Figure 3.15: Plan view of the interconnections between rock sample, bronze button and AE transducer.....	50
Figure 3.16: Hsu-Nielson source for the testing and calibration of acoustic emission systems (source: http://www.ndt.net/ndtaz/ndtaz.php).....	52
Figure 3.17: Location of AE due to pencil lead breaks on sample E1.....	53
Figure 3.18: Location of AE due to pencil lead breaks on sample E2.....	54
Figure 3.19: Location of AE due to pencil lead breaks on sample E3.....	55
Figure 3.20: Location of AE due to pencil lead breaks on sample E4.....	56
Figure 3.21: Location of AE due to pencil lead breaks on sample E5.....	57
Figure 3.22: Location of AE due to pencil lead breaks on sample E6.....	58
Figure 3.23: Location of AE due to pencil lead breaks on sample E7.....	59
Figure 3.24: Location of AE due to pencil lead breaks on sample E8.....	60
Figure 3.25: Event 3 of lead break (on aluminum surface) to check the polarity of the 16 B1025 AE sensors.....	61
Figure 3.26: 1-inch diameter cores drilled through fractured samples.....	62
Figure 4.1: Experiment 1. Fluid injection rate, pump pressure and cumulative AE events (106) as functions of time during the hydraulic fracturing of sample E1 (oil-fractured)..	63
Figure 4.2: Experiment 2. Fluid injection rate, pump pressure and cumulative AE events (50) as functions of time during the hydraulic fracturing of sample E2 (Water-fractured).....	64

Figure 4.3: Experiment 3. Fluid injection rate, pump pressure and cumulative AE events (50) as functions of time during the hydraulic fracturing of sample E3 (Water-fractured).....	65
Figure 4.4: Experiment 4. Fluid injection rate, pump pressure and cumulative AE events (120) as functions of time during the hydraulic fracturing of sample E1 (oil-fractured).....	66
Figure 4.5: Experiment 5. Fluid injection rate, pump pressure and cumulative AE events (395) as functions of time during the hydraulic fracturing of sample E5 (oil-fractured).....	67
Figure 4.6: Experiment 6. Fluid injection rate, pump pressure and cumulative AE events (98) as functions of time during the hydraulic fracturing of sample E6 (Water-fractured).....	68
Figure 4.7: Experiment 7. Fluid injection rate, pump pressure and cumulative AE events (115) as functions of time during the hydraulic fracturing of sample E7 (oil-fractured).....	69
Figure 4.8: Experiment 8. Fluid injection rate, pump pressure and cumulative AE events (80) as functions of time during the hydraulic fracturing of sample E8 (water-fractured).....	70
Figure 4.9: Factors controlling breakdown pressure	72
Figure 4.10: Plan and side views of AE events (48/106) induced in sample E1 during hydraulic fracturing experiment. Darks lines define sample outlines.....	75
Figure 4.11: Plan and side views of AE events (13/50) induced in sample E2 during hydraulic fracturing experiment.....	76
Figure 4.12: Plan and side views of AE events (10/50) induced in sample E3 during hydraulic fracturing experiment.....	77
Figure 4.13: Plan and side views of AE events (14/120) induced in sample E4 during hydraulic fracturing experiment.....	79
Figure 4.14: plan and side views of AE events (10/115) induced in sample E7 during hydraulic fracturing experiment.....	81
Figure 4.15: plan and side views of AE events (16/80) induced in sample E8 during hydraulic fracturing experiment.....	82
Figure 4.16: Plots of microseismic (AE) forward fronts enveloping their respective distances from AE sources in samples E1 – E4, E7 and E8 to the points of fluid injection.....	85

Figure 4.17: Sinusoidal variations of compressional waves around the circumferences of samples E1 – E4, E7 and E8.....	89
Figure 4.18: Plan and side views showing azimuth and take-off angle of a seismic ray with respect to a receiver (i.e. sensor) within a cylindrical core sample.....	90
Figure 4.19: Typical AE waveforms from experiment 1 showing upward/compression (left) and downward/dilatation (right) P-wave first motion.....	91
Figure 4.20: Focal mechanism solutions of AE events (48) from sample E1 showing tensile (9), shear (18) and complex (21) events.....	92
Figure 4.21: Composite focal mechanism solutions of AE events from sample E1 showing normal, thrust and dip-slip faulting for clusters E1_A, E1_B and E1_C, resp...	94
Figure 4.22: Focal mechanism solutions of AE events (13) from sample E2 showing tensile (2), shear (3) and complex (8) events.....	96
Figure 4.23: Focal mechanism solutions of AE events (10) from experiment 3 showing tensile (7) and shear (3) events.....	97
Figure 4.24: Focal mechanism solutions of AE events (14) from experiment 4 showing tensile (2), shear (9) and complex (3) events	98
Figure 4.25: Focal mechanism solutions of AE events (10) from sample E7 showing shear (8) and complex (2) events.....	100
Figure 4.26: Composite focal mechanism solutions of two AE events (no. 10 and 13) from experiment 7, separated by a distance of 8 mm, showing left-lateral strike-slip with thrust faulting component.....	100
Figure 4.27: Focal mechanism solutions of AE events (16) from sample E8 showing tensile (6), shear (4) and complex (5) and compressive events.....	102
Figure 4.28: Composite focal mechanism solutions of all the AE events associated with the hydraulic fracturing of samples E1 – E4, E7 and E8.....	104
Figure 4.29: Power spectra of early portions of event 8 of experiment 1.....	105
Figure 4.30: (a) The amplitude of event 15, experiment 1, varies as the location of the sensor and (b) the Frequency content of event 15, experiment 1, and varies as the location of the sensor.....	106
Figure 4.31: Frequency content of power spectra of the P-wave portion of AE induced during the hydraulic fracturing of samples E1-E4, E7 and E8.....	106
Figure 4.32: Plot of the amplitude against the primary frequency of all the shear AE events shows a linear relationship.....	107

Figure 4.33: Plot of displacement against peak amplitude of all the shear AE events shows an exponential relationship.....	108
Figure 4.34: Theoretical displacement spectral density showing high and low frequency asymptotes.....	109
Figure 4.35: Spectral densities of AE signals associated with event 15 of experiment 1.....	112
Figure 4.36: Plots of AE against source parameters of AE shear events associated with experiment 1.....	113
Figure 4.37: Plots of AE against source parameters of AE shear events associated with experiment 2.....	114
Figure 4.38: Plots of AE against source parameters of AE shear events associated with experiment 3.....	115
Figure 4.39: Plots of AE against source parameters of AE shear events associated with experiment 4.....	116
Figure 4.40: Plots of AE against source parameters of AE shear events associated with experiment 7.....	117
Figure 4.41: Plots of AE against source parameters of AE shear events associated with experiment 8.....	118
Figure 4.42: Source parameters of AE shear events associated with experiments 1 – 4, 7 and 8.....	119
Figure 4.43: Post-fracture SEM images of Experiment 1 .	121
Figure 4.44: Post-fracture SEM images of Experiment 2 .	123
Figure 4.45: Post-fracture SEM images of Experiment 3 .	124
Figure 4.46: Post-fracture SEM images of Experiment 4 .	125
Figure 4.47: Post-fracture SEM images of Experiment 7 .	127
Figure 4.48: Post-fracture SEM images of Experiment 8 .	128

ABSTRACT

Since the advent of hydraulic fracturing as a proven technique for reservoir stimulation, efforts have been made, using empirical and analytical tools, to understand hydraulic fracturing. These efforts have not been entirely successful, and inaccurate hydraulic fracture evaluation remains a problem in the industry. In this study the results of hydraulic fracturing of unconfined 4-inch diameter cylindrical carbonate core samples using water or mineral oil are presented. With a simple laboratory procedure samples were pressurized to failure and associated acoustic emissions analyzed. The breakdown pressures could be associated with the level of AE activity and are functions of treatment fluid viscosity and sample permeability. The hydraulic fractures are not caused by simple tensional failure, and so result in the hydraulic fractures being non-planar at some scale. The microfracturing processes possess overlapping frequency bands between 39 and 391 KHz. Source parameters like stress drops and average displacements of individual shear events are small. Source radii are several orders of magnitude greater than the average grain size. The observations are consistent with the reactivation of pre-existing flaws.

1 INTRODUCTION

1.1 Background

Commercial production from most gas reservoirs in low-permeability formations is achieved through hydraulic fracture stimulation. In this technique, fluids are injected into a wellbore at such a rate that the wellbore pressure overcomes the strength of the rock as well as the minimum closure stress. The first commercial experiment was performed in 1947 at the Hugoton gas field in Grant County, Western Kansas, United States (Howard and Fast, 1970). Hydraulic fracturing has since been used in many well stimulation and completion programs. Clark (1949) pointed out that pumping the fluid at a rate higher than the rate at which the treatment fluid permeates the formation is a necessary condition for hydraulic fractures to occur.

Hydraulic fracturing treatment is conducted in at least four stages – pre-pad, pad, proppant-laden and flush. The pre-pad stage, requiring about 10 percent of the total treatment volume, functions to initiate a fracture and cool the formation down to a reasonable temperature. Cooling is necessary in order to preserve the properties of the fracturing fluids. In the pad stage a more viscous fluid (about 40 percent of the entire treatment volume) is injected into the initiated fracture in order to extend it to the desired dimensions. In the proppant-laden stage, propping agents (sands, pellets, metal shot, glass beads, walnut shells, etc.) are blended with about 40 percent of the total treatment fluid volume to form a slurry mix and pumped into the fracture. The purpose is to ‘prop’ the fracture and keep it from closing when the treatment is terminated. The last stage is the flush stage. A relatively thin fluid (making up 10 percent of the entire treatment volume,

just like the pre-pad stage) is pumped downhole in order to completely displace residual proppant from the wellbore. After the slurry is flushed into the fracture, the treatment is terminated and the well shut-in for a while and then 'flowed back' to eject treatment fluids left in the fracture and wellbore. Often, gel breakers are added to reduce fluid viscosity so that it can be easily pumped out of the fracture. However, the fluid volumes used in these stages or the entire treatment program can be modified depending on the application of the hydraulic fracture treatment.

Based on applications, Zeng (2002) divided the evolution of the hydraulic fracturing technology into generations. The first generation held sway in the 1960s and was intended to overcome near-wellbore formation damaged caused by drilling and completion operations. The second generation is the massive hydraulic fracture treatment which was used extensively in low permeability formations. The process produced long fractures and was made economically viable during the 1970s. The third generation application was the 'frac and pack' technology applied in high permeability formations for the purpose of sand production control. Here, proppant slurry is pumped into an already fractured formation so that its fluid leaks into the formation to form a tip screen out. Regardless of the particular application of hydraulic fracture treatment, it is extremely important to know the dimensions (fracture half length, width, and height), orientations and shapes of the created hydraulic fractures for the purposes of treatment optimization and reservoir management (well spacing and field layout). These data will also help in determining the concentration and volume of proppant needed to keep the hydraulic fractures from closing when treatment is terminated.

Several analytical techniques have been applied to determine the dimensions (fracture half length, width, and height) and azimuths of hydraulic fractures. Hydraulic fracture simulators predict fracture geometry prior to treatment. Their computations are based on either the 2D or 3D linear elastic models. Other methods of determining hydraulic fracture dimensions include the use of radioactive tracers, temperature logs, well testing, production analyses, tiltmeters and microseismic mapping (Zeng, 2002). Excellent reviews of these diagnostic techniques are provided by Hill et al. (1994) and Warpinski (1996). Microseismic mapping has been judged one of the most accurate in defining fracture dimensions, azimuth, and symmetry.

Microseismic mapping deals with the acquisition and analysis of acoustic emissions (also known as microseismic activities, microseisms or micro-earthquakes) signals. In geological materials, acoustic emissions can be associated with shear slippage along planes of weakness, fluid leak-off or creation of new cracks. Sleepe et al. (1995) suggests that in hydraulic fracturing, most of the acoustic emission (AE) events are due to shear failure resulting from the pressurization of fractures as well as formation pore pressure influences. However, under similar conditions, tensile, compressive and more complex failure mechanisms have been observed in hydraulic fractures (Matsunaga et al., 1993; Sasaki, 1998; Ishida et al., 2004). Energy from the microseismic source contains direct shear and compressional waves as well as converted shear and compressional waves. This energy leaves the source, propagates through the medium and is detected by a suitable resonant or broadband transducer/sensor. Along the ray path, the seismic waves undergo such effects as attenuation (a reduction in the amplitude of the wave due to loss of energy), scattering, refraction, reflection and mode conversions. Thus, the transducer

detects signals that have been modified or filtered by the formation and its geometry. For microseismic mapping, the direct compressional wave (P-wave) is the first phase to arrive at the sensor. On a typical signal, the P-wave can be seen as emerging from the background with a positive or negative polarity, depending on the polarity response of the sensor and its relative location with respect to the event source (Cornet and Julien, 1989). The shear wave component arrives later having larger amplitude, phase difference of 90° (relative to the direct p-wave) and different (generally lower) center frequency. Shear waves could be obscured by the effects of reflections and refractions due to their late arrival (Sleepe et al., 1995). Thus, the signal detected by the transducer is a complex superposition of many seismic phases. A diligent analysis of the properties of this signal is necessary in order to determine the hypocenters - the source of acoustic emission within a stressed medium – as well as the frequency content and focal mechanism solutions of microseismic events.

1.2 Motivation

Accounts by some researchers (Fall et al., 1992; Matsunaga et al., 1993) have shown that failure modes of rocks during hydraulic fracturing are complex. Fall et al. (1992) performed hydraulic fracturing on two unconfined Lac Du Bonnet Grey granites and reported that the associated acoustic emissions could be modeled as double-couple (shear failure), tensile (all positive P-wave motion first arrivals), compressive sources (all negative P-wave motion first arrivals) and complex sources (positive and negative P-wave motion first arrivals that do not fit the double-couple model). Matsunaga et al. (1993) went on to examine the effects of fluid viscosity, grain size and rock minerals on hydraulic fracturing mechanism on samples of bi-axially stressed acrylic resin, Inada

granite, Akiyoshi marble and Komatsu andesite. Using water (1-cp viscosity) and oil (70-cp viscosity), they observed that the 'water frac' had less microseismic activity than the 'oil frac' and the AE source locations were aligned in the direction of the maximum imposed stress. They also reported that samples fractured with water showed shear failure except in the non-permeable acrylic resin which displayed tensile failure. Samples fractured with oil show both shear and tensile failure mechanisms. Thin-section analyses revealed that fracture apertures with oil as the fracturing fluid were larger than those fractured with water. Similar experiments conducted by Ishida et al. (2004), revealed that shear events dominated fracture mechanisms in a pressurized sleeve (no fluid flow into rock samples). Sasaki (1998) monitored seismicity during an experiment at the Hijiori hot dry rock site and suggested that hydraulically induced microseismicity could be due to shear failure resulting from high fluid pressure on planes of weakness surrounding a main hydraulic fracture. He determined the focal mechanism solutions of 12 events and found their average pressure axis direction to correlate with both the event hypocentral distribution and the maximum horizontal stress. Cornet and Julien (1989) tried to determine the stress field in the granite massif of Le Mayet de Montagne by inverting the focal mechanisms of microseismic events but were only successful in 14 out of about 102 events. The results obtained from these inversions did not agree with local tectonics. They attributed failure of their attempts to stress heterogeneities as well as fluid-induced stress perturbations in the region.

Some other complexities in the form of multiple hydraulic fracture initiation and asymmetry have also been observed on several treatments (Warpinski et al., 1982; Weijers et al., 2000). Asymmetry in hydraulic fracture geometry, which is a situation

where one arm is longer than the other, negatively impacts hydrocarbon production and proppant transport (Bennett et al., 1983).

It is clear from the foregoing that, while the physics of hydraulic fracturing is fairly well understood from macro stress analysis, the micro-fracturing mechanisms leading ultimately to such 'macro-fractures' remain undefined. Also, the disparity between observed hydraulic fractures and those predicted by mathematical models raises serious concerns regarding hydraulic fracture optimization, reservoir management and its environmental impact. Thus, the industry needs efficient diagnostic tools for mapping hydraulic fractures (Zeng, 2002) in order to increase well productivity and avoid possible health and environmental hazards resulting from uncontained hydraulic fracture growths.

1.3 Research Objectives

From the previous sections, hydraulic fractures are seen as being so complex that their fracturing mechanisms are not easily defined. It is the aim of this experimental investigation to explore such fracturing mechanisms by pressurizing eight unconfined carbonate samples with either mineral oil or water until failure, and recording and locating the associated acoustic emissions. The focal mechanism solutions, frequency content and source parameters of the acoustic emissions were analyzed. The hydraulic fracture morphologies are studied in a scanning electron microscope. Results are correlated and inferences drawn about the hydraulic fracturing mechanisms.

1.4 Synopsis

This thesis is presented in 5 chapters.

Chapter 1 is a short description of hydraulic fracturing technology and acoustic emissions. It also presents the objectives of this research.

Chapter 2 reviews the theoretical bases of hydraulic fracturing and microseismicity. It discusses the mechanics of field-scale hydraulic fracturing and its applicability of microseismic monitoring in mapping the geometries of induced hydraulic fractures.

Chapter 3 describes the experimental methodology as well as apparatus and procedures employed in the experiments.

Chapter 4 presents the results of the experiments, the analysis procedures adopted and their engineering and scientific implications.

Chapter 5 provides conclusions and presents the benefits and applications of this research to the efficient mapping of hydraulic fractures.

2 HYDRAULIC FRACTURING AND MICROSEISMICITY

2.1 In Situ Stresses in Rocks

The in situ state of stress controls hydraulic fracturing. At any point in the subsurface the stress conditions can be represented with three orthogonal principal stresses. The three principal stresses are vertical stress (σ_v) and two horizontal stresses (σ_H and σ_h) as shown in Figure 2.1.

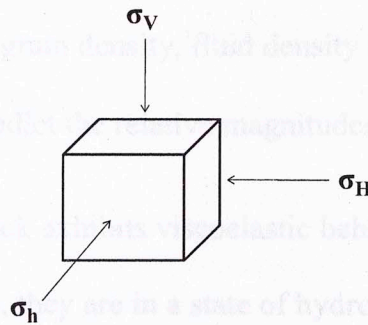


Figure 2.1: Principal stresses on an element of rock mass at a depth.

The magnitudes and directions of these principal stresses are affected by topography, tectonic forces, constitutive behavior and local geological history of the rock (Jaeger, et al., 2007).

The vertical stress is generally taken to be the overburden stress assuming there is no shear stress at the surface.

$$\sigma_v = \int_0^z \rho(z) g dz \quad (2.1)$$

where ρ , g , and z are rock density, acceleration due to gravity, and depth, respectively.

For shallow depth, $\rho(z)$ can be assumed to be independent of z and we have the approximation,

$$\sigma_v = \rho g z \quad (2.2)$$

density, ρ , is given by:

$$\rho = \rho_g (1 - \phi) + \rho_f \phi \quad (2.3)$$

where ρ_g , ρ_f and ϕ are the rock grain density, fluid density and porosity, respectively.

Some of the models used to predict the relative magnitudes of these stresses are:

- a. Heim's model: If the rock exhibits viscoelastic behavior, then all the principal stresses are equal. Thus, they are in a state of hydrostatic stress. The shortcoming of this model is that it does not account for tectonic forces or the possibility of brittle behavior of near surface rocks (Jaeger et al., 2007).
- b. Uniaxial Strain model: This model assumes that if the rock mass is constrained against lateral deformation after the weight of the rock is applied instantaneously the two horizontal stresses are equal and functions of the vertical stress. Assuming the rock is isotropic and no shear stresses, we have,

$$\sigma_H = \sigma_h = \frac{\nu}{1 - \nu} \sigma_v \quad (2.4)$$

where ν is the Poisson's ratio.

- c. Unconstrained Lateral Deformation model: This model assumes that the weight of the rock mass acts instantaneously and the rock experiences no lateral stresses

from that instant of time. Thus, the shear stresses as well as the horizontal stresses are zero.

2.2 Hydraulic Fracture Mechanics

Section 2.1 discusses different models used to represent the state of stress underground. However, if the geometry of the rock is altered by drilling and pressurizing a borehole, the stress concentration in the vicinity of the borehole will change significantly. Assuming an isotropic, homogenous and linearly elastic formation in which a circular hole of infinite length is drilled and fluid-pressurized, the state of stress at a point, r from the center of the wellbore (see Figure 2.2) is given by the general solutions for the plane strain condition and without fracturing fluid permeation into the formation (Kirsch, 1898; Hubbert and Willis, 1957; Haimson and Fairhurst, 1969; and Daneshy, 1973).

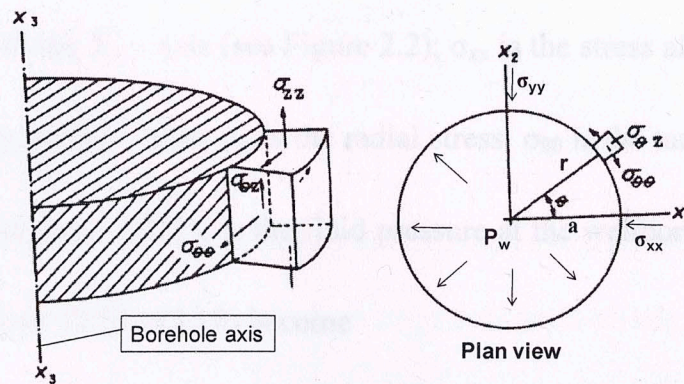


Figure 2.2: Stress components on the borehole wall (Daneshy, 1973). $\sigma_{\theta\theta}$ is the hoop or tangential stress.

$$\sigma_{rr} = \left[\begin{array}{l} 0.5(\sigma_{xx} + \sigma_{yy}) \left(1 - \frac{a^2}{r^2} \right) + 0.5(\sigma_{xx} - \sigma_{yy}) \left(1 + 3\frac{a^4}{r^4} - 4\frac{a^2}{r^2} \right) \cos 2\theta \\ + \tau_{xy} \left(1 + 3\frac{a^4}{r^4} - 4\frac{a^2}{r^2} \right) \sin 2\theta \end{array} \right] + \left[\frac{P_w a^2}{r^2} \right] \quad (2.5)$$

$$\sigma_{\theta\theta} = \begin{bmatrix} 0.5(\sigma_{xx} + \sigma_{yy})\left(1 - \frac{a^2}{r^2}\right) - 0.5(\sigma_{xx} - \sigma_{yy})\left(1 + 3\frac{a^4}{r^4}\right)\cos 2\theta \\ + \tau_{xy}\left(1 + 3\frac{a^4}{r^4}\right)\sin 2\theta \end{bmatrix} - \left[\frac{P_w a^2}{r^2} \right] \quad (2.6)$$

$$\sigma_{zz} = \left[\sigma_z - 2\nu(\sigma_{xx} - \sigma_{yy})\frac{a^2}{r^2}\cos 2\theta - 4\nu\tau_{xy}\frac{a^2}{r^2}\sin 2\theta \right] \quad (2.7)$$

$$\tau_{r\theta} = \left[0.5(\sigma_{xx} + \sigma_{yy})\left(1 - 3\frac{a^4}{r^4} + 2\frac{a^2}{r^2}\right)\sin 2\theta + \tau_{xy}\left(1 - 3\frac{a^4}{r^4} + 2\frac{a^2}{r^2}\right)\cos 2\theta \right] \quad (2.8)$$

$$\tau_{\theta z} = \left[(-\tau_{xz}\sin\theta + \tau_{yz}\cos\theta)\left(1 + \frac{a^2}{r^2}\right) \right] \quad (2.9)$$

$$\tau_{rz} = \left[(\tau_{xz}\cos\theta + \tau_{yz}\sin\theta)\left(1 - \frac{a^2}{r^2}\right) \right] \quad (2.10)$$

where a is the borehole radius; r is the radial distance from the center of the borehole; θ is the angle r makes with the X_1 - axis (see Figure 2.2); σ_{xx} is the stress along the X_1 - axis; σ_{yy} is the stress along the X_2 - axis; σ_{rr} is the radial stress; $\sigma_{\theta\theta}$ is the tangential stress; $\tau_{r\theta}$, $\tau_{\theta z}$ and τ_{rz} are shear stresses; and P_w is the fluid pressure at the wellbore. At the wellbore wall, $r = a$ and equations (2.5) – (2.10) become

$$\sigma_{rr} = P_w \quad (2.11)$$

$$\sigma_{\theta\theta} = (\sigma_{xx} + \sigma_{yy} - P_w) - 2(\sigma_{xx} - \sigma_{yy})\cos(2\theta) + 4\tau_{xy}\sin(2\theta) \quad (2.12)$$

$$\sigma_{zz} = \left[\sigma_z - 2\nu(\sigma_{xx} - \sigma_{yy}) \frac{a^2}{r^2} \cos 2\theta - 4\nu\tau_{xy} \frac{a^2}{r^2} \sin 2\theta \right] \quad (2.13)$$

$$\tau_{r\theta} = 0 \quad (2.14)$$

$$\tau_{\theta z} = \left[2(-\tau_{xz} \sin \theta + \tau_{yz} \cos \theta) \right] \quad (2.15)$$

$$\tau_{rz} = 0 \quad (2.16)$$

Fracture is initiated at the wall of the wellbore when the tensile strength of the rock is overcome and the fracture propagates in a plane normal to the least principal stress (Hubbert and Willis, 1957). The principal stresses prevailing at the wall of the wellbore are given as (Daneshy, 1973)

$$\begin{aligned} \sigma_1 &= \sigma_{rr} = P_w \\ \sigma_2 &= \frac{1}{2} \left[\sigma_{\theta\theta} + \sigma_{zz} + \sqrt{(\sigma_{\theta\theta} - \sigma_{zz})^2 + 4\tau_{\theta z}^2} \right] \\ \sigma_3 &= \frac{1}{2} \left[\sigma_{\theta\theta} + \sigma_{zz} - \sqrt{(\sigma_{\theta\theta} - \sigma_{zz})^2 + 4\tau_{\theta z}^2} \right] \end{aligned} \quad (2.17)$$

where σ_1 is directed radially outwards; σ_2 is tangent to the borehole wall and inclined at an angle of γ to the borehole axis; and σ_3 is also tangent to the borehole wall but inclined to the borehole axis at an angle of $(90 - \gamma)$ as shown in Figure 2.3.

$$\gamma = \frac{1}{2} \tan^{-1} \left(\frac{2\tau_{\theta z}}{\sigma_{\theta\theta} - \sigma_{zz}} \right) \quad (2.18)$$

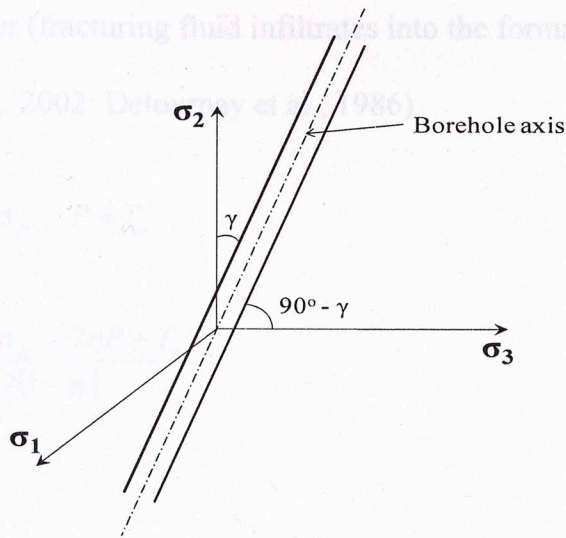


Figure 2.3: Orientation of a wellbore relative to principal stresses, σ_1 , σ_2 and σ_3 . The wellbore is in the $\sigma_2 - \sigma_3$ plane.

For a vertical wellbore, the hoop stress is distributed around the wellbore as a function of angle, θ . To determine the minimum value of the hoop stress, the value of θ at which the derivative of the hoop stress with respect to θ vanishes, is determined. This gives $\theta = 0$ or 180 degrees. Thus equation (2.12) becomes

$$\sigma_{\theta\theta(\min.)} = 3\sigma_{yy} - \sigma_{xx} - P_w \quad (2.19)$$

As the wellbore is pressurized, the effective tangential stress equals the tensile strength (T_o) of the rock. A vertical fracture is initiated when the breakdown pressure becomes

$$P_{cl} = 3\sigma_h - \sigma_H + T_o - P \quad (2.20)$$

where σ_h = minimum horizontal principal stress (σ_{xx}); σ_H = maximum horizontal principal stress (σ_{yy}); P = reservoir pressure; effective tangential stress, $[\sigma_{\theta\theta(\min)} - P] = -T_o$; and P_w = breakdown pressure (P_{cl}). According to Roegiers (1990) vertical fractures are induced at formation depths greater than 2000 ft where the minimum principal stress is horizontal. If the formation has a pore pressure, P , then the upper (no fracturing fluid infiltration into

the formation) and lower (fracturing fluid infiltrates into the formation) breakdown pressures, P_{c1} are (Zeng, 2002; Detournay et al., 1986)

$$P_{c1,upper} = 3\sigma_h - \sigma_H - P + T_o \quad (2.21)$$

$$P_{c1,lower} = \frac{3\sigma_h - \sigma_H - 2\eta P + T_o}{2(1-\eta)} \quad (2.22)$$

$$\eta = \frac{\alpha(1-2\nu)}{2(1-\nu)} \quad (2.23)$$

where η is the poroelastic stress coefficient; ν is the drained Poisson's ratio; and α is the Biot's coefficient which is equal to $1 - (K_{dry}/K_g)$. K_g and K_{dry} are the grain and dry porous frame bulk modulus of the formation, respectively. It is also possible to induce horizontal fractures when the overburden stress is the least principal stress. This usually occurs at formation depths that are less than 2000 ft (Roegiers, 1990) where the breakdown pressure is therefore equal to the overburden stress.

For finite cylindrical rock samples (similar to those used in this study) the boundary conditions and prevailing stress will differ somewhat from those presented by Haimson and Fairhurst (1969). Assuming a rock sample to be isotropic, homogeneous and linearly elastic, for a plane strain condition (i.e. $\epsilon_{zz} = 0$), the stresses induced due to fluid pressurization in a borehole, in the absence of confining pressure is given as (Timoshenko and Guder, 1975)

$$\begin{aligned}
\sigma_{rr} &= \frac{r_w^2}{r_e^2 - r_w^2} \left(1 - \frac{r_e^2}{r^2} \right) (P_w - P_o) \dots \dots \dots \text{compressive}; \\
\sigma_{\theta\theta} &= \frac{r_w^2}{r_e^2 - r_w^2} \left(1 + \frac{r_e^2}{r^2} \right) (P_w - P_o) \dots \dots \dots \text{tensile}; \\
\tau_{r\theta} &= 0; \text{ and} \\
\sigma_{zz} &= 2\nu \frac{r_w^2}{r_e^2 - r_w^2} (P_w - P_o) \dots \dots \dots \text{tensile}
\end{aligned}
\tag{2.24}$$

where r_w and r_e are the radii of the borehole and core sample, respectively; P_w and P_o are the borehole fluid pressure and formation pore pressure, respectively. By considering fluid permeation from the borehole into the sample, applying Lorenz solution for thermally induced stresses in a cylinder with a concentric circular borehole and substituting pressure for temperature, equation (2.24) can be expressed as (Serdyukov, 2000)

$$\begin{aligned}
\sigma_{rr} &= \frac{\alpha(1-2\nu)}{2(1-\nu)\ln\frac{r_e}{r_w}} \left[-\ln\frac{r_e}{r} - \frac{r_w^2}{r_e^2 - r_w^2} \left(1 - \frac{r_e^2}{r^2} \right) \ln\frac{r_e}{r_w} \right] (P_w - P_o) + P(r); \\
\sigma_{\theta\theta} &= \frac{\alpha(1-2\nu)}{2(1-\nu)\ln\frac{r_e}{r_w}} \left[1 - \ln\frac{r_e}{r} - \frac{r_w^2}{r_e^2 - r_w^2} \left(1 + \frac{r_e^2}{r^2} \right) \ln\frac{r_e}{r_w} \right] (P_w - P_o) + P(r); \\
\tau_{r\theta} &= 0; \text{ and} \\
\sigma_{zz} &= \frac{\alpha\nu(1-2\nu)}{2(1-\nu)\ln\frac{r_e}{r_w}} \left[1 - 2\ln\frac{r_e}{r} - \frac{2r_w^2}{r_e^2 - r_w^2} \ln\frac{r_e}{r_w} \right] (P_w - P_o)
\end{aligned}
\tag{2.25}$$

Where,

$$P(r) = (P_w - P_o) \frac{\ln(r_e/r)}{\ln(r_e/r_w)}$$

where α is the poroelastic constant and r is the radial coordinate. Superimposing solutions (2.24) and (2.25) we obtain the conditions for both vertical and horizontal fracture initiations as (Serdyukov, 2000)

$$\sigma_{\theta\theta} = (P_w - P_o) \left[2 \frac{r_e^2}{r_e^2 - r_w^2} - \alpha \frac{1-2\nu}{1-\nu} \left(\frac{r_e^2}{r_e^2 - r_w^2} - \frac{1}{2 \ln \frac{r_e}{r_w}} \right) \right] \dots \text{vertical} \quad (2.26)$$

where $\sigma_{\theta\theta} = T_1$ (horizontal tensile strength of the rock) and $(P_w - P_o) = P_{c1}$ (breakdown pressure) which yields a vertical fracture. Similarly,

$$\sigma_{zz} = (P_w - P_o) \left[\frac{r_e^2 - (1-2\nu)r_w^2}{r_e^2 - r_w^2} - \alpha \nu \frac{1-2\nu}{1-\nu} \left(\frac{r_e^2}{r_e^2 - r_w^2} - \frac{1}{2 \ln \frac{r_e}{r_w}} \right) \right] \dots \text{horiz.} \dots (2.27)$$

where $\sigma_{zz} = T_3$ (vertical tensile strength of the rock) and $(P_w - P_o) = P_{c3}$ (vertical breakdown pressure) which yields a horizontal fracture.

Although hydraulic fractures are initiated in tension, shear components have been observed in inclined wellbores (Daneshy, 1973) and in rocks (subject to plastic deformation) fractures are initiated due to shear (Papanastasiou et al., 1995). After the initiation of hydraulic fractures, another issue has to do with the propagation of these fractures away from the wellbore and into the formation. A number of models have been developed to predict the dimensions and geometries of the hydraulic fractures.

2.3 Hydraulic Fracture Propagation Models

Mathematical models have been developed to relate hydraulic fracture dimensions to treatment parameters, reservoir and fluid properties (Gidley et al., 1989). These models are necessary in performing economic optimization, designing fracturing fluid and slurry injection schedules, simulating hydraulic fracture geometry, proppant placement and evaluation of hydraulic fracturing programs (Mack and Warpinski, 2000). Generally, hydraulic fracturing models assume that reservoir rocks are homogeneous, isotropic and linearly elastic; in-situ stresses, reservoir pressure and formation properties are horizontally invariant; laminar flow of fluids in the hydraulic fracture; and stresses induced by fluid leak-off and thermal effects are negligible. The models are fundamentally divided into two - and three - dimensional models.

2.3.1 Two-Dimensional (2D) Models

Sneddon (1946) and Sneddon and Elliot (1946) used the theory of elasticity to determine the stress concentration and pressure associated with a static pressurized penny-shaped crack of radius, R as shown in Figure 2.4. The width (w) and volume (V) of the crack are related to the differential pressure, ΔP – difference between the internal pressure in the crack and the stress external to the crack.

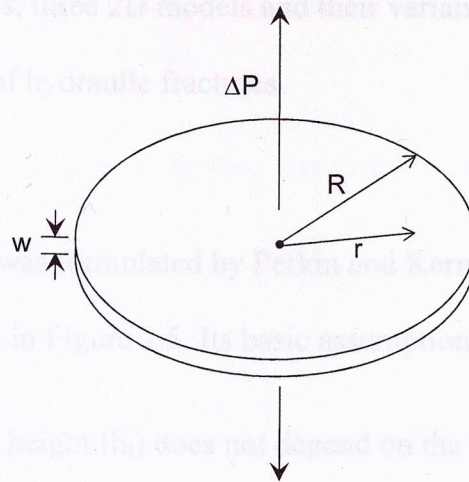


Figure 2.4: Static pressurized penny-shaped crack of radius, R. w is the width of the crack and ΔP is the differential pressure creating the crack.

$$w(r) = \frac{8\Delta PR(1-\nu^2)}{\pi E} \sqrt{1 - \left(\frac{r}{R}\right)^2} \quad (2.28)$$

$$V = \frac{16\Delta PR^3(1-\nu^2)}{3E} \quad (2.29)$$

where r is the outward distance from the center of the crack; ν and E are the Poisson's ratio and the Young's modulus of the pressurized medium, respectively. For a constant fracture height, h_f , and infinite fracture half length, x_f , Sneddon and Elliot (1946) determined the maximum fracture width to be

$$w = \frac{2\Delta P h_f}{E'} \quad (2.30)$$

where E' is the plane strain modulus which is given as

$$E' = \frac{E}{1-\nu^2} \quad (2.31)$$

Using the foregoing as basis, three 2D models and their variants have been developed for predicting the dimensions of hydraulic fractures.

(a) PKN Model:

This model was formulated by Perkin and Kern (1961) and Nordgren (1972) and depicted in Figure 2.5. Its basic assumptions are (Gidley et al., 1989):

- i. The fracture height (h_f) does not depend on the fracture half length (x_f).
- ii. The fracturing fluid pressure in the direction of fracture propagation is constant across the cross-sectional area perpendicular to direction of fracture propagation.
- iii. Each vertical section undergoes individual deformation.
- iv. Maximum fracture width, w , is given by

$$w(x) = \frac{(1 - \nu)h_f(P - \sigma_H)}{G} \quad (2.32)$$

where P is the fluid pressure in the fracture, σ_H is the maximum horizontal stress, G is the shear modulus, and ν is the Poisson's ratio of the formation.

- v. The pressure gradient from the vertical cross-section to the tip of the fracture is a function of the flow resistance in a narrow, elliptical path and based on Lamb (1932), it is given as

$$\frac{\partial(P - \sigma_H)}{\partial x} = -\frac{64q\mu}{\pi h_f w^3} \quad (2.33)$$

where q and μ are the fluid flow rate and viscosity, respectively.

vi. Fracture width and volume are given by

$$w(x,t) = w(x,0) \left(1 - \frac{x}{x_f}\right)^{\frac{1}{4}} \dots\dots\dots \text{Shape} \quad (2.34)$$

$$V = \frac{\pi}{5} x_f h_f w(0,t) = qt \dots\dots\dots \text{Volume}$$

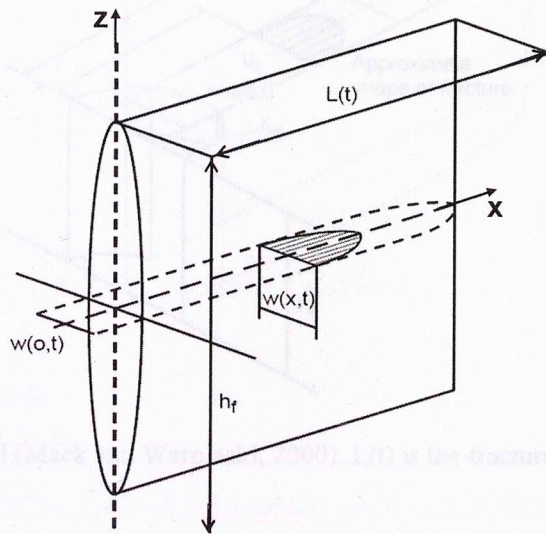


Figure 2.5: PKN model (Mack and Warpinski, 2000). $L(t)$ is the fracture half length, x_f .

(b) KGD Model

This model was proposed by Khristianovich, Geertsma and de Klerk and shown in Figure 2.6. Its most important assumptions are (Gidley et al., 1989):

- i. Fracture height (h_f) is constant but the width (w_f) depends on the fracture half length (x_f).

- ii. The fracture has an elliptical cross-section in the horizontal plane and rectangular cross-section in the vertical plane.
- iii. The fluid pressure in the fracture is given by:

$$P(0,t) - P(x,t) = \frac{12}{h_f} \int_0^x \frac{dx}{w^3(x,t)} \quad (2.35)$$

with a boundary condition given as:

$$w(0,t) = \frac{2(1-\nu)x_f(P_f - \sigma_H)}{G} \quad (2.36)$$

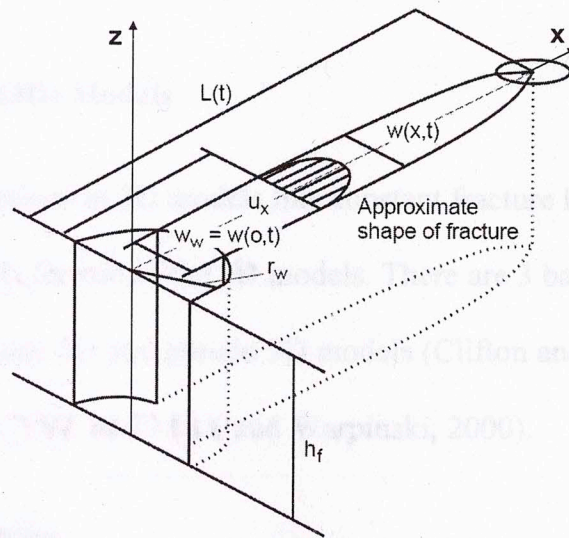


Figure 2.6: KGD model (Mack and Warpinski, 2000). $L(t)$ is the fracture half length, x_f

(c) Radial Model

This is also the penny-shaped model (see Figure 2.4) and refers to either vertical or horizontal circular fracture propagating radially outwards. Its main assumptions are:

- i. The radial distance from the center of the fracture is equal in all directions.
- ii. There is no boundary containment.
- iii. Pressure drop at the same distance in all direction is equal.

- iv. The fracture width decreases in all directions and has its maximum value at the wall of the borehole which is given by

$$w_{\max} = \frac{8(1-\nu^2)\Delta PR}{\pi E} \quad (2.37)$$

where ΔP is the differential pressure between the fracture fluid and the reservoir; R is the radius of the fracture; and E and ν are the formation's Young's modulus and Poisson's ratio, respectively.

2.3.2 Three-Dimensional (3D) Models

Some of the assumptions in 2D models like constant fracture height or radial fractures are eliminated with the use of the 3D models. There are 3 basic categories of the 3D models: general 3D, planar 3D and pseudo 3D models (Clifton and Abou-Sayed, 1979; Cleary, 1980; Baree, 1983; and Mack and Warpinski, 2000).

2.4 Rock Failure Mechanisms

Rocks deform and fail depending on loading conditions (Jaeger et al., 2007). In uniaxial compressive loading, rocks split irregularly along the stress axis in the absence of confining pressure. This failure plane tends to be inclined at an angle less than 45 degrees to the stress axis as confining pressure is applied. The failure plane is characterized by shear slippages and changes slightly under confined pressure where plastic deformation of rock grains are associated with a network of micro shear fractures. On the other hand, if the uniaxial loading is tensional, the rock mass appears to separate at a failure plane as extensional fractures. Brace (1964) described some rock failures

which appear to be comprised of both shear and extensional fractures as intrusive fractures.

Coulomb (1773) proposed a failure criterion which stated that rocks are likely to fail along a plane due to the action of shear stress on that plane according to equation (2.38)

$$|\tau| = S_o + \mu\sigma \quad (2.38)$$

where τ is the shear stress; S_o is the cohesion; μ is the coefficient of internal friction; and σ is the normal stress.

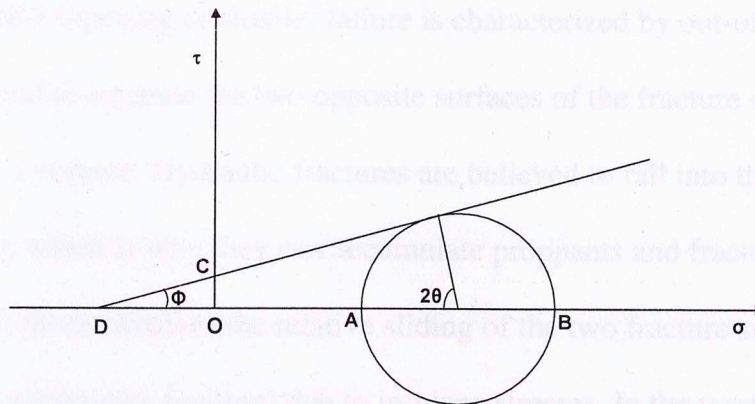


Figure 2.7: Mohr circle representation. OC is the cohesion, S_o ; OA is the least principal stress; OB is the maximum principal stress; and ϕ is the angle of internal friction.

Mohr (1900) introduced a replacement for equation (2.38) to account for the nonlinearity in the relationship between τ and σ . In other words, a curve is fitted to a series of Mohr circles in the (τ, σ) plane, giving the nonlinear relationship,

$$|\tau| = f(\sigma) \quad (2.39)$$

When rocks fail, the induced fractures tend to propagate in any of three modes – opening, sliding or tearing (Irwin, 1957) as shown in Figure 2.8.

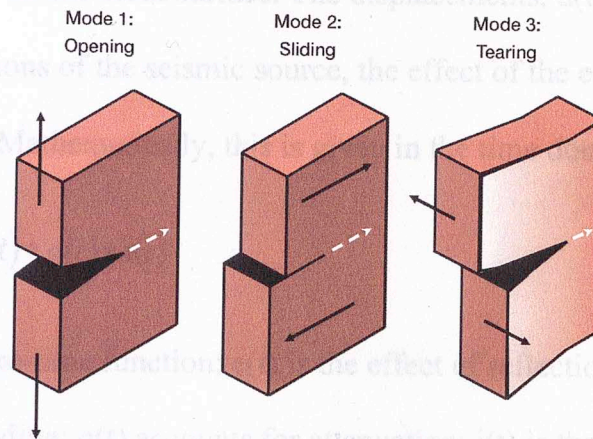


Figure 2.8: Opening, sliding and tearing modes of crack propagation (Martin and Valko, 2007). Solid arrow is the dislocation vector while the broken arrow is the crack propagation vector.

The mode 1 (opening or tensile) failure is characterized by out-of-plane extensive stresses which tend to separate the two opposite surfaces of the fracture symmetrically, thereby creating a volume. Hydraulic fractures are believed to fall into this category (Daneshy, 1974), which is why they can accumulate proppants and fracturing fluids. The sliding (or shear) mode involves the relative sliding of the two fracture surfaces on each other (similar to earthquake faulting) due to in-plane stresses. In the tearing (or mixed) mode, the fracture surfaces twist away from each other and occupy different planes. This can be observed as hackle marks in natural hydraulic fractures.

2.5 Basic Theory of Microseismicity in Rocks

A lot of what is known about microseismicity today stems from earthquake seismology. In earthquake studies, seismic waves are generated in the earth due to slips across fault planes. According to the elastic rebound theory proposed by Reid (1910), this slip results from the inability of rock particles on opposite sides of a fault to withstand

strain energy accumulated due to their relative movement on opposite sides of the fault plane. The seismic waves so generated travel through the earth and are detected by seismographs located on the earth surface. The displacements, $u(t)$, detected by the instruments are functions of the seismic source, the effect of the earth structure and the instrument response. Mathematically, this is given in the time domain as the convolution,

$$u(t) = x(t) * e(t) * q(t) * i(t) \quad (2.40)$$

where $x(t)$ is the source-time function; $e(t)$ is the effect of reflections, mode conversions and geometrical spreading; $q(t)$ accounts for attenuation; $i(t)$ is the instrument response; and $*$ is the convolution operator. In the frequency domain, equation (2.40) is given by its Fourier transform as

$$U(\omega) = X(\omega)E(\omega)Q(\omega)I(\omega) \quad (2.41)$$

where $X(\omega)$ is the source function; $E(\omega)$ is the effect of reflections, mode conversions and geometrical spreading; $Q(\omega)$ accounts for attenuation; and $I(\omega)$ is the instrument response.

2.5.1 Description of Microseismic Sources

The task in microseismic (or earthquake) studies is to relate the displacement detected at a location on a free surface to a fracture process within a medium. The point within a medium where the event originates is called the event hypocenter; the depth is called the focal depth; while the point on the earth surface directly above the event hypocenter is known as the epicenter. Usually, a displacement discontinuity, u across an internal surface, Σ , as shown in Figure 2.9, can be given as (Aki and Richards, 2002).

$$u_s(\vec{x}, t) = \int_{-\infty}^{\infty} dt \iint_{\Sigma} [d_i(\vec{\xi}, \tau)] c_{ijab} G_{sa,b}(\vec{x}, t; \vec{\xi}, \tau) n_j d\Sigma(\vec{\xi}) \quad (2.42)$$

Or

$$u_s(\vec{x}, t) = \int_{-\infty}^{\infty} dt \iint_{\Sigma} [d_i(\vec{\xi}, \tau)] c_{ijab} G_{sa,b}(\vec{x}, t - \tau; \vec{\xi}, 0) n_j d\Sigma(\vec{\xi}) \quad (2.43)$$

where \mathbf{n} is the normal to the surface of the discontinuity; \mathbf{d} is the slip vector; c_{ijab} is the fourth-order elastic constant tensor; ξ is the source point; τ is the corresponding time at the source point; \mathbf{x} is the receiver point; $G_{sa,b}$ is the spatial derivative of the elastodynamic Green's function, G_{sa} with respect to the ξ_b .

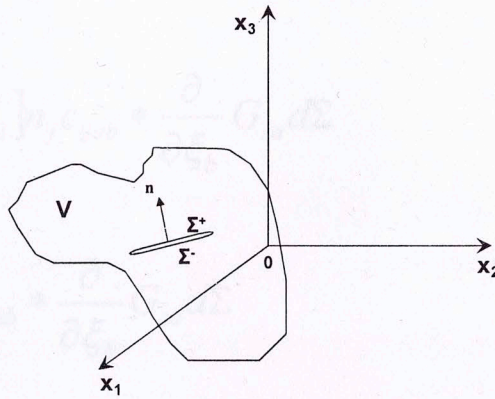


Figure 2.9: Internal discontinuity in a rock of volume, V bounded by a surface, Σ .

The Green's function is the displacement field that results from the application of a unidirectional unit impulse. In a homogeneous, isotropic, unbounded medium, it can be expressed as (Aki and Richards, 2002).

$$G_{sa}(\vec{x}, t; \vec{\xi}, \tau) = \frac{1}{4\pi\rho} \left\{ \begin{aligned} & \left[\frac{(3\gamma_s\gamma_a - \delta_{sa})}{r^3} \int_{r/V_p}^{r/V_s} t' \delta(t - \tau - t') dt' \right] \\ & + \left[\frac{\gamma_s\gamma_a}{rV_p^2} \delta\left(t - \tau - \frac{r}{V_p}\right) \right] \\ & + \left[\frac{(\gamma_s\gamma_a - \delta_{sa})}{rV_s^2} \delta\left(t - \tau - \frac{r}{V_s}\right) \right] \end{aligned} \right\} \quad (2.44)$$

Where V_p is the P-wave velocity; V_s is the S-wave velocity; ρ is the density of the medium; r and γ are the distance and unit vector from the source to the receiver, respectively.

Equation (2.43) can be expressed as a convolution by

$$u_s(\vec{x}, t) = \iint_{\Sigma} [d_i] n_j c_{ijab} * \frac{\partial}{\partial \xi_b} G_{sa} d\Sigma \quad (2.45)$$

$$u_s(\vec{x}, t) = \iint_{\Sigma} m_{ab} * \frac{\partial}{\partial \xi_b} G_{sa} d\Sigma \quad (2.46)$$

where m_{ab} are the elements of the moment density tensor which are given by

$$m_{ab} \equiv [d_i] n_j c_{ijab} \quad (2.47)$$

In a concise form, the integral of the moment density over the surface of the discontinuity gives the moment tensor, M . Thus, equation (2.46) becomes

$$u_s(\vec{x}, t) = M_{ab} * G_{sa,b} \quad (2.48)$$

where the moment tensor, M , is given by (Lay and Wallace, 1995)

$$M = \begin{bmatrix} M_{11} & M_{12} & M_{13} \\ M_{21} & M_{22} & M_{23} \\ M_{31} & M_{32} & M_{33} \end{bmatrix} \quad (2.49)$$

where each of the elements, M_{ab} , of equation (2.49) defines a force couple in the Cartesian coordinate system in which a pair of opposite forces separated by a finite distance in the 'b - direction' act in the 'a - direction' (see Figure 2.10).

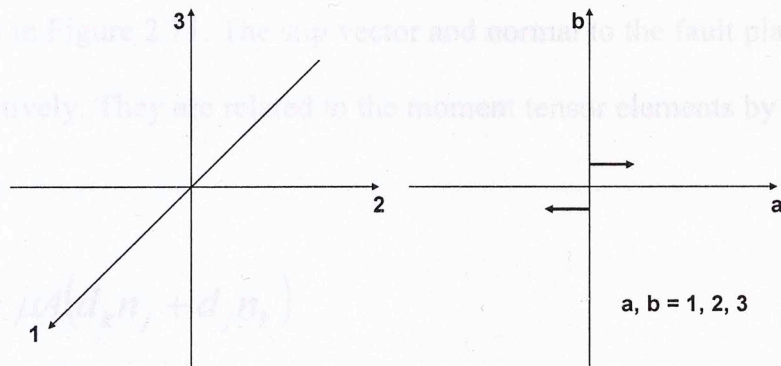


Figure 2.10: Couples on the Cartesian coordinate system constituting the seismic moment tensor.

The nine elements of the moment tensor reduce to six due to the conservation of angular momentum which also makes the tensor symmetric as expressed in equation (2.50). This is a good far-field approximation for representing body forces in an elastic medium (Shearer, 1999).

$$M = \begin{bmatrix} M_{11} & M_{12} & M_{13} \\ M_{12} & M_{22} & M_{23} \\ M_{13} & M_{23} & M_{33} \end{bmatrix} \quad (2.50)$$

The sense of slip and the orientation of the planar discontinuity on which the slip occurs constitute the focal mechanism of an earthquake. It has been used to study the kinematics of earthquakes based on the elastic rebound theory (Kayal, 2008). The geometry of the fault which causes the earthquake controls the earthquake radiation pattern.

Generally, the earthquake fault is assumed to be a plane on which one surface of the fault slides over the other in a particular direction. The side of the fault bearing the sliding surface is called the hanging wall block while the other is known as the foot wall block as shown in Figure 2.11. The slip vector and normal to the fault plane are given as \mathbf{d} and \mathbf{n} , respectively. They are related to the moment tensor elements by (Lay and Wallace, 1995)

$$M_{kj} = \mu A (d_k n_j + d_j n_k) \quad (2.51)$$

where μ is the shear modulus of the medium; A is the area of the fault; \mathbf{d} is the slip vector; \mathbf{n} is the normal vector; subscripts, k and j are equal to 1, 2, or 3.

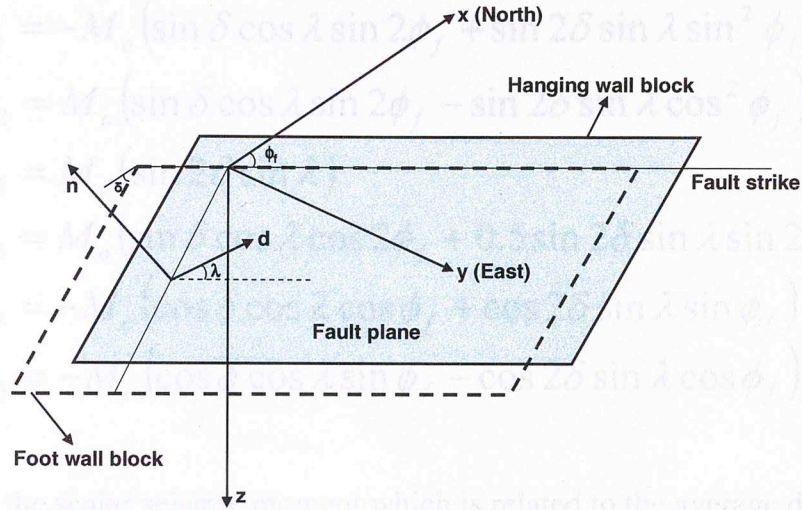


Figure 2.11: Fault geometry in a geographical coordinate system for earthquake studies. The hanging wall block (solid outline) is on top of the foot wall block (dash outline). The fault dip angle is given as δ , slip angle is λ and strike angle is ϕ_f .

The hanging wall block in Figure 2.11 (solid outline) moves along the slip vector, relative to the foot wall block (dash outline). The slip angle or rake, λ , ranges from 0 to 360°; dip angle, δ , varies from 0 to 90°; and strike angle, ϕ_f , varies from 0 to 360°.

In terms of the geographical coordinate system given in Figure 2.11, the slip vector and unit normal to the fault plane are given as

$$d = \begin{bmatrix} \cos \lambda \cos \phi_f + \sin \lambda \cos \delta \sin \phi_f \\ \cos \lambda \sin \phi_f - \cos \delta \sin \lambda \cos \phi_f \\ -\sin \delta \sin \lambda \end{bmatrix} \begin{bmatrix} x & y & z \end{bmatrix} \quad (2.52)$$

$$n = \begin{bmatrix} -\sin \delta \sin \phi_f \\ \sin \delta \cos \phi_f \\ -\cos \delta \end{bmatrix} \begin{bmatrix} x & y & z \end{bmatrix} \quad (2.53)$$

Substituting for \mathbf{d} and \mathbf{n} , we have

$$\begin{aligned}
M_{11} &= -M_o \left(\sin \delta \cos \lambda \sin 2\phi_f + \sin 2\delta \sin \lambda \sin^2 \phi_f \right) \\
M_{22} &= M_o \left(\sin \delta \cos \lambda \sin 2\phi_f - \sin 2\delta \sin \lambda \cos^2 \phi_f \right) \\
M_{33} &= M_o \left(\sin 2\delta \sin \lambda \right) \\
M_{12} &= M_o \left(\sin \delta \cos \lambda \cos 2\phi_f + 0.5 \sin 2\delta \sin \lambda \sin 2\phi_f \right) \\
M_{13} &= -M_o \left(\cos \delta \cos \lambda \cos \phi_f + \cos 2\delta \sin \lambda \sin \phi_f \right) \\
M_{23} &= -M_o \left(\cos \delta \cos \lambda \sin \phi_f - \cos 2\delta \sin \lambda \cos \phi_f \right)
\end{aligned} \tag{2.54}$$

where M_o is the scalar seismic moment which is related to the average displacement, D by (Kayal, 2008)

$$M_o = \mu AD \tag{2.55}$$

A null (\mathbf{B}) axis, orthogonal to both \mathbf{n} and \mathbf{d} can be derived from the cross product of \mathbf{n} and \mathbf{d} . Similarly, the pressure axis, \mathbf{p} (corresponding to the direction of maximum compressive stress) and tension axis, \mathbf{t} (corresponding to the direction of minimum compressive stress) can be obtained by a combination of \mathbf{n} and \mathbf{d} (Stein and Wysession, 2003)

$$\begin{aligned}
t &= n + d \\
p &= n - d
\end{aligned} \tag{2.56}$$

The magnitude of the seismic moment tensor components determine the type of fault causing an earthquake. They are used to graphically represent different fault types as shown in Figure 2.12 (Cronin, 2004). The strike-slip fault involves a horizontal relative movement of the two sides of the fault in which the hanging wall either moves to the right ($\lambda = 0^\circ$) yielding left-lateral strike-slip or moves to the left ($\lambda = 180^\circ$) yielding right-

lateral strike-slip. Normal faulting is caused by the downward sliding ($\lambda = 270^\circ$) of the hanging wall while reverse faulting is a result of the upward movement ($\lambda = 90^\circ$) of the hanging wall.

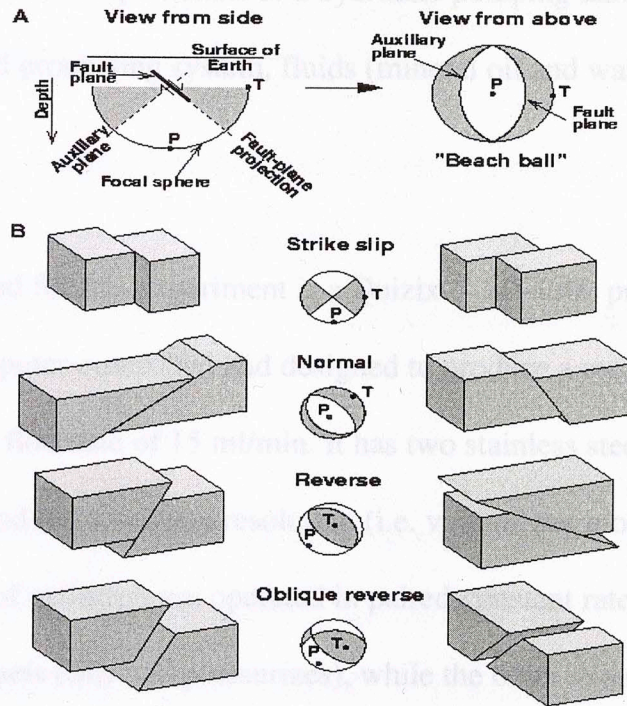


Figure 2.12: Basic fault geometry and beach ball representations (source: <http://geology.about.com/library/bl/blbeachball.htm>).

The procedure for the construction of lower hemisphere focal plots (beach balls) is outlined in Appendix A.

3 EXPERIMENTAL METHODOLOGY

3.1 Equipment and Materials

The experimental setup consists of a hydraulic pumping unit, acoustic emission signal acquisition and processing system, fluids (mineral oil and water) and rock samples.

3.1.1 Pumping Unit

The pump used for this experiment is a Quizix™ SP-5200 pumping unit (see Figure 3.1). It is computer-controlled and designed to produce a maximum pressure of 10 kpsi and a maximum flow rate of 15 ml/min. It has two stainless steel cylinders of 9.3- ml barrel volume each and has a volume resolution (i.e. volume per motor step) of 0.318 nanoliters. The pair of cylinders are operated in paired-constant rate delivery mode so that one cylinder retracts (fills and pressurizes), while the other extends to delivers fluid to the outlet. After a stroke, the two cylinders switch functions and continue to work alternately until pumping is terminated.

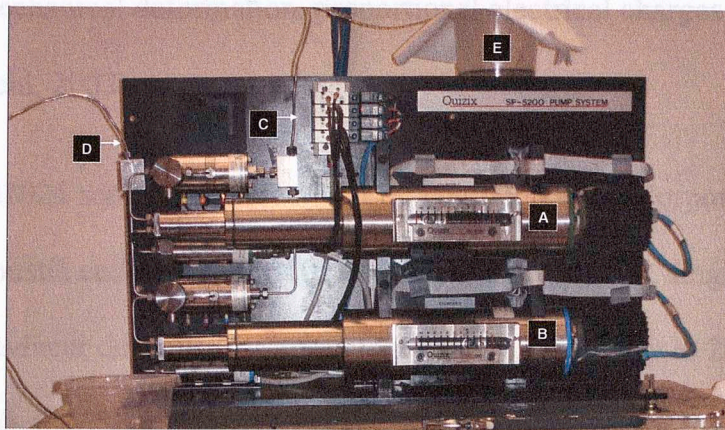


Figure 3.1: Quizix™ SP-5200 pumping unit used for hydraulic fracturing experiments. It has a maximum pumping rate rate of 15 cc/minute and maximum pressure of 10,000 psi. A and B are cylinders 1 and 2, respectively; C and D are the fluid inlet and outlet lines, respectively; and E is the fracturing fluid reservoir. Each cylinder has a piston stroke volume of 9.3 ml and a volume resolution of 0.318 nanoliters.

3.1.2 Fluid System

The fracturing fluids used for our experiments are water and mineral oil with viscosities at ambient conditions of 1cp and 37 cp, respectively.

3.1.3 Acoustic Emission (AE) Monitoring System

The acoustic emission (AE) monitoring system utilized in the experiments consists of piezoelectric sensors (16), broadband pre-amplifiers (16), a 16-channel signal conditioning unit and a data acquisition module attached to a personal computer (PC).

(a) Sensor

Acoustic emissions (AE) are generally detected using piezoelectric transducers (PZT 5A) which act as both sensing and transduction elements. Usually, the sensing element responds directly to a measured quantity (displacement, velocity, or acceleration) while the transduction element is the electrical portion of the sensor that provides the output voltage. The AE sensors work on the principle that when a piezoelectric material is subjected to mechanical deformation, proportional electrical charges are induced at terminals (Gautschi, 2002).

Sixteen B1025 sensors manufactured by Digital Wave® Corporations were used to capture the acoustic emissions. A B1025 sensor is a broadband, single-component piezoelectric transducer designed for a frequency range of 50 KHz to 2MHz. Its small size (1-inch length, 0.365-inch diameter and 0.25-inch diameter for the piezoelectric material), high fidelity and low attenuation make it ideal for this application. They are

calibrated by the manufacturer using an absolute surface wave calibration technique to yield a displacement sensitivity of 40 dB (ref. 1 V/ μm) as shown in Figure 3.3.

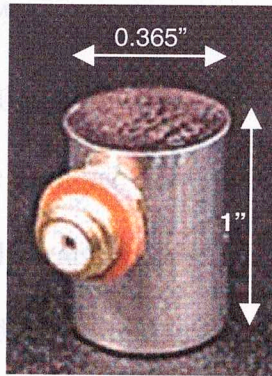


Figure 3.2: Broadband acoustic emission transducer (B1025)

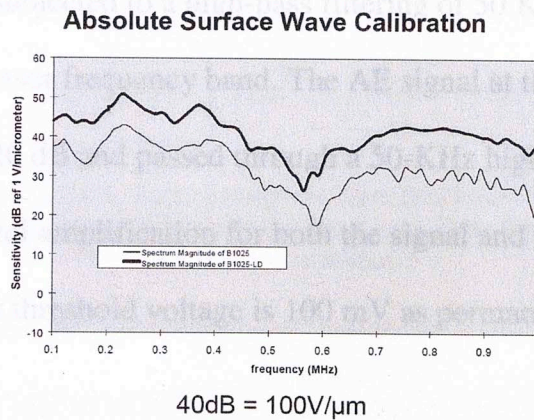


Figure 3.3: Calibration of AE transducer (B1025)
(source:http://www.digitalwavecorp.com/mae_sensors.html)

(b) Preamplifier

Each sensor is connected to a model 5660B Panametrics-NDTTM wide band preamplifier via a BNC-to-Microdot coaxial cable. The preamplifiers have a frequency band between 500 Hz and 40 MHz and two gain settings – 40 and 60 dB. Their specifications are provided in Appendix A. Each preamplifier output is connected to a signal card in the signal conditioning unit via a BNC-to-BNC coaxial cable.

(c) Signal Conditioning Unit

Signals from the pre-amplifiers are transmitted to the signal conditioning unit – 16-channel Field Module (FM-1TM) unit which is shown in Figure 3.4, where further amplification and filtering of AE signals are provided. The FM-1TM is installed with 2 controller cards, each having three sections – internal preamplifier, signal and trigger conditioning sections. The internal preamplifier stage increases the AE signal input from the sensors by a gain of 6 dB and feeds it, in parallel, to the signal and trigger conditioning sections. At the signal conditioning section the AE signal is further amplified by a gain of 24 dB and subjected to a high-pass filtering of 50 KHz – corresponding to the lower limit of the sensor frequency band. The AE signal at the trigger conditioning section is amplified by 20 dB and passed through a 50-KHz high-pass and 1.5-MHz low-pass filters. Thus, the total amplification for both the signal and trigger are 70 and 66 dB, respectively. The trigger threshold voltage is 100 mV as permanently set by the manufacturer.

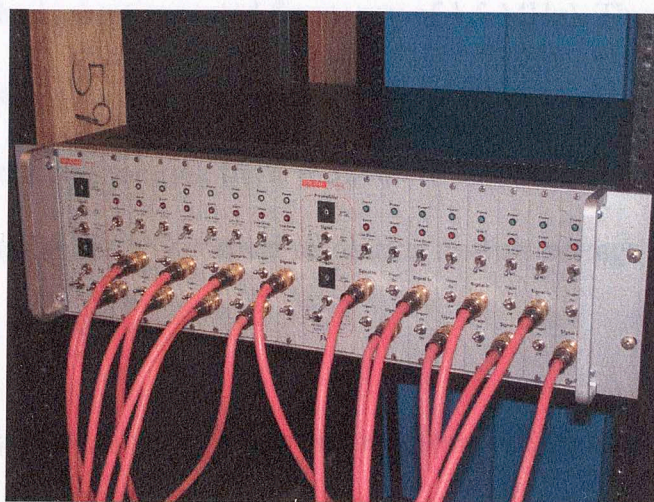


Figure 3.4: Field Module (FM-1TM) unit manufactured by Digital Wave®, Inc. It accommodates 16 channels as shown by the cable connections from a stack of 16 external preamplifiers. It also consists of an internal preamplifier stage (gain = 6dB); trigger stage (gain = 20 dB, LP filtering = 50 KHz and HP filtering = 1.5 MHz); and signal stage (gain = 24 dB and HP filtering = 50 KHz).

(d) Data Acquisition Module

The data acquisition module is the ICS-645 PCI Bus analog input board. A block diagram is shown in Figure 3.5. It has 32 channels and receives signal and trigger inputs from the FM-1TM unit.

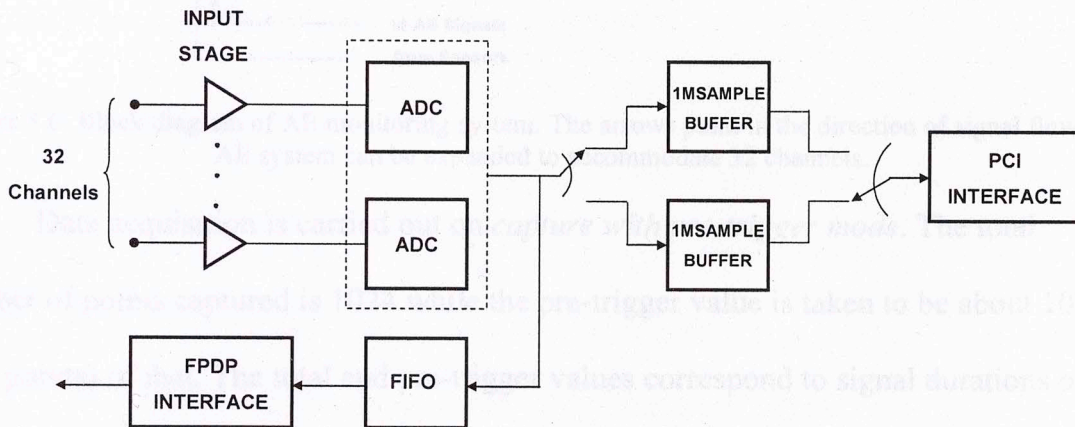


Figure 3.5: ICS-645 Simplified block diagram (modified from DaqScribe Technology, Inc., 2003). FIFO stands for First-In-First-Out memory. FPDP stands for Front Panel Data Port interface. For our purpose 16 channels were utilized.

The ICS-645 board incorporates 16-bit resolution ADC's (AD9260) and has a maximum sampling rate (f_s) of 20 MHz. We set the sampling rate to be 5MHz (i.e. greater than twice the highest expected frequency of 1.5 MHz). Thus, giving an oversampling ratio of 4 (i.e. $20 \div 5$). The full scale input is ± 1.03 volts which is digitized to yield quantization levels ranging from -32484 to $+32483$ (DaqScribe Technology, Inc., 2003). This implies that the vertical resolution (lowest voltage recorded) of the data acquisition board is $30 \mu\text{V}$.

A schematic diagram of the entire process, from AE signal detection to data storage on a PC is shown in Figure 3.6.

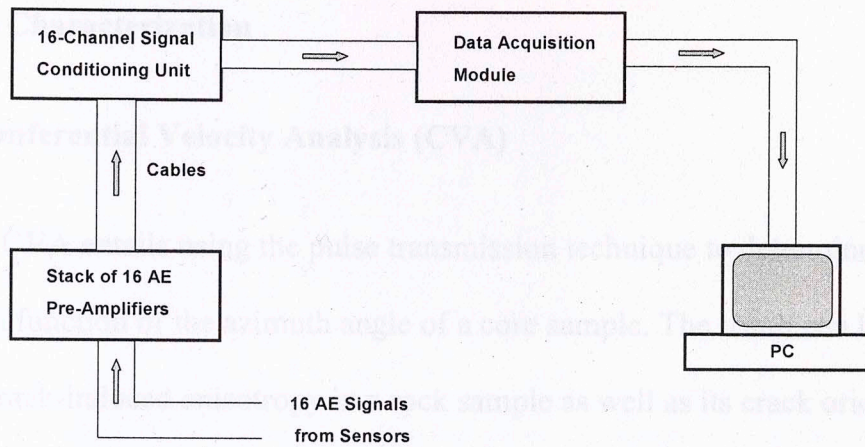


Figure 3.6: Block diagram of AE monitoring system. The arrows point in the direction of signal flow. The AE system can be expanded to accommodate 32 channels.

Data acquisition is carried out on *capture with pre-trigger mode*. The total number of points captured is 1024 while the pre-trigger value is taken to be about 10% (102 points) of that. The total and pre-trigger values correspond to signal durations of 20.4 μs and 204.8 μs , respectively for a sampling rate of 5 MHz. The upper and lower values of P-wave velocity in our experimental samples (which are approximately 101.6 mm in diameter and 75 mm in length) are 4 and 6 mm/ μs - corresponding to a maximum travel time (maximum distance /velocity) of 31.57 μs and 21.05 μs , respectively. The pre-trigger points are chosen based on the frequency range of the AE signal expected: a frequency range of 50 kHz and 1.5 MHz corresponds to signal periods of 20 μs and 0.67 μs , respectively. From several trial experiments, the signal trigger gains are set so that the early arriving portion of the AE signal waveform is of sufficient amplitude to constitute a valid trigger of ± 100 mV. This ensures that sufficient pre-trigger data is stored.

3.2 Sample Characterization

3.2.1 Circumferential Velocity Analysis (CVA)

The CVA entails using the pulse transmission technique to determine seismic velocity as a function of the azimuth angle of a core sample. The result can be used to determine crack-induced anisotropy in a rock sample as well as its crack orientations. In an isotropic sample, the P- and S-waves will be constant regardless of sample azimuth. Usually, this is not the case; rocks contain aligned cracks and minerals. The velocities along a preferred crack orientation will be highest while those normal to it will be lowest. Thus, we can infer crack and in-situ stress directions from CVA. Stress-relief cracks tend to be aligned perpendicular to the direction of the maximum stress in the region where they occur.

In the CVA technique, the sample is mounted firmly on a rotatable base with a calibrated azimuth from 0° to 360° . A starting point is defined on the outer circumference of the sample, i.e. zero degrees azimuth. Two spring-loaded P-wave transducers (transmitting and receiving piezoelectric transducers) are mounted diametrically across the sample in the zero degree azimuth direction as shown in Figure 3.7.

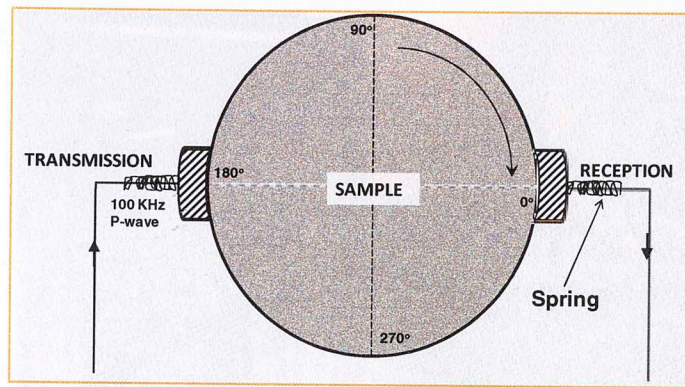


Figure 3.7: Schematic of circumferential velocity analysis (CVA) in plan view showing the P-wave piezoelectric transducers (hatched portions) located diametrically across a sample. The sample is rotated clockwise through 10° increments and P-wave velocity measurements are made.

A 100 KHz gated sinusoidal signal from a pulse generator is sent through the sample and received on the opposite side of the sample. Each received signal is amplified by a 60-dB ultrasonic preamplifier as seen in Figure 3.8 (item C). Fifty received signals are stacked in order to filter out noise. The stacked trace is amplified, displayed on a digital oscilloscope and stored in a computer. The CVA base is rotated 10 degrees and the same procedure is repeated until 36 traces have been acquired. Specially-designed software is used to display the 36 traces and interactively pick the travel times. Dividing the diameter of the sample by these travel times less the transducer delay time gives the compressional wave velocities (V_p) through the sample as a function of its azimuth.

The shear wave velocities are measured in a similar way except that shear wave transducers are attached to the top and bottom of each sample so that one trace of shear wave is acquired. The shear wave velocity (V_s) is then calculated by the dividing the sample length by the travel time less the transducer delay time.

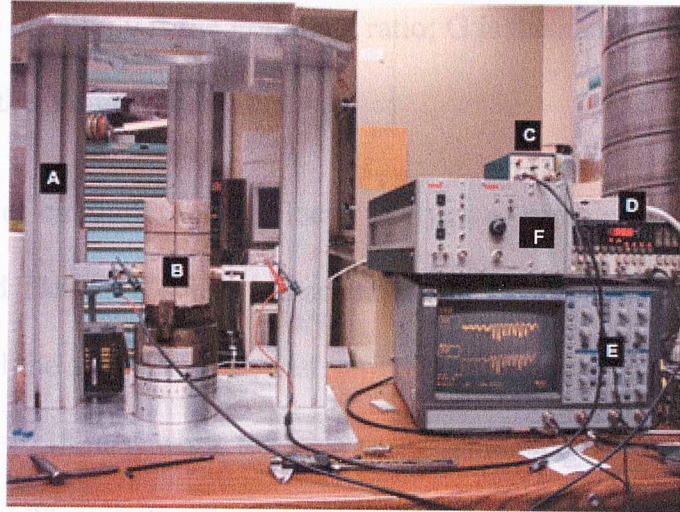


Figure 3.8: Apparatus for circumferential velocity analysis (CVA). A is the support frame; B is the sample mounted on a rotatable base; C is an active pulse amplifier (40/60 db); D is a pulse generator; and E is a digital oscilloscope with waveform averaging capabilities; and F is a high voltage amplifier.

The dynamic elastic properties are computed with equations (3.1) through (3.4) and using values of P-wave velocity, S-wave velocities and bulk densities. P-wave velocities we used are those that give the least absolute location error for pencil lead breaks during Hsu-Nielsen AE calibration (Zeng, 2002).

$$\nu = \frac{0.5 \left(\frac{V_p}{V_s} \right)^2 - 1}{\left(\frac{V_p}{V_s} \right)^2 - 1} \quad (3.1)$$

$$G = \rho V_s^2 \quad (3.2)$$

$$K = \rho \left(V_p^2 - \frac{4}{3} V_s^2 \right) \quad (3.3)$$

$$E = 2G(1 + \nu) \quad (3.4)$$

where ρ is the bulk density; ν is the Poisson's ratio; G is the shear modulus; K is the bulk modulus; and E is the Young's modulus.

The results of circumferential velocity analysis of samples E1 – E8 are presented in Figures (3.9) and Table 3.1. There is a considerable variation of P-wave velocity with azimuth angle in all the samples. The most variation is observed in sample E5 (V_p standard deviation = 238 m/s) while the least variation is recorded in sample E1 (V_p standard deviation = 23 m/s). Correlations of V_p with azimuth angle are presented in section 4.2.3.

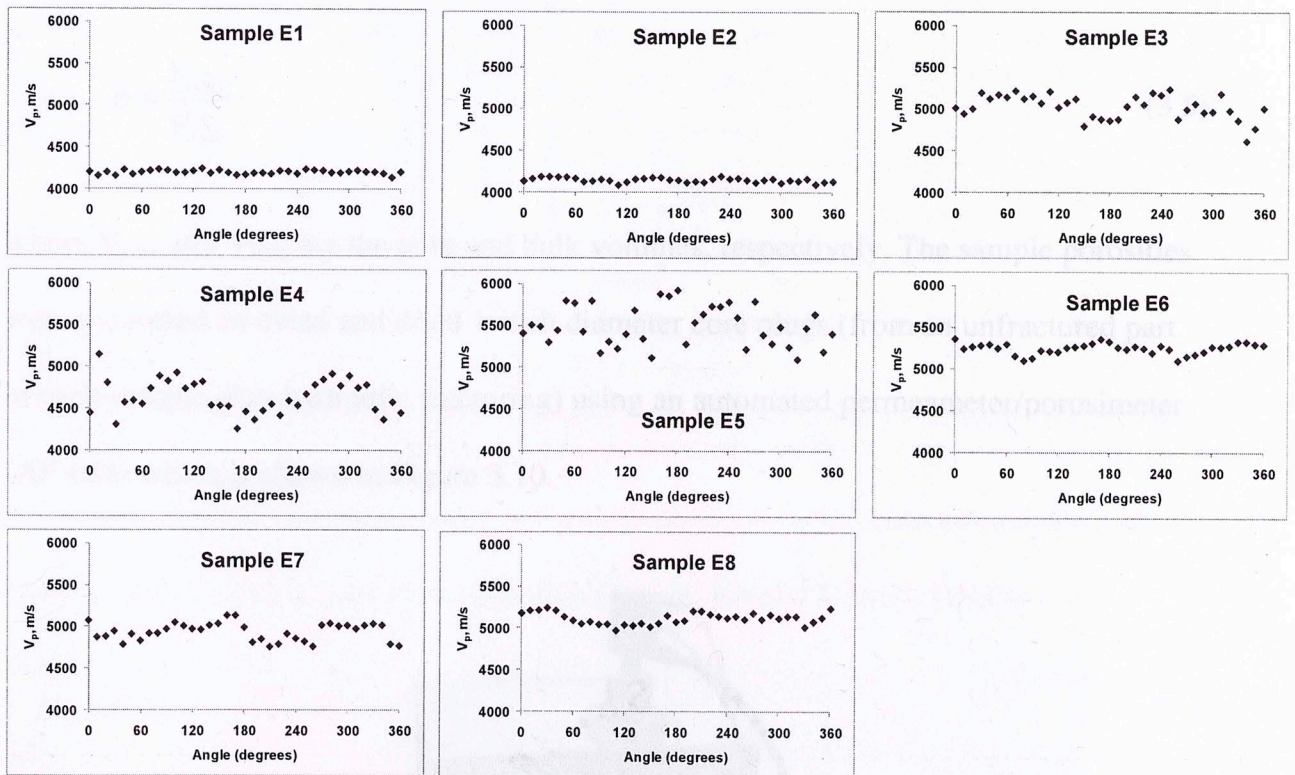


Figure 3.9: CVA results of sample E1 – E8. They are plots of P-wave velocity (V_p) as a function of azimuth angle.

Table 3.1: Results of circumferential velocity analysis (CVA) of sample E1 – E8

Sample ID	Compressional Wave Velocity, m/s			
	Minimum	Maximum	Average	Std. Dev.
E1	4137	4239	4197	23
E2	4084	4192	4147	26
E3	4608	5238	5024	147
E4	4252	5141	4635	203
E5	5094	5920	5492	238
E6	5099	5357	5247	64
E7	4762	5135	4937	106
E8	4964	5235	5112	69

3.2.2 Porosity Measurement

The porosity (ϕ) of a rock sample is ratio of its pore to bulk volume expressed as a fraction or percentage (Cone and Kersey, 1992):

$$\phi = \frac{V_{pore}}{V_{bulk}} \quad (3.5)$$

where V_{pore} and V_{bulk} are the pore and bulk volumes, respectively. The sample porosities were measured on clean and dried 1-inch diameter core plugs (from an unfractured part of each sample after hydraulic fracturing) using an automated permeameter/porosimeter (AP-608) which is shown in Figure 3.10.



Figure 3.10: Automatic Klinkenberg permeameter/porosimeter (AP-608) for measuring sample porosity and permeability as a function of confining pressure up to 10, 000 psi.

3.2.3 The AP-608 measures sample porosity using the Boyle's Law method. The flat end faces of the sample are polished to +/- 0.005 – inch accuracy. The samples are cleaned using a mixture of 20% methanol and 80% toluene in a Soxhlet extractor. Each of the samples is dried in an oven for 8 hours and inserted inside the core holder of the AP-608 and confining pressures ranging from 500 to 2000 psi is applied to an impermeable sleeve to seal it. Helium gas from a reference cell of known pressure, P_1 , is injected into the sample until it is judged to be fully saturated (see Figure 3.11)

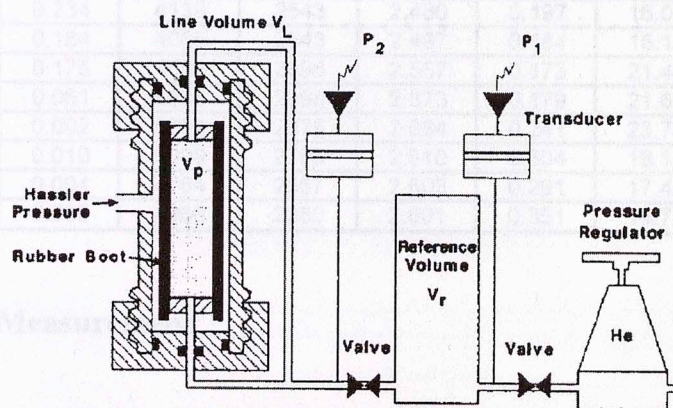


Figure 3.11: Boyle's law method of porosity determination. Rock sample is placed inside the rubber boot and pressurized (Cone and Kersey, 1992).

The pore volume of the rock sample is then calculated to be the volume of helium gas injected into it. This is done using equation (3.6) (Cone and Kersey, 1992).

$$P_1 V_r = P_2 (V_r + V_L + V_{pore}) \quad (3.6)$$

where V_r is the reference volume; V_L is the total volume of connecting lines; and V_{pore} is sample pore volume. Equation (3.5) is then invoked to compute sample porosity.

3.2.3 Permeability measurement

In addition to measuring porosity, the AP-608 uses a pulse decay technique to measure permeabilities of core samples (Coretest Systems, 2002). The procedure is described by Jones (1971). Klinkenberg permeability values are reported along with other petrophysical and elastic properties in Table 3.2.

Table 3.2: Petrophysical and elastic properties of sample E1 – E8. Φ and k are reported at 800-psi confining pressure.

Sample ID	ϕ , %	k, md	V_p , m/s	V_s , m/s	ρ , g/cc	ν	G, Gpa	K, Gpa	E, Gpa
E1	7.10	0.234	4139	2543	2.480	0.197	16.03	21.10	38.39
E2	7.10	0.184	4085	2543	2.497	0.184	16.14	20.14	38.23
E3	5.77	0.175	4609	2898	2.557	0.173	21.47	25.69	50.38
E4	3.59	0.061	4635	2898	2.573	0.179	21.61	26.46	50.96
E5	2.90	0.002	5094	2975	2.684	0.241	23.75	37.97	58.97
E6	3.21	0.010	5099	2708	2.610	0.304	19.14	42.34	49.90
E7	2.42	0.004	4764	2587	2.603	0.291	17.42	35.84	44.98
E8	2.43	0.006	4966	2380	2.601	0.351	14.73	44.50	39.81

3.2.4 Mineralogy Measurement

Rocks are composed of mineral grains, cementing materials, pore fluids, and voids. These components determine the elastic and poroelastic properties of petroleum reservoirs. The Fourier Transform Infrared (FTIR) Spectroscopy can be used in determining the mineral composition of rocks by comparing them to a library of known mineral spectra (Sondergeld and Rai, 1993). These minerals have covalent bonds which are known to vibrate and absorb infrared light at certain wavelengths. The Thermo Nicolet Avatar 370 FTIR shown in Figure 3.12 is used to measure the mineral compositions. Quantitative analysis software estimates the weight percent of 16 minerals – Quartz, Calcite, Dolomite, Illite, Smectite, Kaolinite, Chlorite, Pyrite, Orthoclase, Oligoclase, Mixed Clay, Albite, Anhydrite, Siderite, Apatite and Aragonite. The theory

and measurement procedures are explained by Ballard (2007). The mineral compositions (in weight percentage) for the eight samples used for our hydraulic fracturing experiments are shown in Table 3.3.

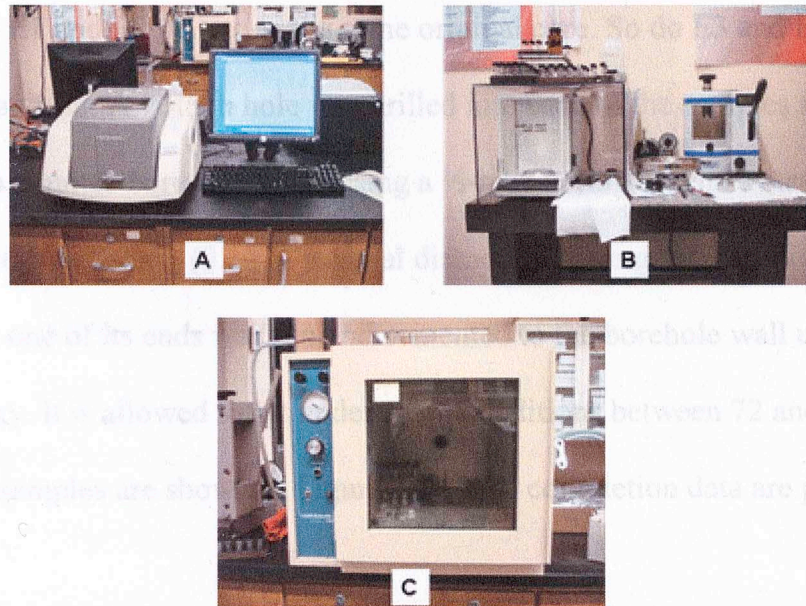


Figure 3.12: Apparatus for the measuring mineral composition. A is the Thermo Nicolet Avatar 370 FTIR equipment; B contains weighing balance on the left and a pellet press on the right; and C is the oven used in drying powdered samples.

Table 3.3: FTIR mineralogical compositions of samples E1 to E8 in weight percentages

Rock Minerals	Sample ID							
	E1	E2	E3	E4	E5	E6	E7	E8
Quartz	0	0	2	0	0	0	0	0
Calcite	48	62	50	64	32	65	69	77
Dolomite	31	24	29	13	61	23	10	10
Illite	0	0	1	0	0	1	2	0
Smectite	1	0	2	2	0	0	1	0
Kaolinite	0	0	0	0	0	0	0	0
Chlorite	2	3	5	5	2	4	3	4
Pyrite	6	6	5	6	0	1	6	3
Orthoclase	0	0	0	0	0	0	0	0
Oglioclase	0	0	0	0	0	0	0	0
Mixed Clay	4	1	1	2	0	0	0	0
Albite	0	0	0	0	3	3	1	3
Anhydrite	2	0	1	1	0	0	2	1
Siderite	0	0	0	0	0	0	0	0
Apatite	1	1	0	1	0	1	1	1
Aragonite	5	4	4	6	1	2	5	3

3.3 Experimental Procedure

Eight cylindrical core samples obtained from splitting four 6-inch-length core samples are carefully polished so that they are right circular. The samples are labeled E1 to E8. Sample E1 and E2 belong to the same original core. So do E3 and E4, E5 and E6 as well as E7 and E8. A ¼-inch hole was drilled into each of the samples from one of the flat ends and a counter-bore was made using a ½-inch coring bit and a steel mini-casing/high pressure tubing (0.12” - internal diameter), having two perforations at 180° phase close to one of its ends was run and cemented to the borehole wall using Conley Weld™ epoxy. It is allowed to set under room conditions between 72 and 120 hours. The prepared samples are shown in Figure 3.13. The completion data are presented in Table 3.4.

Table 3.4: Completion data for hydraulically fractured samples

	Sample ID							
	E1	E2	E3	E4	E5	E6	E7	E8
Length, mm	70	76	76	73	73	75	73	75
Diameter, mm	101.6	101.6	101.6	101.6	101.6	101.6	101.6	101.6
Borehole depth, mm	37.0	31.5	33.3	33.5	40.0	40.0	39.0	39.5
Counter-bore depth, mm	12.5	14.5	12.5	14.0	10.0	11.0	10.0	12.0
Bonding depth, mm	27.5	22.5	24.0	24.0	29.5	29.0	29.5	30.0
Perforation depth, mm	33.5	28.5	30.0	30.0	35.5	35.0	35.5	36.0

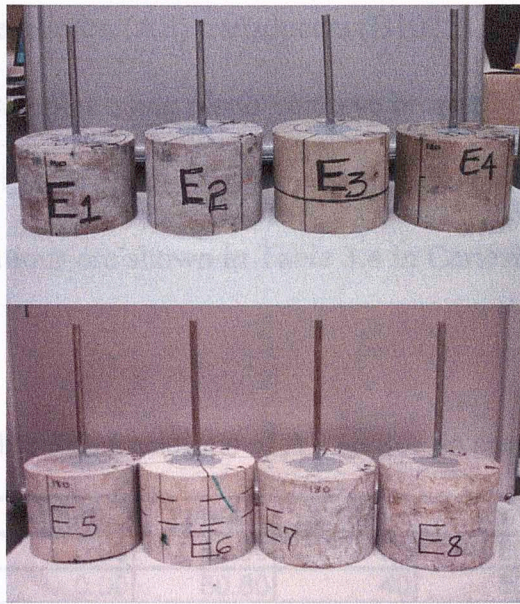


Figure 3.13: Samples under preparation before hydraulic fracturing.

A Cartesian coordinate (x, y, z) system is defined on each cylindrical sample such that its top flat surface bears the x - y plane with the origin at the center. The z -axis starts from the origin and increases downwards to the flat bottom surface (see Figure 3.14).

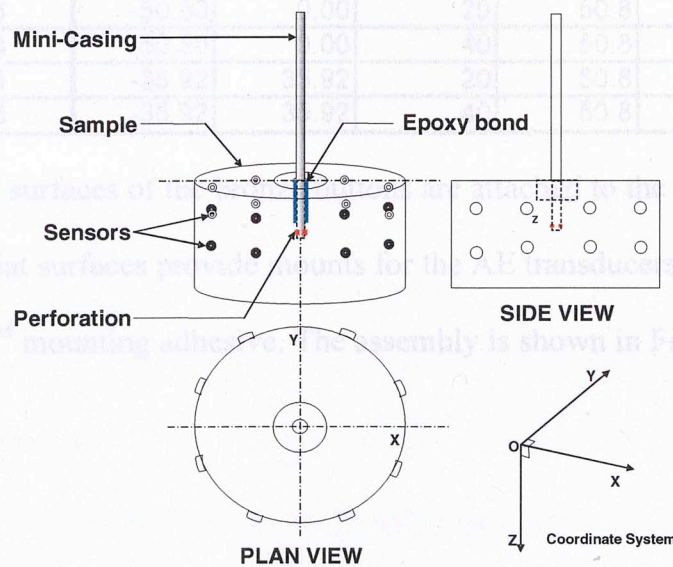


Figure 3.14: 3-D plan and side views of a 4-in diameter sample completed with 0.12 in ID mini-casing. 16 broadband acoustic emission (AE) transducers are shown in small circles. Red squares indicate perforation points while the blue portion symbolizes Conley Weld™ epoxy which acts to confine fracturing fluids to the annulus around the perforations.

Sixteen acoustic emission (AE) transducers (B1025) are attached to the curved surface of each of the 8 samples using plano-concave bronze buttons. The sensors are mounted on the samples in two circular arrays covering the expected hydraulic fracture location. The sensor locations are shown in Table 3.4 in Cartesian and cylindrical coordinate systems.

Table 3.5: Locations of AE sensor on samples

Sensor ID	x, mm	y, mm	z, mm	r, mm	ϕ , degrees
1	0.00	50.80	20	50.8	0
2	0.00	50.80	40	50.8	0
3	35.92	35.92	20	50.8	45
4	35.92	35.92	40	50.8	45
5	50.80	0.00	20	50.8	90
6	50.80	0.00	40	50.8	90
7	35.92	-35.92	20	50.8	135
8	35.92	-35.92	40	50.8	135
9	0.00	-50.80	20	50.8	180
10	0.00	-50.80	40	50.8	180
11	-35.92	-35.92	20	50.8	225
12	-35.92	-35.92	40	50.8	225
13	-50.80	0.00	20	50.8	270
14	-50.80	0.00	40	50.8	270
15	-35.92	35.92	20	50.8	315
16	-35.92	35.92	40	50.8	315

The curved surfaces of the bronze buttons are attached to the curved surface of the sample while the flat surfaces provide mounts for the AE transducers (B1025). We used Crystalbond 555TM mounting adhesive. The assembly is shown in Figure 3.15.

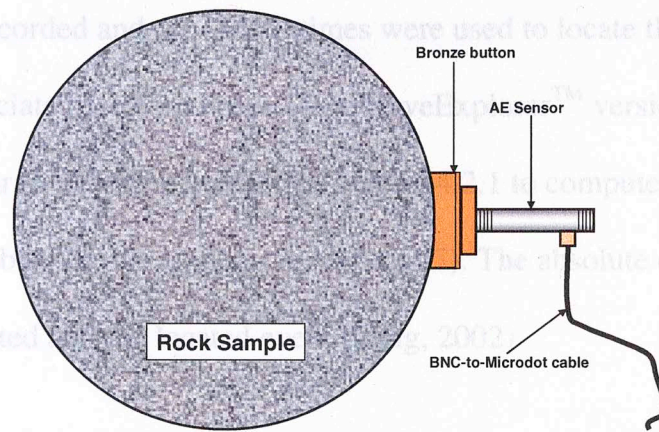


Figure 3.15: Plan view of the interconnections between rock sample, bronze button and AE transducer. The curved end of the bronze button has a dimension of 17.50 mm in diameter and 3.25 mm in thickness. Its flat end is 14.44 mm in diameter and 2.50 mm thick. Only one channel is shown.

On the AE software (WaveExplorer™ version 7.1) interface, the number of channels (16), sampling rate (5 MHz), number of sampling points (1024), and pre-trigger points (102) are specified. Thus, the storage memory allocated to one AE event is 32 KB [i.e. 16 bits (ADC resolution) * 16 channels * 1024 (sampling points) / 8 (bits/byte)]. The other information input to the software are the location of the 16 B1025 sensors, velocity model, type of material or sample, and elastic properties of the sample. P-wave velocities are computed and used for AE event locations.

AE system is calibrated using the Hsu-Nielsen source (Zeng, 2002). As shown in Figure 3.16, when a 0.5 mm or 0.3 mm brittle lead pencil is broken on a surface connected with a suitable apparatus, artificial acoustic emission (AE) events are generated which are similar to step function unloading sources. The purpose of this exercise is to verify that the AE sensors are properly attached to the specimen as well as check the accuracy of source location program. Prior to each experiment, the lead breaks were carried out in eight different locations on the $z = 0$ plane. The locations of the pencil breaks are shown in Table 3.5 in both the Cartesian and cylindrical coordinates. The AE

waveforms were recorded and the arrival times were used to locate the events and calculate their associated location errors. The WaveExplorer™ version 7.1 software uses an algorithm similar to the one presented in section 4.2.1 to compute the event locations. We computed the absolute errors using equation (3.7). The absolute error is the distance between the simulated and the located event (Zeng, 2002).

$$Error_{Abs.} = \sqrt{(x_s - x_l)^2 + (y_s - y_l)^2 + (z_s - z_l)^2} \quad (3.7)$$

where subscripts, s and l, indicate simulated (known) and located events.

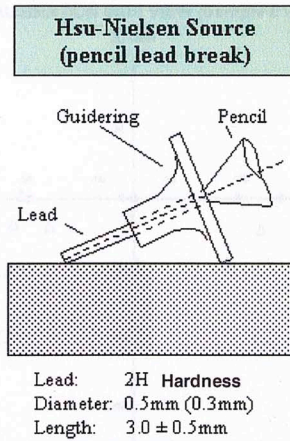


Figure 3.16: Hsu-Nielsen source for the testing and calibration of acoustic emission systems (source: <http://www.ndt.net/ndtaz/ndtaz.php>)

Table 3.5: Locations of pencil lead breaks for AE system calibration in Cartesian and cylindrical coordinates.

Event No	x, mm	y, mm	z, mm	r, mm	φ, degrees
1	0.00	40.80	0	40.8	0
2	28.85	28.85	0	40.8	45
3	40.80	0.00	0	40.8	90
4	28.85	-28.85	0	40.8	135
5	0.00	-40.80	0	40.8	180
6	-28.85	-28.85	0	40.8	225
7	-40.80	0.00	0	40.8	270
8	-28.85	28.85	0	40.8	315

The results are presented in Figures 3.17 to 3.24.

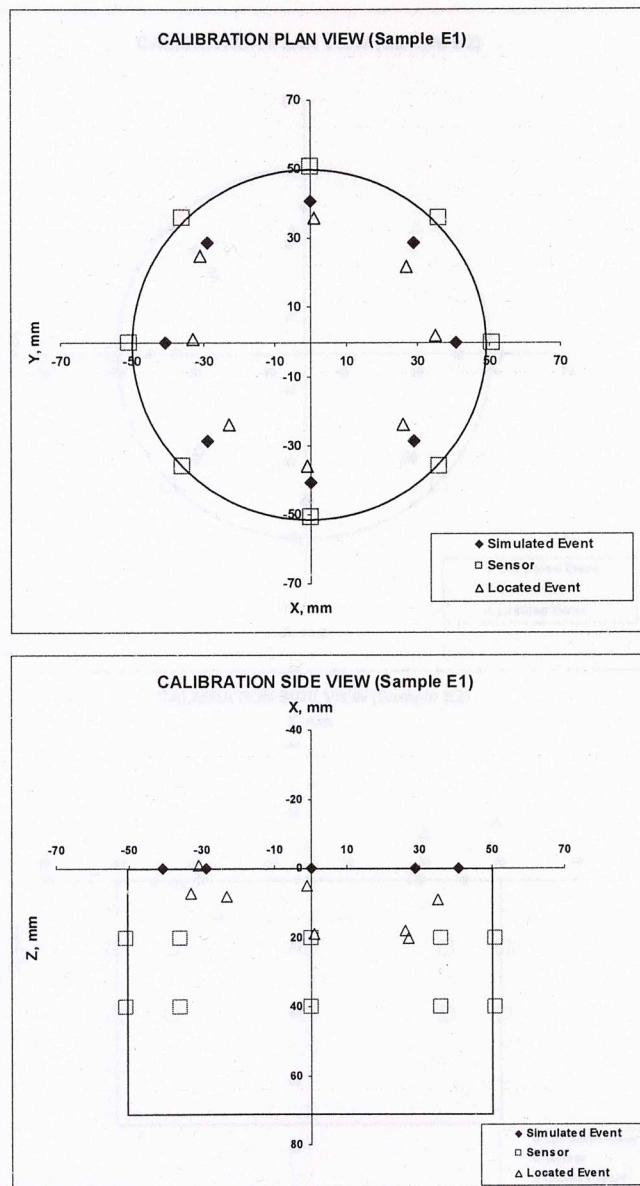


Figure 3.17: 3D location of acoustic emission (AE) associated with pencil lead breaks on sample E1. The 'simulated events' are the lead breaks while the 'Located Events' are results generated by the source location program. The absolute errors range between 4.52 and 21.22 mm and have an average value of 12.96 mm for a constant velocity model of 4139 m/s.

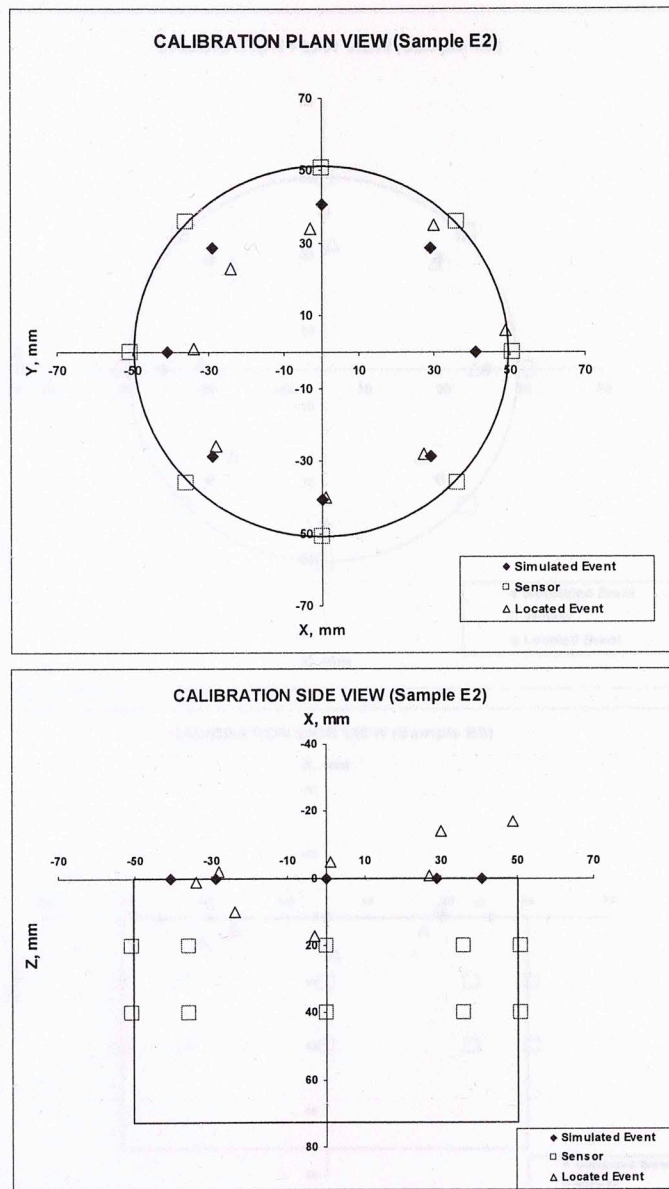


Figure 3.18: 3D location of acoustic emission (AE) associated with pencil lead breaks on sample E2. The 'simulated events' are the lead breaks while the 'Located Events' are results generated by the source location program. The absolute errors range between 2.27 and 19.80 mm and have an average value of 10.53 mm for a constant velocity model of 4085 m/s.

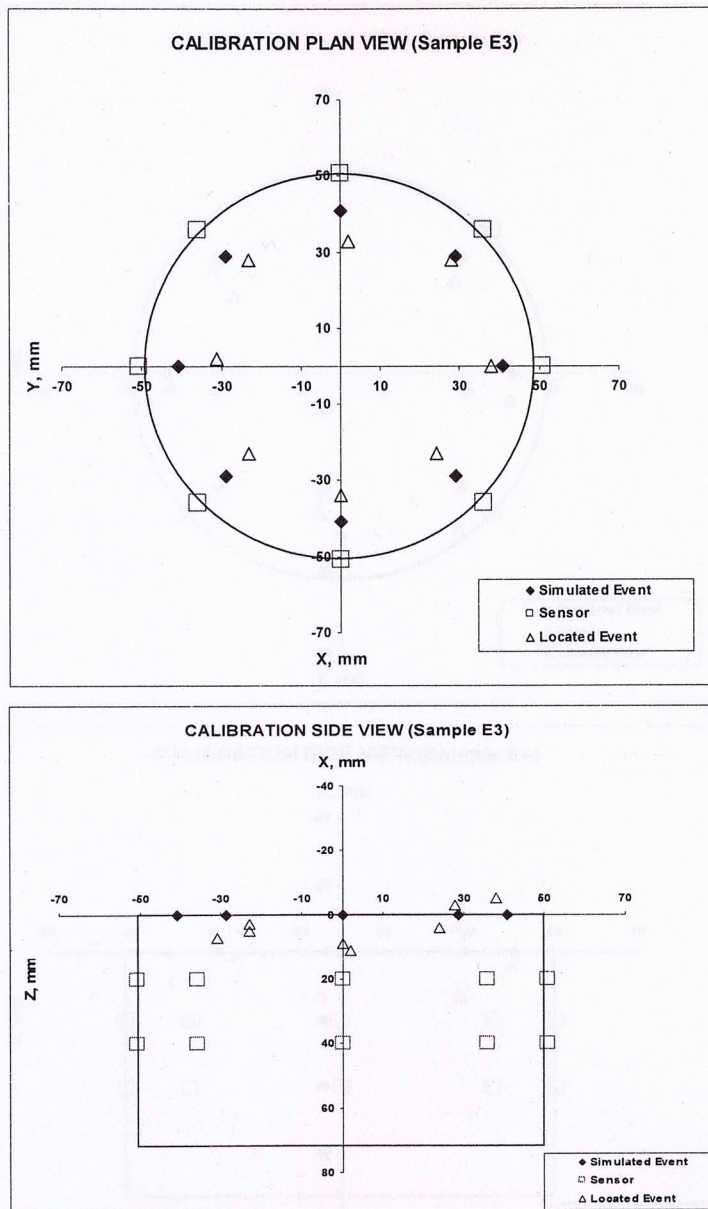


Figure 3.19: 3D location of acoustic emission (AE) associated with pencil lead breaks on sample E3. The 'simulated events' are the lead breaks while the 'Located Events' are results generated by the source location program. The absolute errors range between 3.23 and 13.63 mm and have an average value of 8.90 mm for a constant velocity model of 4609 m/s.

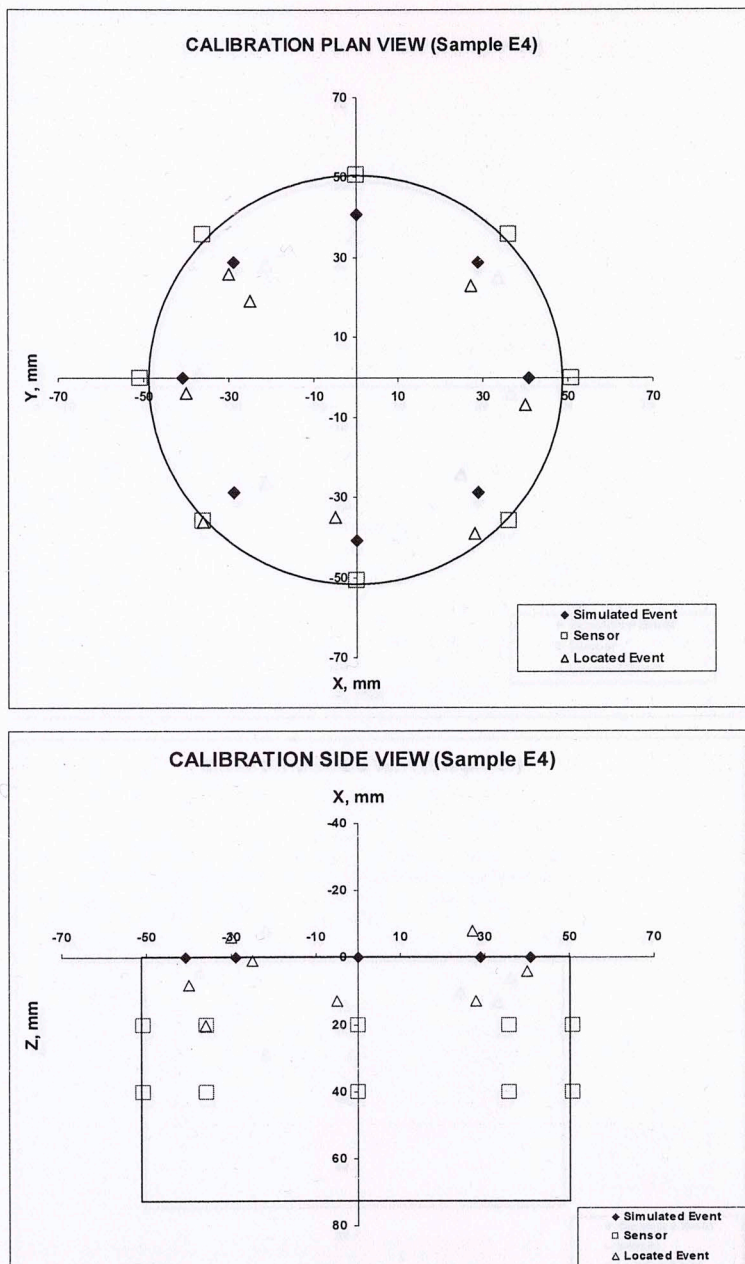


Figure 3.20: 3D location of acoustic emission (AE) associated with pencil lead breaks on sample E4. The 'simulated events' are the lead breaks while the 'Located Events' are results generated by the source location program. The absolute errors range between 6.74 and 33.18 mm and have an average value of 15.14 mm for a constant velocity model of 4635 m/s.

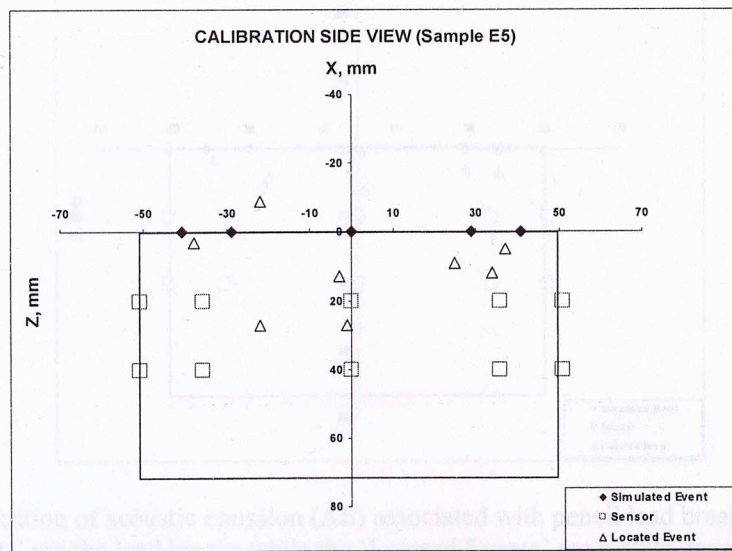
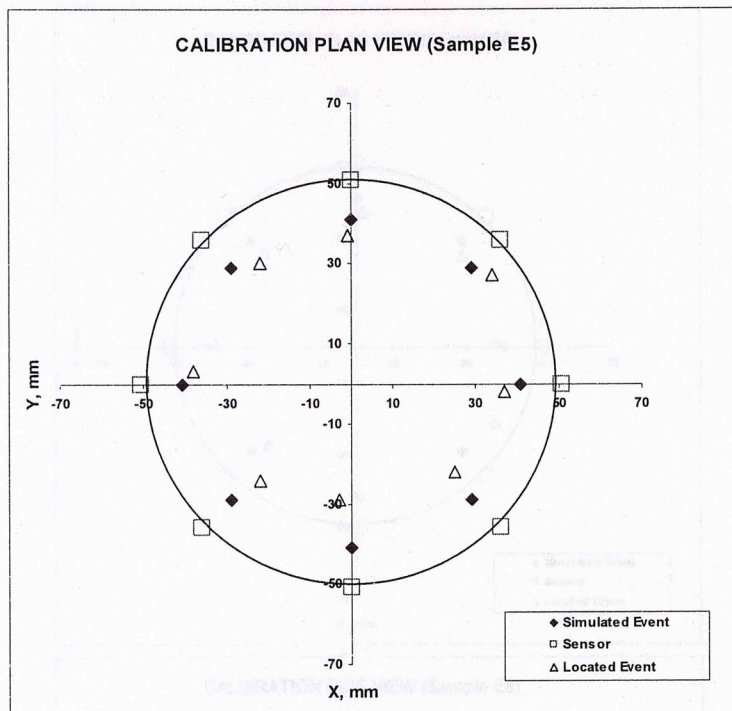


Figure 3.21: 3D location of acoustic emission (AE) associated with pencil lead breaks on sample E5. The 'simulated events' are the lead breaks while the 'Located Events' are results generated by the source location program. The absolute errors range between 5.08 and 28.27 mm and have an average value of 15.19 mm for a constant velocity model of 5094 m/s.

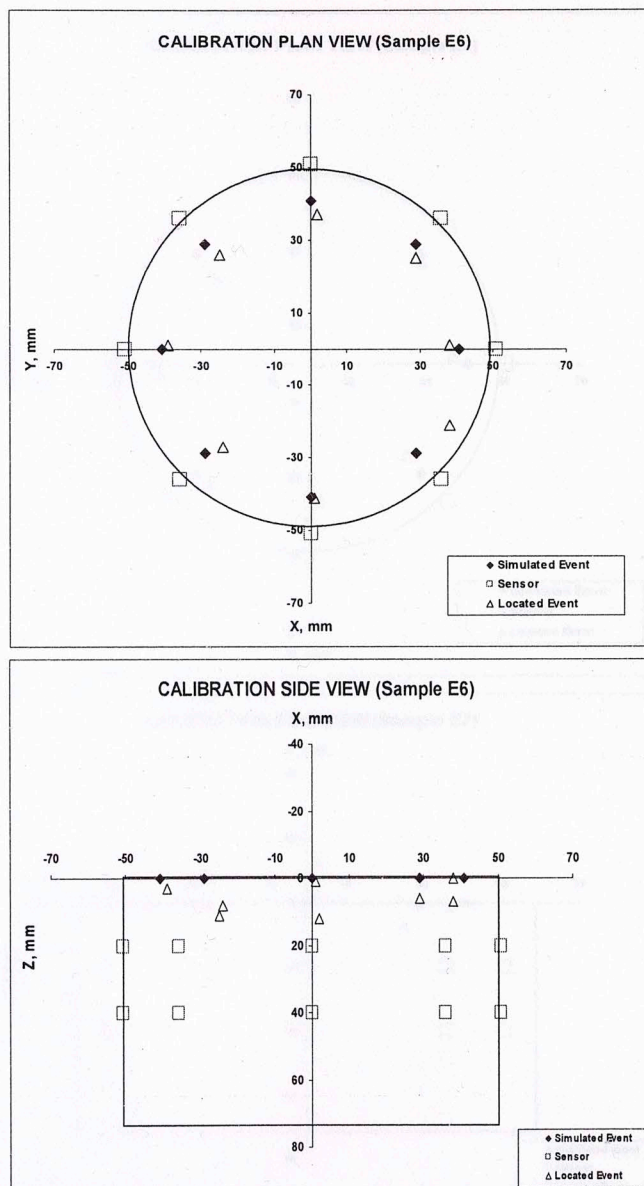


Figure 3.22: 3D location of acoustic emission (AE) associated with pencil lead breaks on sample E6. The 'simulated events' are the lead breaks while the 'Located Events' are results generated by the source location program. The absolute errors range between 1.43 and 12.75 mm and have an average value of 8.27 mm for a constant velocity model of 5099 m/s.

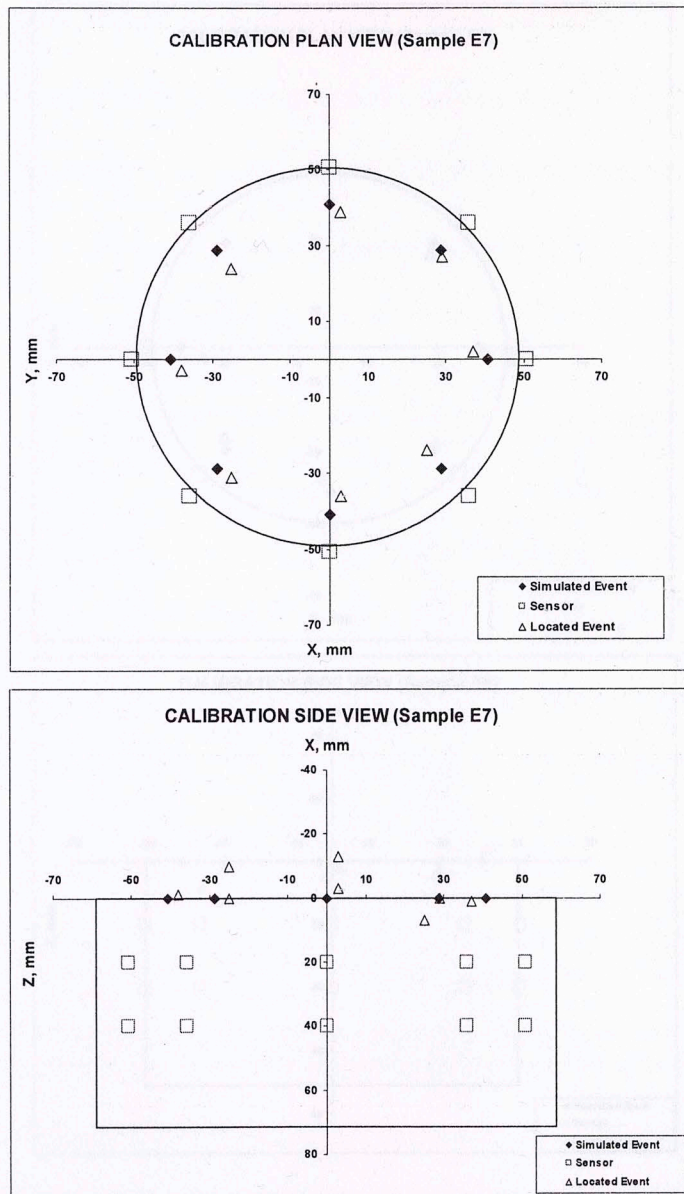


Figure 3.23: 3D location of acoustic emission (AE) associated with pencil lead breaks on sample E7. The 'simulated events' are the lead breaks while the 'Located Events' are results generated by the source location program. The absolute errors range between 1.86 and 13.46 mm and have an average value of 7.10 mm for a constant velocity model of 4764 m/s.

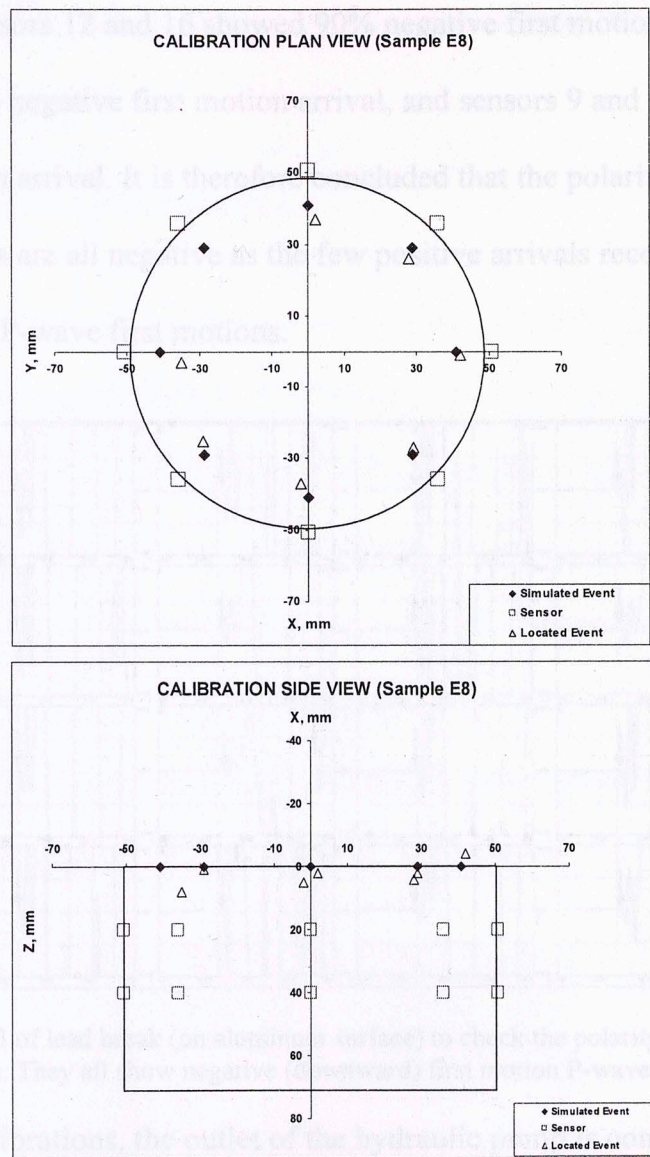


Figure 3.24: 3D location of acoustic emission (AE) associated with pencil lead breaks on sample E8. The 'simulated events' are the lead breaks while the 'Located Events' are results generated by the source location program. The absolute errors range between 2.73 and 10.33 mm and have an average value of 5.62 mm for a constant velocity model of 4966 m/s.

Also, the polarity responses of the sensors are determined with the Hsu-Nielsen source technique which produces a dilatational P-wave first motion (Sondergeld and Estey, 1982). The sensors are attached to a cylindrical aluminum sample in the same way they were attached to the rock samples. Ten pencil leads were broken at the center of the surface of the aluminum sample. A typical waveform recorded is shown in Figure 3.25. Out of the 10 events recorded, sensors 1-8, 14 and 15 showed 100% negative first motion

arrival polarity, sensors 12 and 16 showed 90% negative first motion arrival, sensors 10 and 13 showed 80% negative first motion arrival, and sensors 9 and 11 showed 70% negative first motion arrival. It is therefore concluded that the polarities of first p-wave arrival to the sensors are all negative as the few positive arrivals recorded may have been due to ambiguity in P-wave first motions.

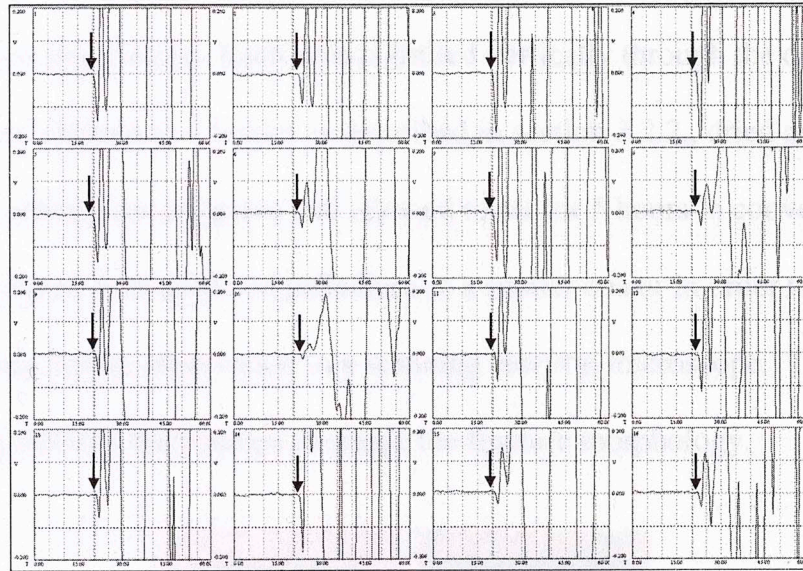


Figure 3.25: Event 3 of lead break (on aluminum surface) to check the polarity of the 16 B1025 AE sensors. They all show negative (downward) first motion P-wave polarity.

After the calibrations, the outlet of the hydraulic pump is connected to the steel mini-casing which is filled with fine-grained sands to reduce borehole volume. Setting the pump on ‘paired constant rate delivery’ mode, mineral oil is pumped into the mini-casing in order to pressurize and fracture samples E1, E4, E5 and E7. Samples E2, E3, E6 and E8 were pressurized by injecting water. The fluid injection schedule is the same for all the eight experiments. Fluid (oil or water) is injected into each sample at 2 cc/min for about 5 minutes and then stepped up to 4 cc/min for another 5.25 minutes. Acoustic emission signals associated with microcracking of the samples during the hydraulic

fracturing process are recorded over the same time span. The results and analyses are presented in the next chapter.

4.1 Pressure and AE Responses during Fluid Injection

3.4 Assessment of Fracture Morphology

After the hydraulic fracture treatment, the protruding part of the mini-casing is sawed off and a 1-inch core is drilled out of each sample (see Figure 3.26) for study in a scanning electron microscope. Each core is drilled vertically through the center of the sample. They are cleaned in a Soxhlet as described in section 3.2.2., dried and attached to holders using carbon paint adhesive and allowed to set for 5 hours in conventional oven. They are then coated with gold and palladium in a sputter coater in order to reduce electron charging during observation in a scanning electron microscope. They are placed in the scanning electron microscope to image the fracture morphology.

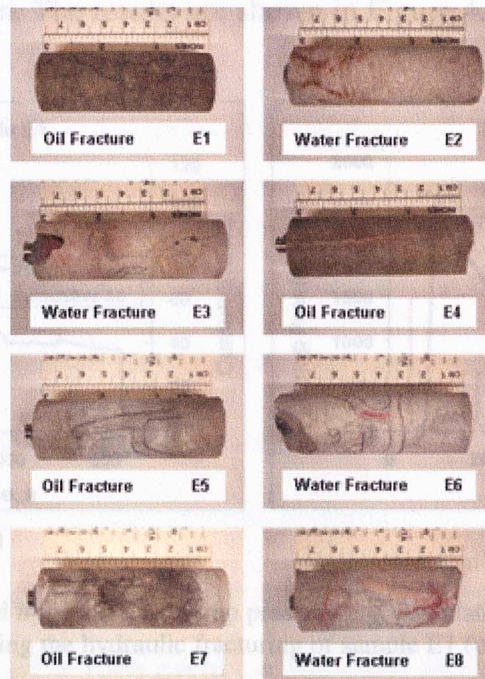


Figure 3.26: 1-inch diameter cores drilled through fractured samples. Note that the tubing is in the center of each core plug.

4 RESULTS, ANALYSES AND DISCUSSIONS

4.1 Pressure and AE Responses during Fluid Injection

In experiment 1 (hydraulic fracturing of sample E1 with mineral oil), fracturing occurred at a pressure of 2634 psi during the first phase of injection when the fluid flow rate was constant at 2 cm³ per minute. The time corresponding to this breakdown is 102.24 seconds. Prior to fracturing, the fluid pressure increased at a rate of 5.56 psi/s until the pressure is 141 psi at time of 77.16 s. Pressure is then increased more rapidly at 108 psi/s until breakdown at pressure, 2634 psi at 102.24 s. After the breakdown, the pressure declined initially at a rate of -27 psi/s and then -6.7 psi/s. During the 2nd stage of fluid injection, only 2 prominent pressure peaks, 1155 psi and 1196.7 psi, were recorded at 323.53 s and 365.58 s, respectively. There are 106 AE events induced in the first stage of fluid injection. The results are shown in Figure 4.1.

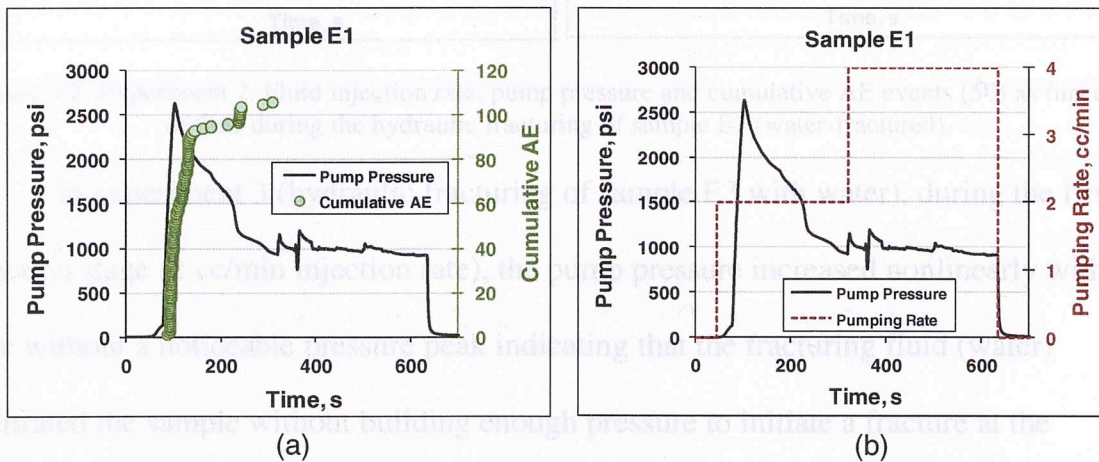


Figure 4.1: Experiment 1. Fluid injection rate, pump pressure and cumulative AE events (106) as functions of time during the hydraulic fracturing of sample E1 (oil-fractured).

In experiment 2 (hydraulic fracturing of sample E2 with water) multiple pressure peaked were observed. The first peak occurred at $t = 68$ s during the first injection stage at a pump pressure of 1229 psi. The second occurred during the second fluid injection stage at $t = 322.5$ s at a pump pressure of 1894.7 psi. The maximum pressurization rate just before the first and second fracture initiations were 135.3 and 210 psi/s, respectively. One AE event was recorded during the first pressure peak, 48 during the second and one after the treatment was terminated, giving a total of 50 AE events. The results are shown in Figure 4.2.

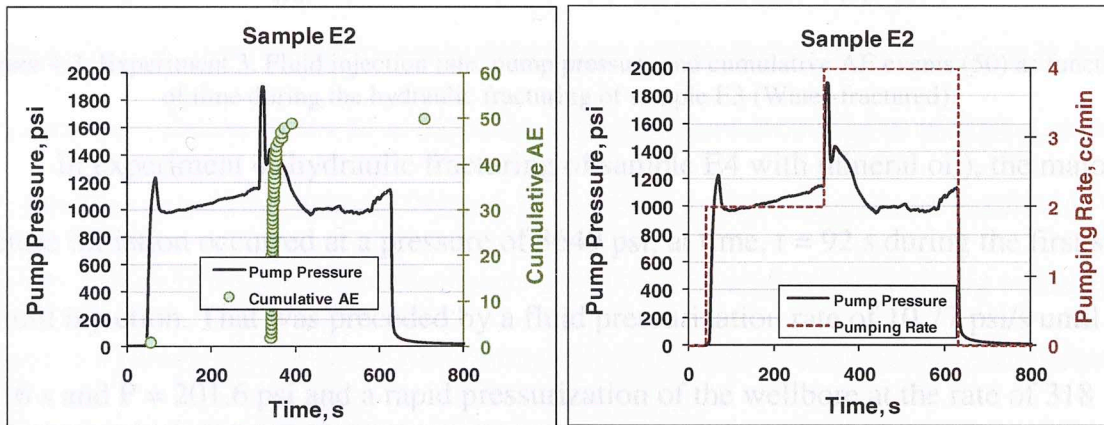


Figure 4.2: Experiment 2. Fluid injection rate, pump pressure and cumulative AE events (50) as functions of time during the hydraulic fracturing of sample E2 (water-fractured).

In experiment 3 (hydraulic fracturing of sample E3 with water), during the first injection stage (2 cc/min injection rate), the pump pressure increased nonlinearly with time without a noticeable pressure peak indicating that the fracturing fluid (water) infiltrated the sample without building enough pressure to initiate a fracture at the borehole wall. During the second injection stage, the rate of pressurization rose to 179 psi/s and the pressure peaked at 1504 psi at $t = 369$ s and another peak was recorded at 1600 psi at $t = 474$ s. One AE event was recorded at the onset of the second stage and 49

during the first breakdown. There are 50 AE events recorded altogether. The results are shown in Figure 4.3.

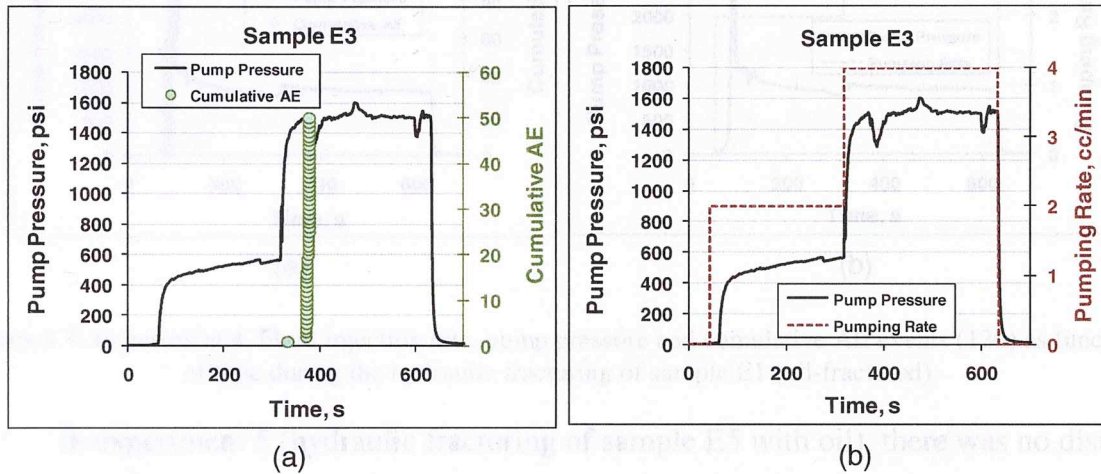


Figure 4.3: Experiment 3. Fluid injection rate, pump pressure and cumulative AE events (50) as functions of time during the hydraulic fracturing of sample E3 (Water-fractured).

In experiment 4 (hydraulic fracturing of sample E4 with mineral oil), the major fracture initiation occurred at a pressure of 3649 psi, at time, $t = 92$ s during the first stage of fluid injection. That was preceded by a fluid pressurization rate of 10.77 psi/s until $t = 80.16$ s and $P = 201.6$ psi and a rapid pressurization of the wellbore at the rate of 318 psi/s. After the breakdown, the pressure declined at a rate of - 856 psi/s. In the second stage of pumping, a maximum pressure of 1046 psi was recorded at $t = 319.5$ s. During the first stage of pumping, 113 AE events were recorded. Seven AE events were recorded during the second stage of the fluid injection. The results are shown in Figure 4.4

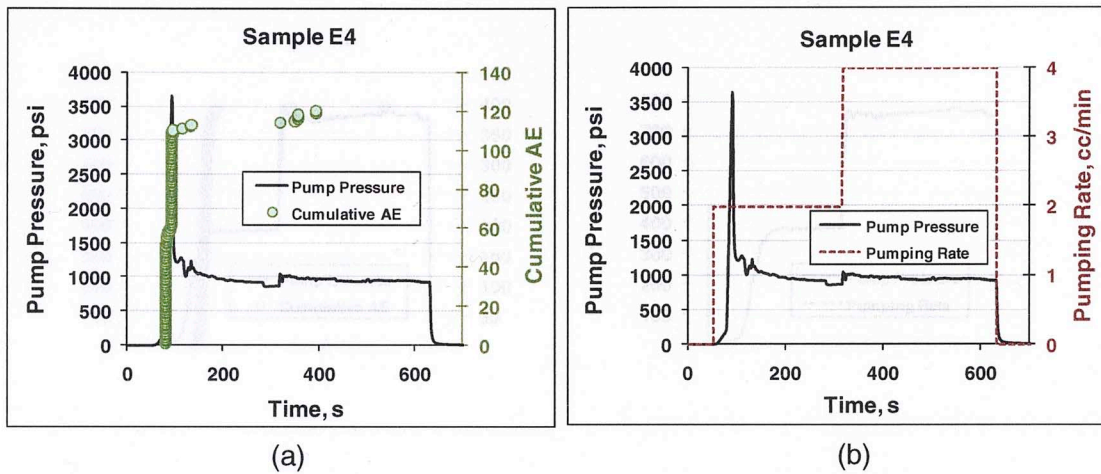


Figure 4.4: Experiment 4. Fluid injection rate, pump pressure and cumulative AE events (120) as functions of time during the hydraulic fracturing of sample E1 (oil-fractured).

In experiment 5 (hydraulic fracturing of sample E5 with oil), there was no distinct pressure peak in either of the two treatment stages unlike the pressure behaviors in the previous experiments. In the first stage, the pump pressure increased as pumping started and stabilizes at a value of about 380 psi. In the second stage the pressure stabilized between 738 and 776 psi. This behavior is due to the large open flaw running across the sample, which created a channel for treatment fluid to flow without building sufficient pressure for fracturing. During the first stage of fluid injection, as the pressure stabilizes at about 380 psi, 387 AE events were captured. Another 7 event were recorded at the beginning of the second pumping stage and one event at $t = 534$ s, after which the treatment was terminated at $t = 631$ s. Thus, 395 AE events were recorded altogether. The results are shown in Figure 4.5

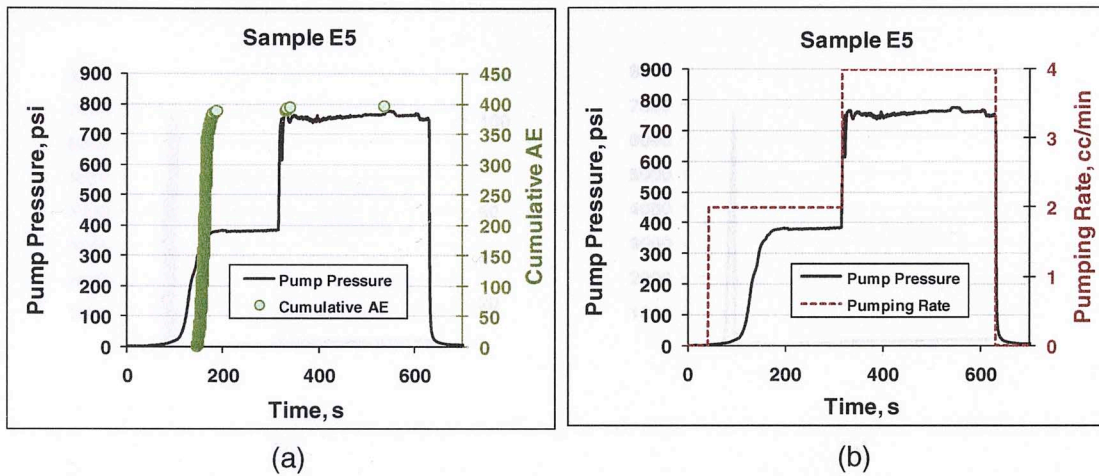


Figure 4.5: Experiment 5. Fluid injection rate, pump pressure and cumulative AE events (395) as functions of time during the hydraulic fracturing of sample E5 (oil-fractured).

In experiment 6 (hydraulic fracturing of sample E6 with water), during the first stage of fluid injection the pressure rose at a rate of 318 psi/s and fracture was initiated at a breakdown pressure of 6800 psi at time, $t = 97$ s. Immediately after the breakdown, the pressure declined at a rate of -1400 psi/s. During the second stage of fluid injection, the pressure rose from 98 to 215 psi before the treatment was terminated at $t = 634$ s. Ninety-eight AE events were recorded during this first treatment stage all coinciding with the duration of rapid pressure rise and eventual fracture initiation. The results are shown in Figure 4.6.

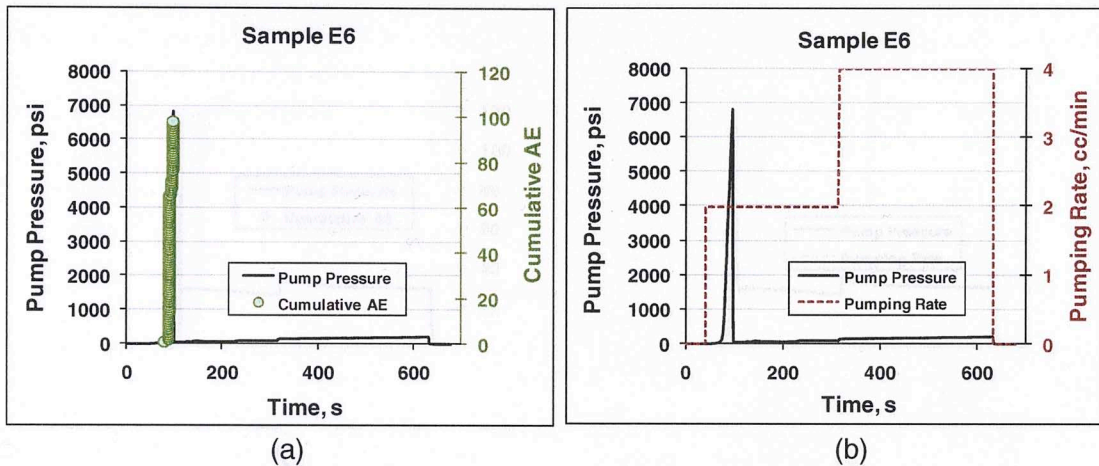


Figure 4.6: Experiment 6. Fluid injection rate, pump pressure and cumulative AE events (98) as functions of time during the hydraulic fracturing of sample E6 (Water-fractured).

In experiment 7 (hydraulic fracturing of sample E7 with mineral oil), during the first stage of oil injection pressure rose at a rate of 304 psi/s and fracture was initiated at a breakdown pressure of 3355 psi at time, $t = 98$ s. Immediately after the breakdown, the pressure declined at a rate of -875 psi/s. During the second stage of fluid injection, there was a step increase in pressure from 742 to 1007 psi and declined to 830 psi before the treatment was terminated. One hundred and fifteen (115) AE events were recorded during the first treatment stage, all coinciding with the duration of rapid pressure rise and eventual fracture initiation. The results are shown in Figure 4.7.

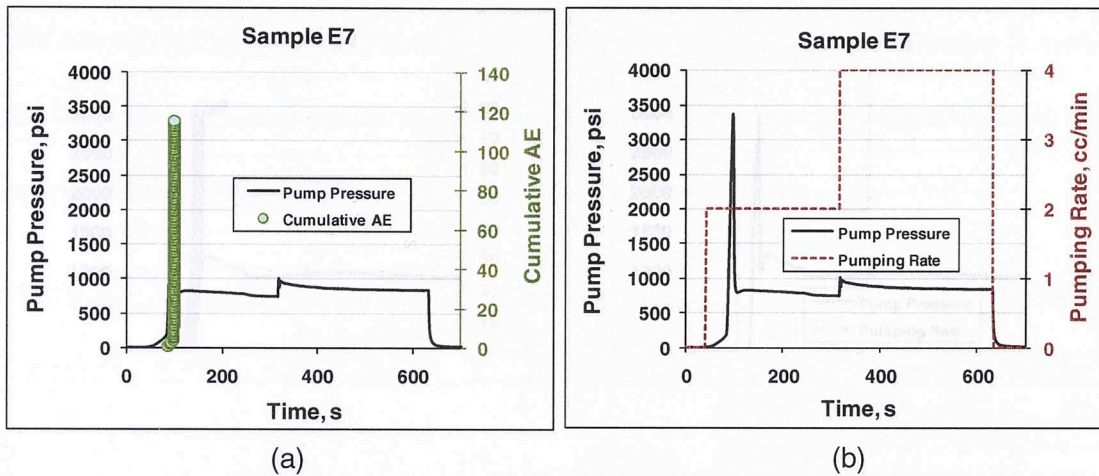


Figure 4.7: Experiment 7. Fluid injection rate, pump pressure and cumulative AE events (115) as functions of time during the hydraulic fracturing of sample E7 (oil-fractured).

In experiment 8 (hydraulic fracturing of sample E8 with water), during the first stage of water injection the pressure rose at a rate of 325 psi/s and fracture was initiated at 3 breakdown pressures (2348 psi at $t = 137$ s; 2592 psi at $t = 141$ s; and 2921 psi at $t = 146$ s) after which the pressure declined to 976 psi at a rate of -1000 psi/s. The pressure rises again, albeit less rapidly, to a value of 1204 psi at a rate of 27.5 psi/s. This is followed by a pressure decline at a rate of -2.5 psi/s to settle at a pressure of about 950 psi. The second stage of fluid injection did not produce any remarkable effect on the pressure behavior before the treatment was terminated at time, $t = 692$ s. Eighty AE events were recorded during this first treatment stage all coinciding with the duration of rapid pressure rise and eventual fracture initiation. The results are shown in Figure 4.8.

of dolomite content, porosity and permeability. The dependence of hydraulic fracture breakdown pressures on fluid and sample properties as seen in Figure 4.9 can be attributed to the effect of fluid permeation into the sample which tends to increase its pore pressure (i.e., reduce its effective stress) and create shear microfractures in the process (Matsunaga et al., 1993). There is also greater microseismic activities (AE events) with oil-fractured than with water-fractured samples which implies that more

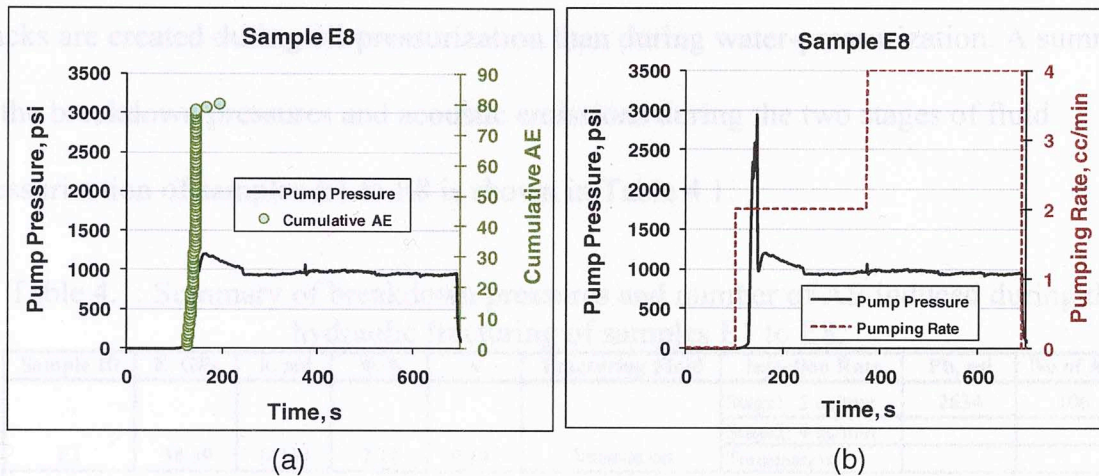


Figure 4.8: Experiment 8. Fluid injection rate, pump pressure and cumulative AE events (80) as functions of time during the hydraulic fracturing of sample E8 (water-fractured).

From the foregoing, it is apparent that samples with comparative properties and treatment parameters breakdown at higher pressures, P_b , when oil (37-cp) is used as the treatment fluid than when water (1-cp) is used. The increases are 28% between samples E1 and E2, 59% between E3 and E4 and 13 % between E7 and E8. Samples E5 and E6 have been deliberately omitted from this analysis because E5 did not show any distinctive breakdown and so could not be compared to its pair, sample E6. Similar increase (40%) in breakdown pressure with viscosity has been observed by Matsunaga et al. (1993) when fracturing with water and oil (70-cp). Also, the P_b appears to increase with increase calcite content and Young's Modulus (this is more obvious in oil-fractured samples than in water-fractured samples). On the other hand, P_b decreases with increase in the amount of dolomite content, porosity and permeability. The dependence of hydraulic fracture breakdown pressures on fluid and sample properties as seen in Figure 4.9 can be attributed to the effect of fluid permeation into the sample which tends to increase its pore pressure (i.e. reduce its effective stress) and create shear microfractures in the process (Matsunaga et al., 1993). There is also greater microseismic activities (AE events) with oil-fractured than with water-fractured samples which implies that more

cracks are created during oil-pressurization than during water-pressurization. A summary of the breakdown pressures and acoustic emissions during the two stages of fluid pressurization of samples E1 to E8 is shown in Table 4.1.

Table 4.1: Summary of breakdown pressures and number of AE induced during the hydraulic fracturing of samples E1 to E8.

Sample ID	E, GPa	k, md	ϕ , %	ν	Fracturing Fluid	Injection Rate	Pb, psi	No of AE
E1	38.39	0.234	7.10	0.197	Mineral oil	Stage1: 2 cc/min	2634	106
						Stage2: 4 cc/min		
						Termination		
								106
E2	38.23	0.184	7.10	0.184	Water	Stage1: 2 cc/min	1229	1
						Stage2: 4 cc/min	1895	48
						Termination		1
								50
E3	50.38	0.175	5.77	0.173	Water	Stage1: 2 cc/min		
						Stage2: 4 cc/min	1504	50
						Termination		
								50
E4	50.96	0.061	3.59	0.179	Mineral oil	Stage1: 2 cc/min	3649	113
						Stage2: 4 cc/min		7
						Termination		
								120
E5	58.97	0.002	2.90	0.241	Mineral oil	Stage1: 2 cc/min		387
						Stage2: 4 cc/min		8
						Termination		
								395
E6	49.90	0.010	3.21	0.304	Water	Stage1: 2 cc/min	6800	98
						Stage2: 4 cc/min		
						Termination		
								98
E7	44.98	0.004	2.42	0.291	Mineral oil	Stage1: 2 cc/min	3355	115
						Stage2: 4 cc/min		
						Termination		
								115
E8	39.81	0.006	2.43	0.351	Water	Stage1: 2 cc/min	2921	80
						Stage2: 4 cc/min		
						Termination		
								80

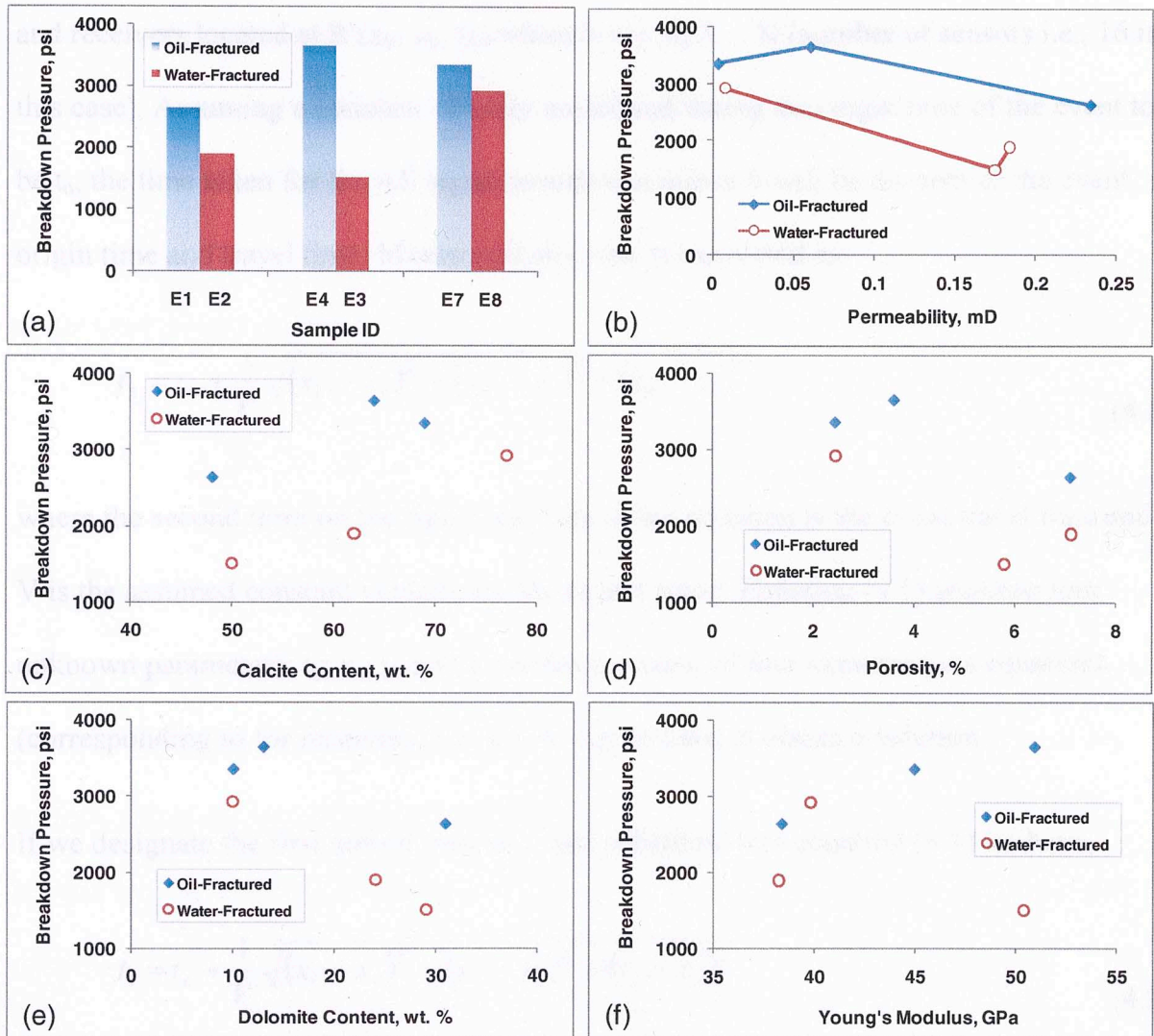


Figure 4.9: Factors controlling breakdown pressure. Breakdown pressure varies directly as fluid viscosity (a), calcite content (c), and Young's modulus (E) but inversely as rock permeability (b), porosity (d) as well as dolomite content (e).

4.2 Analyses of Experiment Results

4.2.1 AE Event Location

For each event, the arrival time to each of the 16 sensors was manually picked and then, a constant velocity model obtained from calibration was used to locate the events.

Typically, this involves setting the source of the acoustic emission (AE) as $S(x_s, y_s, z_s)$

and receivers located at R (x_k, y_k, z_k) where $k = 1, 2, 3 \dots N$ (number of sensors i.e., 16 in this case). Assuming a constant velocity model and taking the origin time of the event to be t_0 , the time taken for the AE signal to arrive at sensor k will be the sum of the event origin time and travel time. Mathematically, this is expressed as

$$t_k = t_0 + \frac{1}{V} \sqrt{(x_k - x_s)^2 + (y_k - y_s)^2 + (z_k - z_s)^2} \quad (4.1)$$

where the second term on the right hand side of the equation is the event travel time and V is the assumed constant velocity for the elastic wave. Equation (4.1) contains four unknown parameters: t_0, x_s, y_s and z_s so that a system of four simultaneous equations (corresponding to for receivers, i.e., $k = 4$) can be used to obtain a solution.

If we designate the first arrival time as t_1 and substitute into equation (4.1) we have,

$$t_1 = t_0 + \frac{1}{V} \sqrt{(x_1 - x_s)^2 + (y_1 - y_s)^2 + (z_1 - z_s)^2} \quad (4.2)$$

Subtracting equation (4.2) from (4.1), we have

$$\Delta t_k = t_k - t_1 \quad (4.3)$$

$$\Delta t_k = \frac{1}{V} \left[\sqrt{(x_k - x_s)^2 + (y_k - y_s)^2 + (z_k - z_s)^2} - \sqrt{(x_1 - x_s)^2 + (y_1 - y_s)^2 + (z_1 - z_s)^2} \right] \quad (4.4)$$

for $k = 2, 3, 4$.

Generally, in earthquake seismology, more than four sensors are used to obtain an overdetermined solution (Lay and Wallace, 1995). Thus, for a number of sensors, N ,

equation (4.3) gives the arrival times at $N - 1$ sensor locations relative to the first or least arrival time and can be termed as $\Delta t_{k, obs}$. By assuming an initial source location we can compute the relative arrival times from equation (4.4) as $\Delta t_{k, calc}$ (PAC, 2004). The error resulting from the difference between the two relative arrival times can then be minimized using multiple linear regression technique by expressing it as (PAC, 2004)

$$\chi^2 = \sum_{k=1}^{N-1} (\Delta t_{k, obs} - \Delta t_{k, calc})^2 \quad (4.5)$$

For the purpose of our experiments, the Cartesian coordinate system is used. The x – axis runs from East to West; y – axis is directed from South to North; and the z – axis is mutually perpendicular to both the x – and y – axis and points downwards (from the surface of the sample) along the length (depth) of the sample, thereby forming a right-handed system. Fracture orientations are reported as azimuths measured clockwise and referred to North.

Out of the 106 events detected in sample E1, only 48 could be located within the sample. The rest had poor quality signals that made arrival time picking impossible, located outside the sample, or the location program could not converge to a solution. The plots of AE event hypocenters and the sensor locations are shown in Figure 4.10; only those events located within the sample are plotted. Two planes of AE locations can be identified as having azimuths, 45° and 53° and they span an estimated height of 50 mm. Physical observation of the fractured sample ($z = 0$ plane) shows the hydraulic fracture oriented 85° and passes through the center of the sample as seen in Figure 4.10.

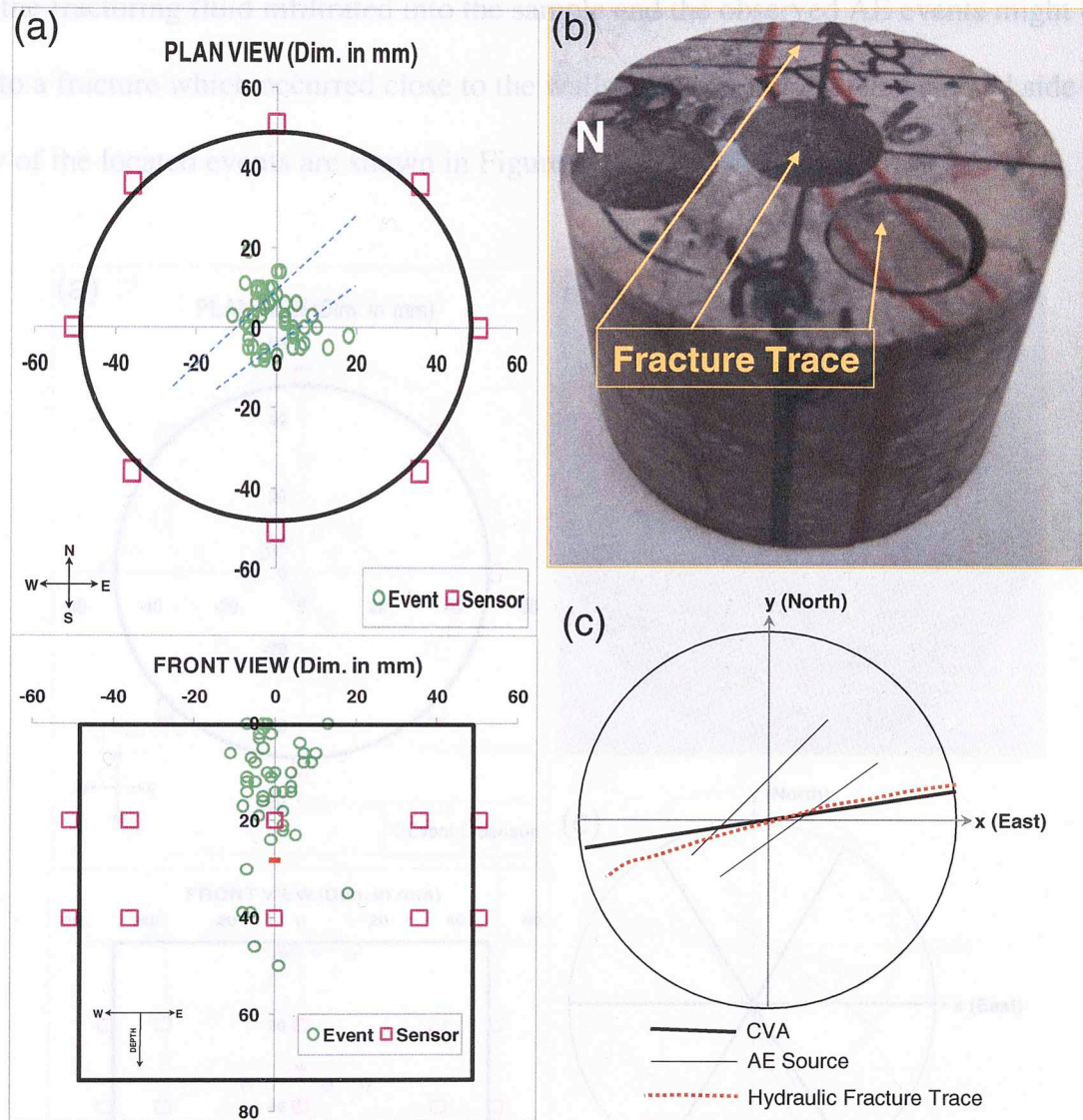


Figure 4.10: Plan and front views of AE events (48/106) induced in sample E1 (fractured with mineral oil) during hydraulic fracturing. Dark lines define sample outlines and broken lines are the estimated orientations of AE locations. A post-fracture picture of the sample is also shown.

In experiment 2 (water-fracture), 13 of 50 recorded events were located within the sample. The AE events are located close to the top of the sample and a close examination reveals two planes of AE locations trending in the azimuths, 37° and 43° and spanning an estimated height of 35 mm. Physical observation of the sample does not show any visible fracture at a radius of 0.5" from the borehole axis. However, colored dye, injected into the fracture after treatment, could be seen concentrated on a plane oriented 160° showing

that the fracturing fluid infiltrated into the sample and the observed AE events might be due to a fracture which occurred close to the walls of the wellbore. The plan and side view of the located events are shown in Figure 4.11.

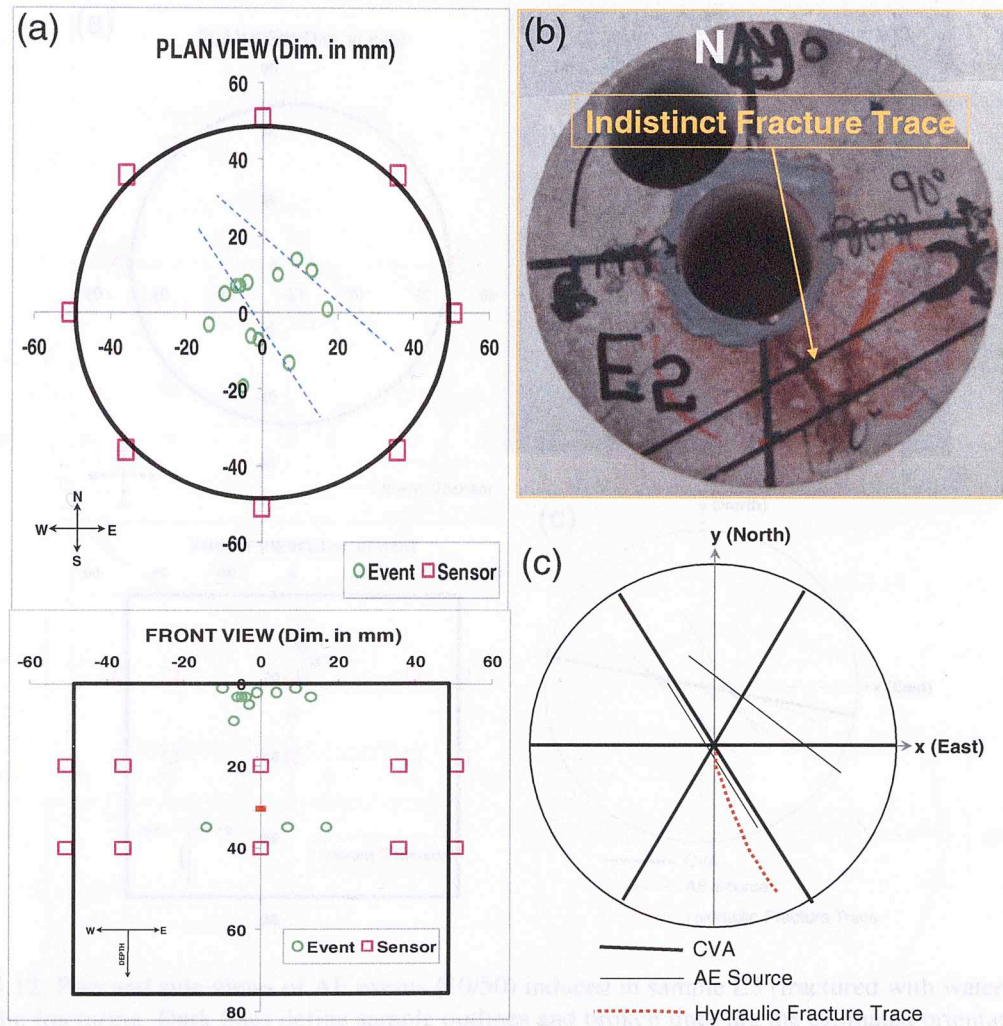


Figure 4.11: Plan and side views of AE events (13/50) induced in sample E2 (fractured with water) during hydraulic fracturing. Dark lines define sample outlines and broken lines are the estimated orientations of AE locations. A post-fracture picture of the sample is also shown.

Similarly, 10 of 50 recorded AE events during the hydraulic fracturing of sample E3 (water-fractured) were successfully located within the sample. They are clustered in the 1st and 2nd quadrants as shown in Figure 4.12. The fracture is single-winged and aligned in an almost West-East direction. Two planes of AE locations can be identified

trending in the azimuth 313° and 298° and they span an estimated height of 40 mm.

Physical observations on the fractured sample confirmed the existence of a fracture plane in the 2nd (south-east) quadrant trending 125° and 105° .

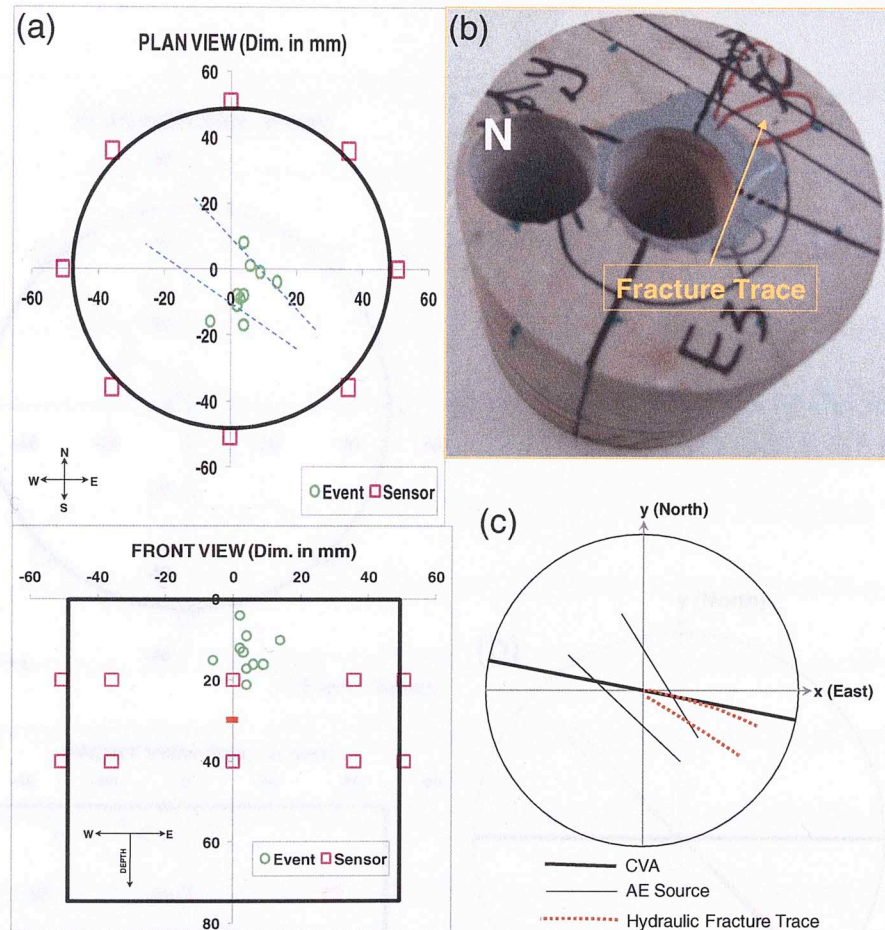


Figure 4.12: Plan and side views of AE events (10/50) induced in sample E3 (fractured with water) during hydraulic fracturing. Dark lines define sample outlines and broken lines are the estimated orientations of AE locations. A post-fracture picture of the sample is also shown.

In experiment 4 (sample E4 was fractured with mineral oil) 14 out of a total of 120 AE events were located within the sample as shown in Figure 4.13. The signals from sensors 1 through 4 were so attenuated that they could not be used for hypocenter determination. Thus, only the arrival times of signals from channels 5-16 were picked. The AE events depict an asymmetrical, bi-winged hydraulic fracture aligned in the NW-SE direction. Specifically, the AE location trends 315° and spans a height of

approximately 40 mm. Physical observation of the fractured sample ($z = 0$ plane) shows the hydraulic fracture oriented 315° and passes through the center of the sample. A picture was not taken because the sample broke apart during post-fracture core plugging.

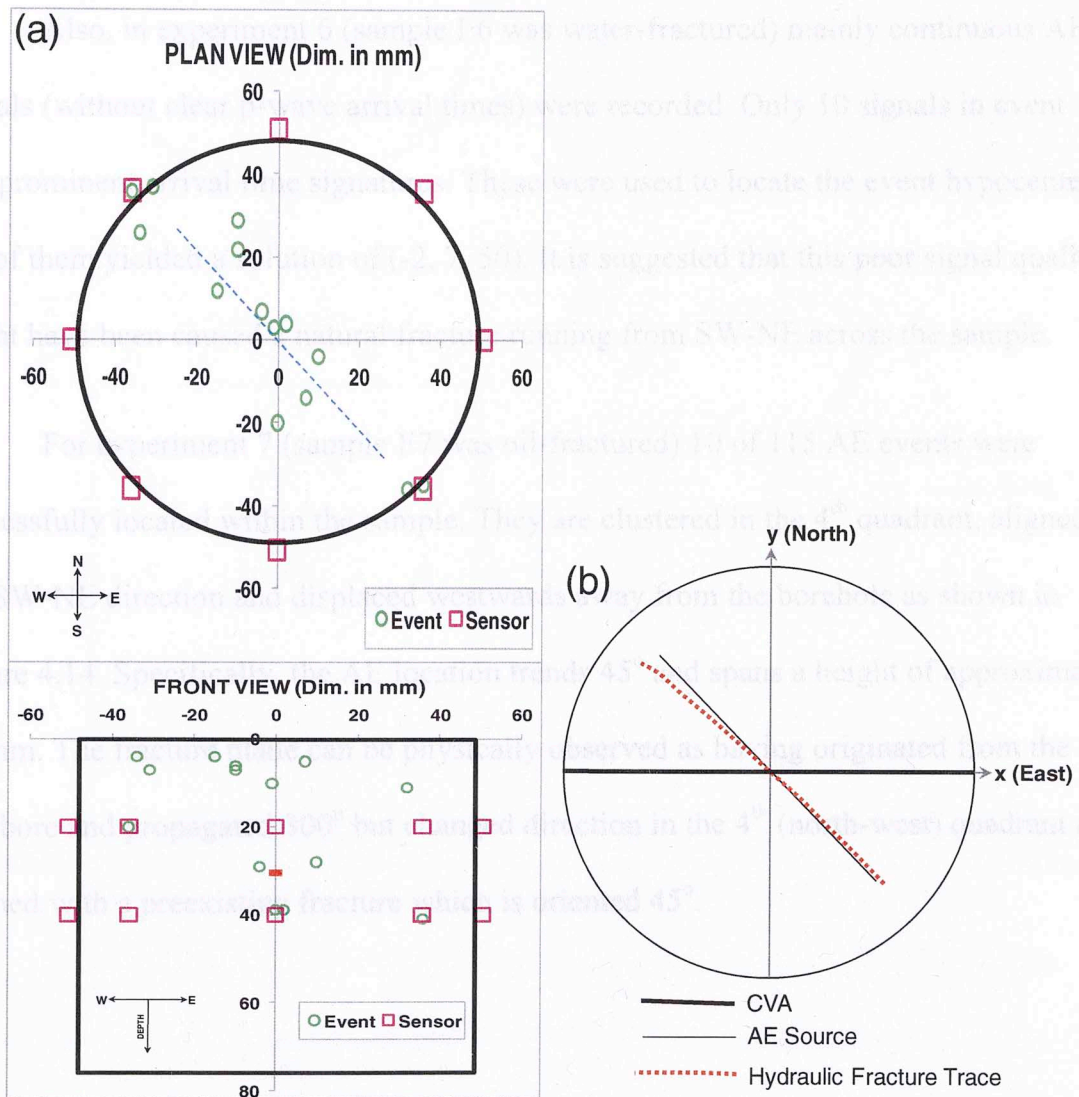


Figure 4.13: Plan and side views of AE events (14/120) induced in sample E4 (fractured with mineral oil) during hydraulic fracturing. Dark lines define sample outlines and the broken line is the estimated orientation of AE locations.

In experiment 5 (sample E5 was oil-fractured) mainly continuous AE signals (without clear p-wave arrival times) were recorded. Only events number 389, 390, 392,

393 and 394 showed identifiable arrival times in 7, 8, 6, 8 and 7 channels, respectively. The arrival times were used to locate the events which all occurred at the coordinate (-35.92, 35.92, 20). A pre-existing fracture ran through this point and is also the location of sensor 15 and might have attenuated the signals beyond their detection level.

Also, in experiment 6 (sample E6 was water-fractured) mainly continuous AE signals (without clear p-wave arrival times) were recorded. Only 10 signals in event 1 had prominent arrival time signatures. These were used to locate the event hypocenters. All of them yielded a solution of (-2, 7, 50). It is suggested that this poor signal quality might have been caused by a natural fracture running from SW-NE across the sample.

For experiment 7 (sample E7 was oil-fractured) 10 of 115 AE events were successfully located within the sample. They are clustered in the 4th quadrant, aligned in the SW-NE direction and displaced westwards away from the borehole as shown in Figure 4.14. Specifically, the AE location trends 45° and spans a height of approximately 40 mm. The fracture plane can be physically observed as having originated from the wellbore and propagated 300° but changed direction in the 4th (north-west) quadrant and aligned with a preexisting fracture which is oriented 45°.

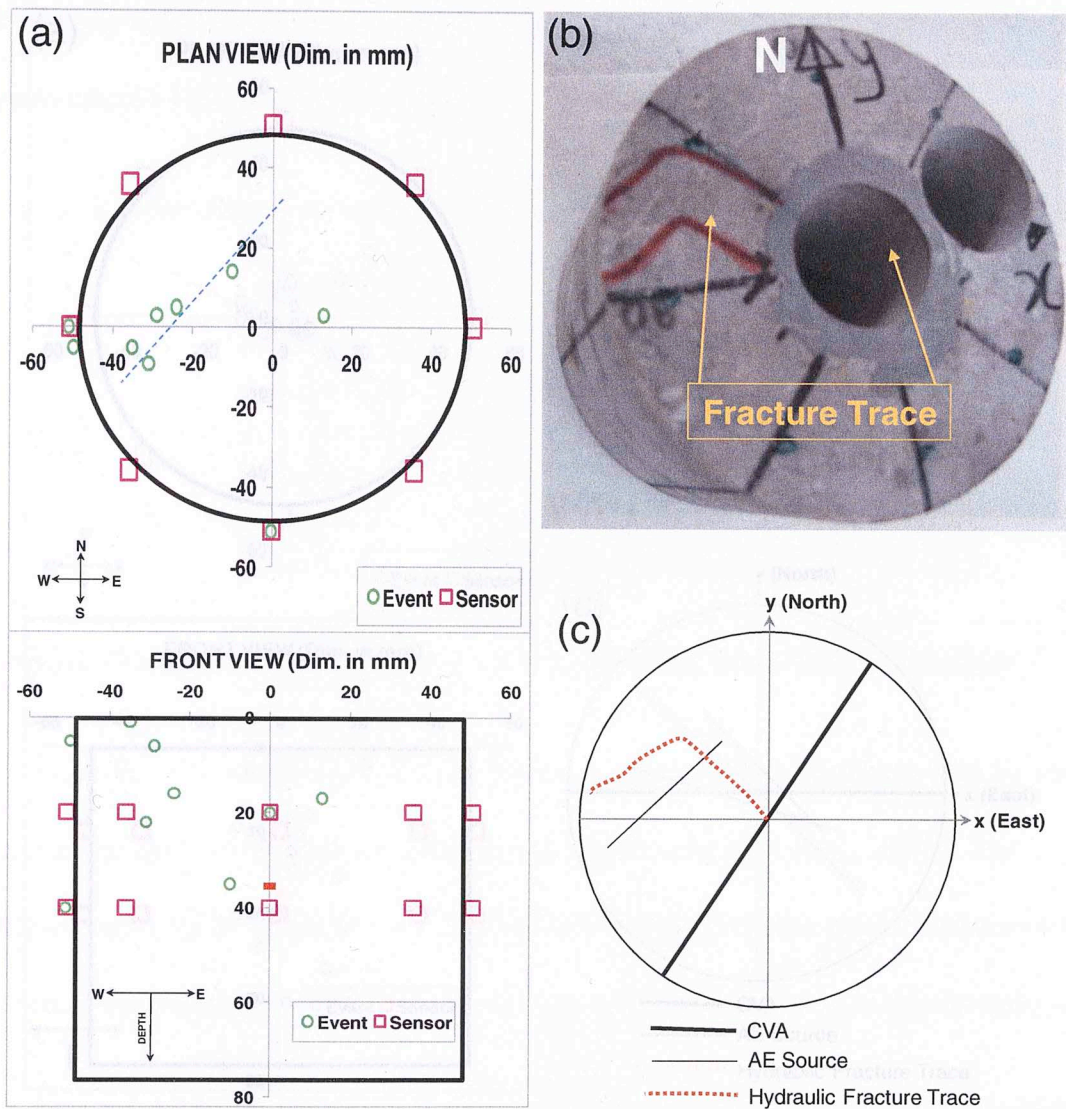


Figure 4.14: Plan and side views of AE events (10/115) induced in sample E7 (fractured with mineral oil) during hydraulic fracturing. Dark lines define sample outlines and the broken line is the estimated orientation of AE locations. A post-fracture picture of the sample is also shown.

Finally, for experiment 8 (sample E8 was fractured with water) 16 of 80 AE events were located within the sample. The located events are clustered around the borehole as shown in Figure 4.15 with a tendency to align in the SE-NW direction except for events 1, 15 and 76 which were in different quadrants. Two planes of AE locations can be identified trending in the 325° and 300° and they span an estimated height of 60 mm. This is evident from the physical observation of the sample with the fracture plane on the 2nd (south-east) and 4th (north-west) quadrants. The fracture trace trends 315° .

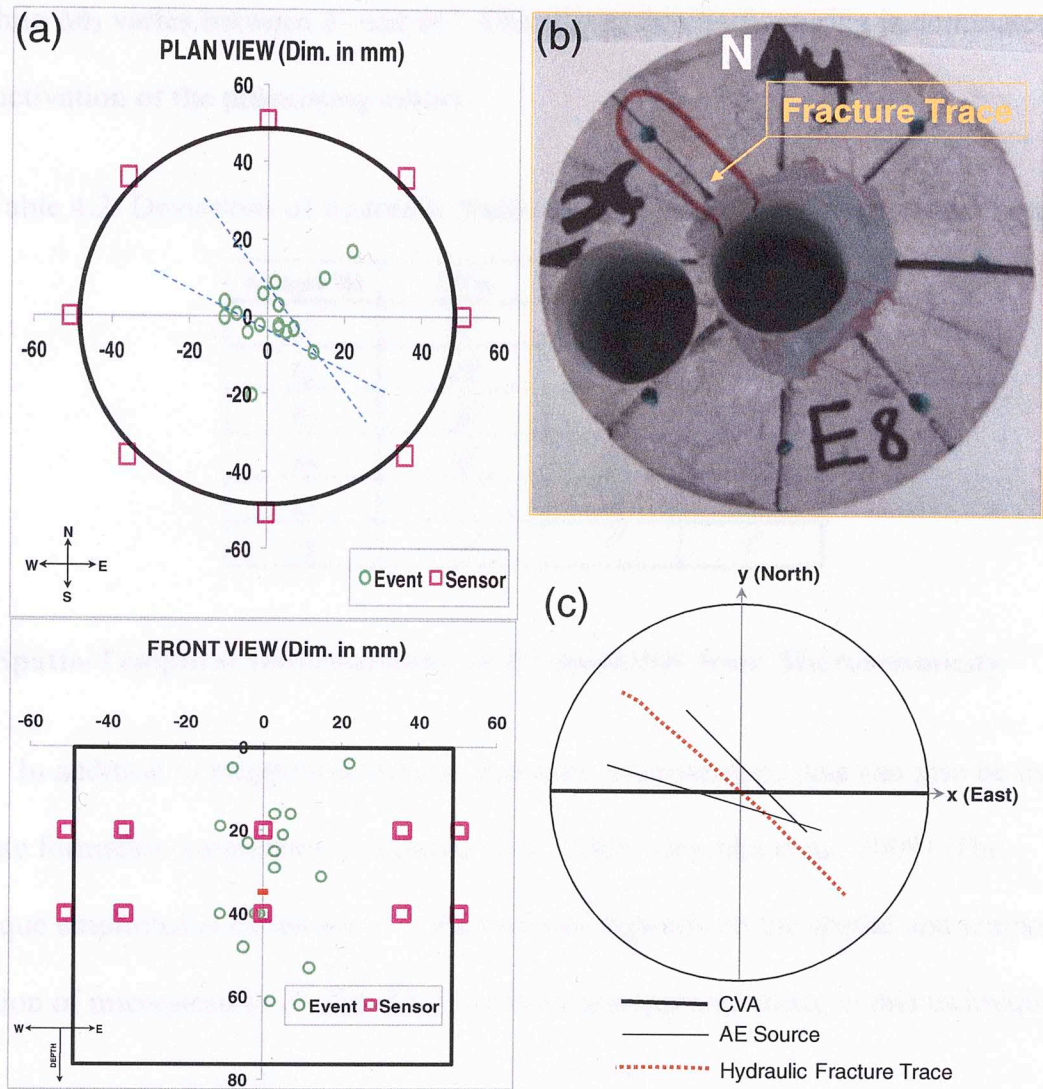


Figure 4.15: Plan and side views of AE events (16/80) induced in sample E8 (fractured with water) during hydraulic fracturing experiment. Dark lines define sample outlines and broken lines are the estimated orientations of AE locations. A post-fracture picture of the sample is also shown.

In summary, the AE source locations can be seen as mirroring the physical fractures observed in the samples within certain limits of error. The angular deviations, $\Delta\theta_1$ and $\Delta\theta_2$, of the average AE source locations and the visible fracture traces, respectively, from the predominant crack orientations (obtained from the CVA results of section 4.2.3) within the samples are shown in Table 4.2. The hydraulic fractures are clearly seen as being subparallel to the preexisting cracks as $\Delta\theta_1$ varies between 0° and

45° while $\Delta\theta_2$ varies between 3° and 45°. Thus the hydraulic fracturing is dominated by the reactivation of the preexisting cracks.

Table 4.2: Deviations of hydraulic fractures from preexisting crack orientations.

Sample ID	CVA	$\Delta\theta_1$	$\Delta\theta_2$
E1	85°	0°	36°
E2	150°	10°	10°
E3	100°	5°	22°
E4	90°	45°	45°
E7	35°	10°	10°
E8	130°	5°	3°

4.2.2 Spatio-Temporal Determination of Permeability from Microseismicity

In addition to mapping hydraulic fractures, microseismic data can also be used to evaluate formation permeability (Shapiro et al., 2006; Grechka et al., 2009). The technique employed is called the *r – t method* and depends on the spatial and temporal evolution of microseismic clouds. There are two assumptions made in this technique:

- (i) The induced hydraulic fracture is vertical with geometry defined by its width, height and half length.
- (ii) Most of the fluid injected into the hydraulic fracture leaks off into the formation and is responsible for the microseismicity recorded during the treatment, i.e. the fluid pressure decreases the effective pressure leading to failure.

According to the r-t method, the in situ formation permeability, k^* , is given as

$$k^* = \frac{\mu}{128\phi cD} \left(\frac{q}{h_f \Delta P} \right)^2 \quad (4.6)$$

where μ and c are the viscosity and compressibility of the reservoir fluid, respectively; ϕ and D are the porosity and apparent diffusivity of the formation, respectively; q and ΔP are the average fluid injection rate and effective fracture pressure, respectively; and h_f is the average fracture height. The apparent diffusivity, D , is related to the forward front of the microseismic cloud, $r_{\mu s}(t)$ and the time, t_s , when fracturing fluid injection into the formation starts, by:

$$r_{\mu s}(t) = \sqrt{4\pi D(t - t_s)} \quad (4.7)$$

In order to determine the value of apparent D used in equation (4.6) to compute the formation permeability, k^* , radial distances from AE hypocenters to the points of fluid injection are plotted as a function of time (see Figure 4.16) and enveloped with the forward front of microseismic cloud, $r_{\mu s}(t)$. The permeability is then computed with the assumption that the fluid in the core samples used for our experiments is air (at atmospheric pressure) with viscosity and compressibility at 1 atm and 70°F as 2×10^{-5} Pa.s and 7×10^{-6} Pa⁻¹, respectively. Other parameters for our computation of permeability values are shown in Table 4.3. The average fluid injection rates and pressures are computed as the integral of the respective curves divided by the time between the start of fluid injection and the last AE event.

AE	ϕ , %	D , m ² /s	μ , Pa.s	c , Pa ⁻¹	q , m ³ /s	ΔP , Pa	k^* , mD	k , pD
E1	10	1.07	2.0	7.0	2.01	37.0	387	34
E2	10	1.07	2.0	7.0	0.23	391.8	82.8	104
E3	10	1.07	2.0	7.0	0.17	126.4	126.0	173
E4	10	1.07	2.0	7.0	1.19	36.1	15	31
E7	10	1.07	2.0	7.0	1.20	10.0	10.0	1
E8	10	1.07	2.0	7.0	2.00	9.1	4.0	4

The values of permeability, k^* (see Table 4.2) computed from microseismic triggering fronts are several orders of magnitude lower than those from laboratory

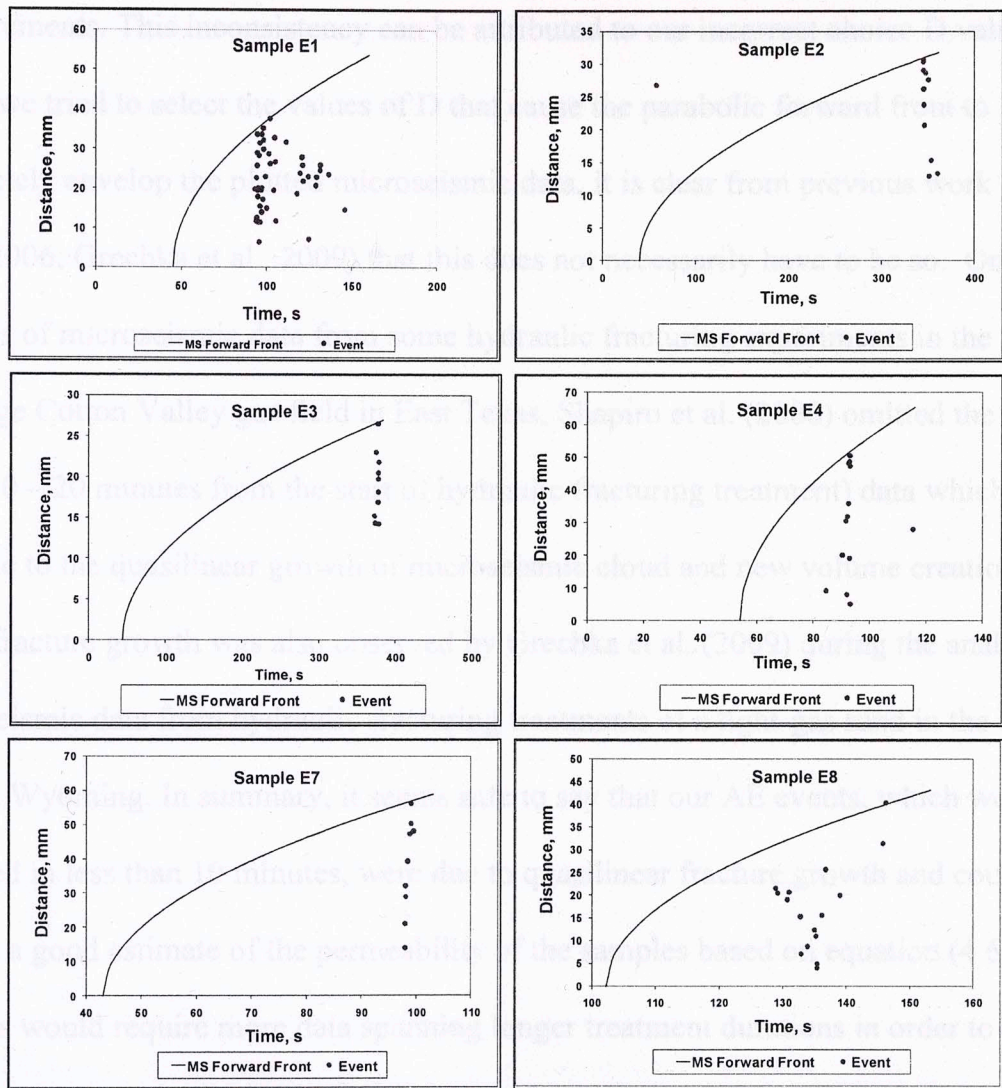


Figure 4.16: Plots of microseismic (AE) forward fronts enveloping their respective distances from AE sources in samples E1 – E4, E7 and E8 to the points of fluid injection.

Table 4.3: Parameters for computing permeability, k^* from AE and their results

Sample ID	Input Data					$w_f, \mu\text{m}$	k^*, nD	$k, \mu\text{D}$
	$q, \text{cc/min}$	$\Delta P, \text{psi}$	h_f, mm	$\phi, \%$	$D, \text{mm}^2/\text{s}$			
E1	2.00	1392	40	7.10	2.00	27.0	38.2	234
E2	4.00	1076	30	7.10	0.25	240.0	82.8	184
E3	2.36	621	30	5.77	0.17	129.4	120.0	175
E4	2.00	960	40	3.59	5.50	20.8	1.8	61
E7	2.00	530	40	2.42	4.60	19.0	10.0	4
E8	2.00	720	50	2.43	2.90	9.4	4.0	6

The values of permeability, k^* (see Table 4.2) computed from microseismic triggering fronts are several orders of magnitude lower than those from laboratory

measurements. This inconsistency can be attributed to our incorrect choice D values. While we tried to select the values of D that cause the parabolic forward front to completely envelop the plotted microseismic data, it is clear from previous work (Shapiro et al., 2006; Grechka et al., 2009) that this does not necessarily have to be so. On the analysis of microseismic data from some hydraulic fracturing experiments in the Carthage Cotton Valley gas field in East Texas, Shapiro et al. (2006) omitted the early time (10 – 20 minutes from the start of hydraulic fracturing treatment) data which they attribute to the quasilinear growth of microseismic cloud and new volume creation. This initial fracture growth was also observed by Grechka et al. (2009) during the analysis of microseismic data from hydraulic fracturing treatments of a tight-gas sand in the Pinedale field in Wyoming. In summary, it seems safe to say that our AE events, which were recorded in less than 10 minutes, were due to quasilinear fracture growth and could not give us a good estimate of the permeability of the samples based on equation (4.6). Such analysis would require more data spanning longer treatment durations in order to be certain that the microseismicity induced is due to fluid leak-off effects. However, we can compute the average fracture width, w_f , resulting from the quasilinear fracture growth by using a simple model of fracture growth resulting from the volume balance of an incompressible treatment fluid (Shapiro et al., 2006). Based on the volume balance of the fracturing fluid, the average fracture half length, $L(t)$ is given as

$$L(t) = \frac{qt}{4h_f C_L \sqrt{2t} + 2h_f w_f} \quad (4.8)$$

where q = average fluid injection rate; t = average fluid injection time; h_f = average fracture height; C_L = fluid leak-off coefficient; and w_f = average fracture width. The

initial fracture growth is contributed by the 2nd term in the denominator of equation (4.8) which assumes that there is minimal fluid leak-off into the rock samples. Thus, equation (4.9) reduces to

$$L(t) = \frac{qt}{2h_f w_f} \quad (4.9)$$

which enables the average fracture width, w_f , of our samples to be calculated (based on a fracture half length of ½ inch) (see Table 4.2). Apart from experiment 2, the fracture widths (9 – 129 μm) computed for the hydraulic fractures are comparable to the physically observed fracture widths (5 – 70 μm).

4.2.3 Focal Mechanism Solutions (FMS)

One of the reasons for determining the focal mechanisms of micro-earthquakes induced during hydraulic fracturing is to effectively characterize the orientations of pre-existing fracture planes on which slip is presumed to occur. However, as explained in section 2.5, there are two nodal planes defined by the double-couple source model. One is the fault plane on which slip occurs while the other is an auxiliary plane that does not have a real scientific or engineering application. So we use data from other sources like the CVA, AE locations or physical observations of the samples to determine which of the nodal planes is the actual fault plane.

Analyses of the CVA results of samples E1 – E4, E7 and E8 shows that compressional wave velocity varies sinusoidally around the circumference of our rock samples as shown in Figure 4.18. The sinusoidal models are of the form,

$$V_p(\theta) = A + B \sin(C\theta + D) \quad (4.10)$$

where constants $A \approx$ average value of V_p ; $B \approx$ half of the range of V_p ; C controls the period of the sinusoid; and D is the phase angle of the sinusoid. The values of the constants, $A - D$, as well as their correlation coefficients with respect to the actual V_p data are shown in Table 4.4. Figure 4.17 shows that peak values of V_p (with the angle increasing in an anticlockwise direction) occur at 100° and 270° for sample E1; 30° , 150° and 270° for sample E2; 80° and 260° for sample E3; 80° and 280° for sample E4; 140° and 150° for sample E7; and 230° for sample E8. In a clockwise convention (which is adopted in the analyses of focal mechanisms in this work), this corresponds to 80° and 90° for sample E1; 150° , 30° and 90° for sample E2; 100° for sample E3; 100° and 80° for sample E4; 40° and 50° for sample E7; and 130° for sample E8. It is also seen from Table 4.4 that between 54 % and 100 % of the variance of V_p data could be predicted by the sinusoidal models.

Figure 4.17. Sinusoidal models for V_p data for samples E1-E8.

Table 4.4. Model Parameters and Correlation Coefficients for Sinusoidal Models for V_p Data for Samples E1-E8.

Sample	A	B	C	D	r	Variance (%)
E1	0.00	0.00	0.00	0.00	0.00	54
E2	0.00	0.00	0.00	0.00	0.00	100
E3	0.00	0.00	0.00	0.00	0.00	100
E4	0.00	0.00	0.00	0.00	0.00	100
E7	0.00	0.00	0.00	0.00	0.00	100
E8	0.00	0.00	0.00	0.00	0.00	100

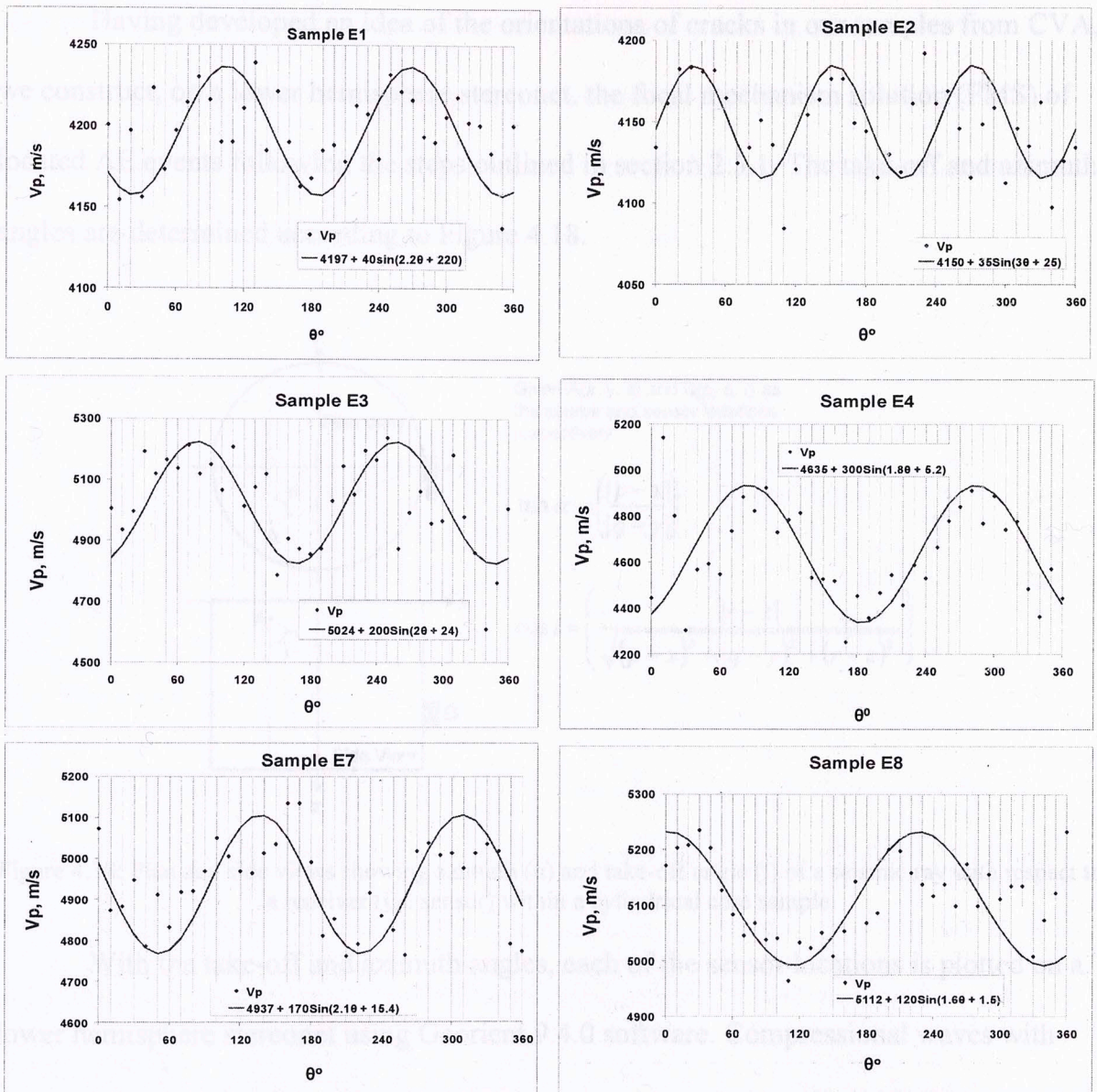


Figure 4.17: Sinusoidal variations of compressional waves around the circumferences of samples E1 – E4, E7 and E8.

Table 4.4: Model Parameters and correlation coefficient, R^2 , of the CVA Results for samples E1 – E4, E7 and E8

Sample ID	A	B	C	D	R^2
E1	4197	40	2.2	220.0	0.54
E2	4150	35	3.0	25.0	1.00
E3	5024	200	2.0	24.0	0.64
E4	4635	300	1.8	5.2	0.62
E7	4937	170	2.1	15.4	0.70
E8	5112	120	1.6	1.5	0.64

Having developed an idea of the orientations of cracks in our samples from CVA, we construct, on a lower hemisphere stereonet, the focal mechanism solution (FMS) of located AE events following the steps outlined in section 2.5.1. The take-off and azimuth angles are determined according to Figure 4.18.

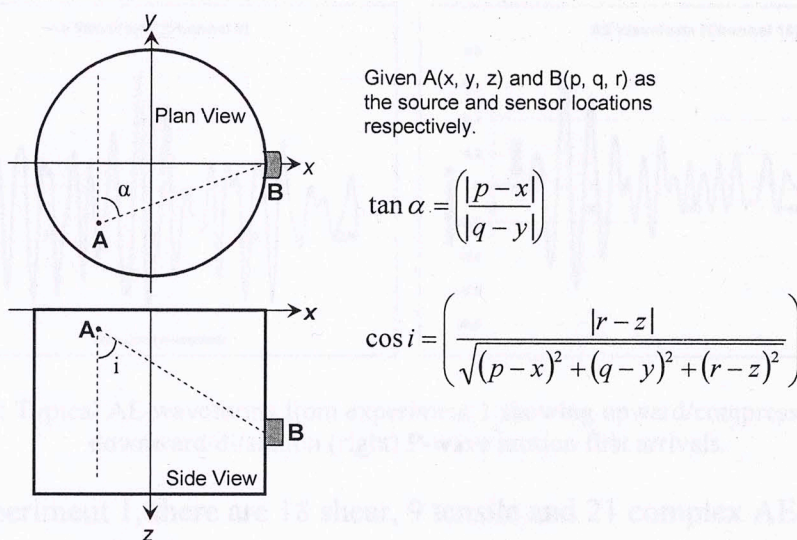


Figure 4.18: Plan and side views showing azimuth (α) and take-off angle (i) of a seismic ray with respect to a receiver (i.e. sensor) within a cylindrical core sample.

With the take-off and azimuth angles, each of the sensor locations is plotted on a lower hemisphere stereonet using Georient 9.4.0 software. Compressional waves with upward (compressional) first motion arrivals are indicated with a filled circle while those with negative (dilatational) first motions are indicated with open circles. Examples of AE signals with upward and downward P-wave motion first arrivals are shown in Figure 4.19. Single-event FMS for all the AE events associated with the fracturing of samples E1 - E4, E7 and E8 as well as composite focal mechanisms (Sondergeld and Estey, 1982) for closely located AE events are plotted. Classification of the focal plots is based on guideline given by Fall et al. (1992): A tensile events occurs if all the P-wave motion first arrivals are upwards and compressive if they are all downwards; if P-wave first motion

arrivals have mixed polarities (upwards and downwards) and can be separated into 4 quadrants by 2 perpendicular nodal planes (fault and auxiliary planes), then the AE event is said to be shear event from a double-coupled source. If it cannot be separated into 4 quadrants, then, it is complex or non-double-couple shear.

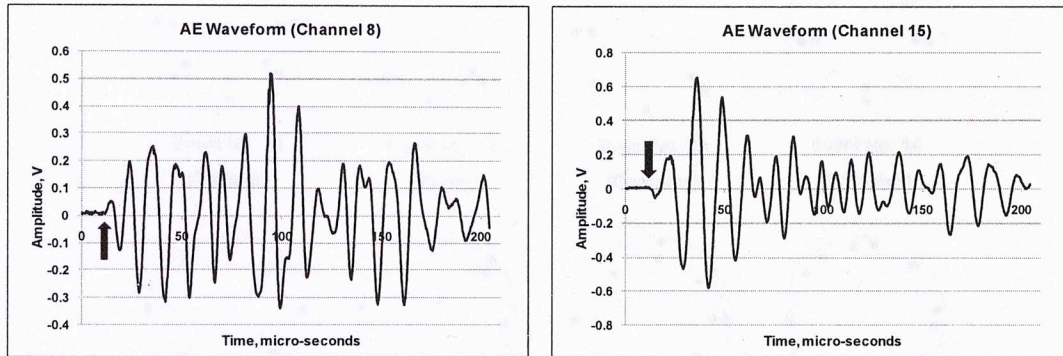


Figure 4.19: Typical AE waveforms from experiment 1 showing upward/compression (left) and downward/dilatation (right) P-wave motion first arrivals.

For experiment 1, there are 18 shear, 9 tensile and 21 complex AE events as shown in Figure 4.20. The 18 shear events are characterized by normal (61%), thrust (17%), pure dip-slip (17%) and strike-slip (5%) faulting. This suggests that extensional deformation of the rock was the dominant mechanism responsible for the shear failures (Kayal, 2008).

Composite focal mechanisms (Sondergeld and Estey, 1982) are also plotted as shown in Figure 4.21 for 3 clusters (cluster E1_A, cluster E1_B and cluster E1_C within an area of less than 10-mm diameter) of AE events suggesting similarities in microfracturing process. A summary of the fault parameters associated with the hydraulic fracturing of sample E1 is depicted in Table 4.5. The strikes of the shear events are generally subparallel to the orientation (NE-SW) of the AE location.

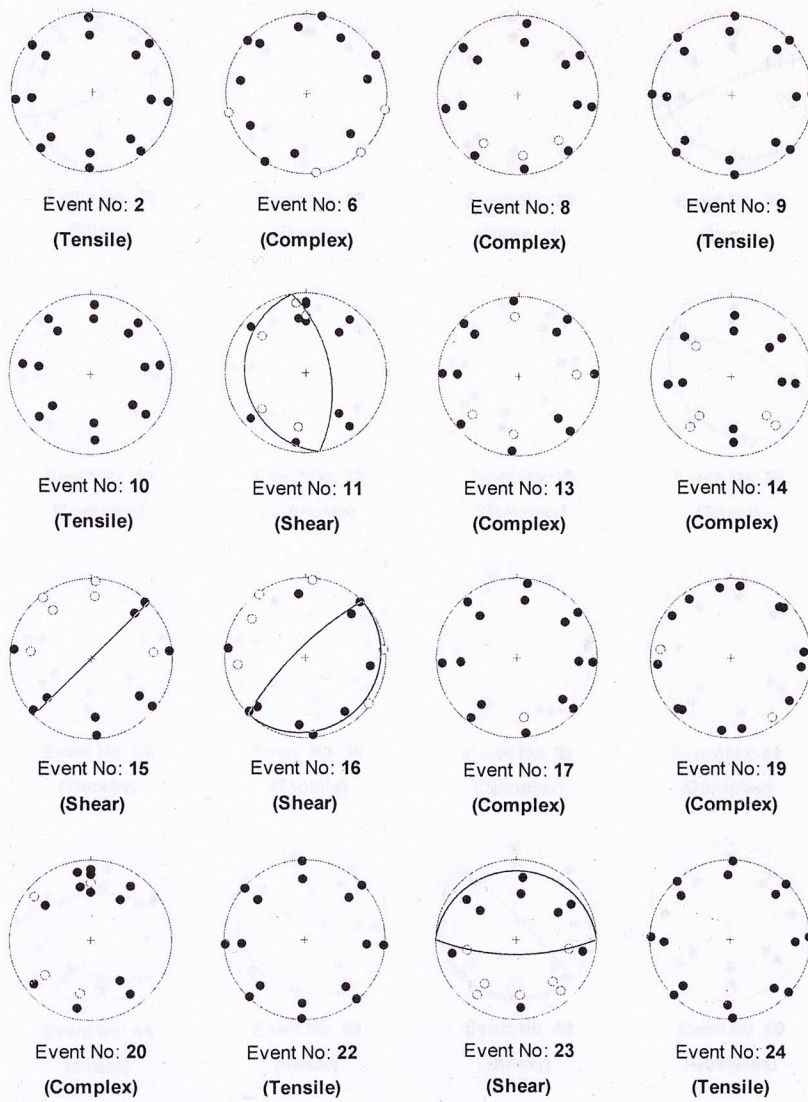


Figure 4.20: Focal mechanism solutions of AE events (48) from sample E1 (fractured with mineral oil) showing tensile (9), shear (18) and complex (21) events. Filled circles show compressional while open circles show dilatation first motion p-wave arrivals.

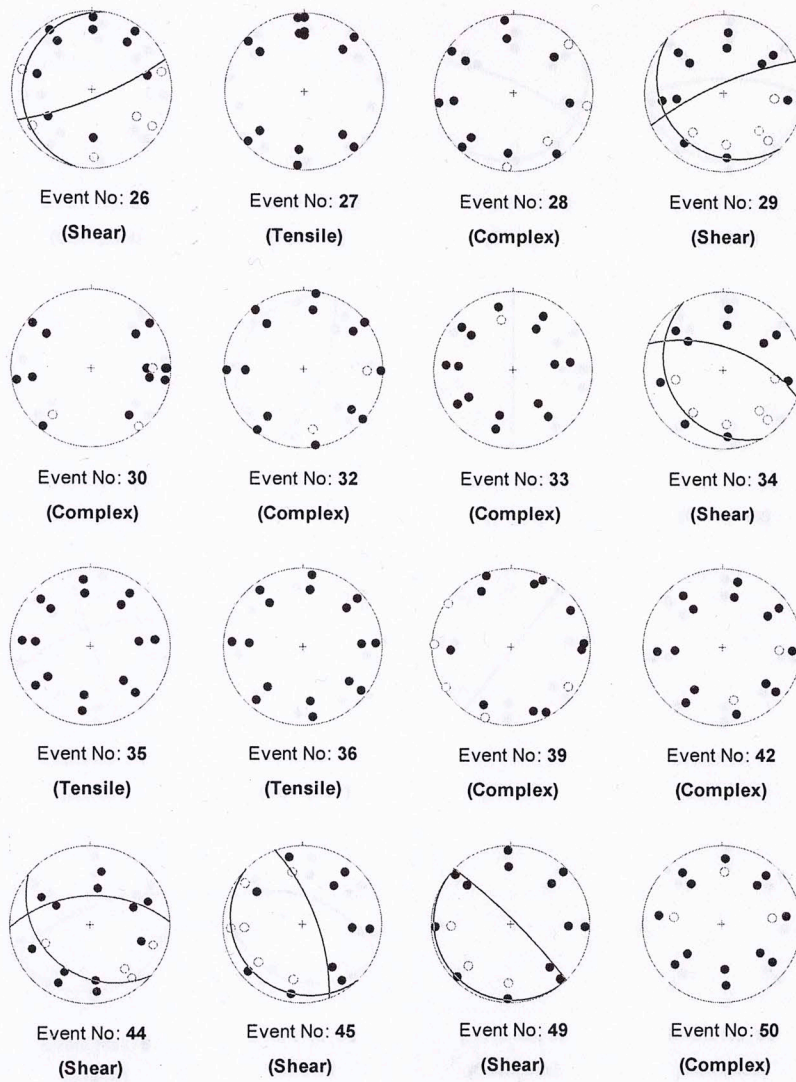


Figure 4.20: continued

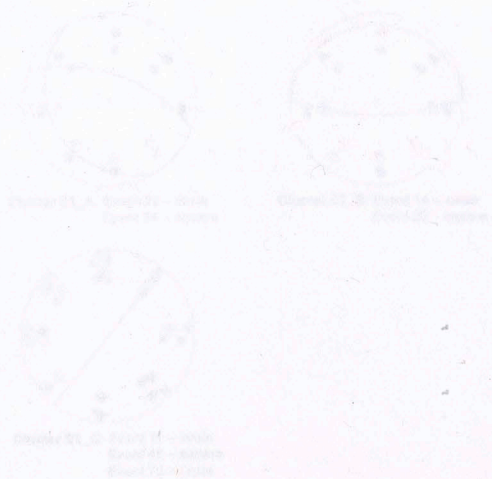


Figure 4.21: Composite focal mechanism solutions of AF events from sample E1 (fractured with mineral oil) showing normal, thrust and dip-slip faulting for clusters E1_A, E1_B and E1_C, respectively.

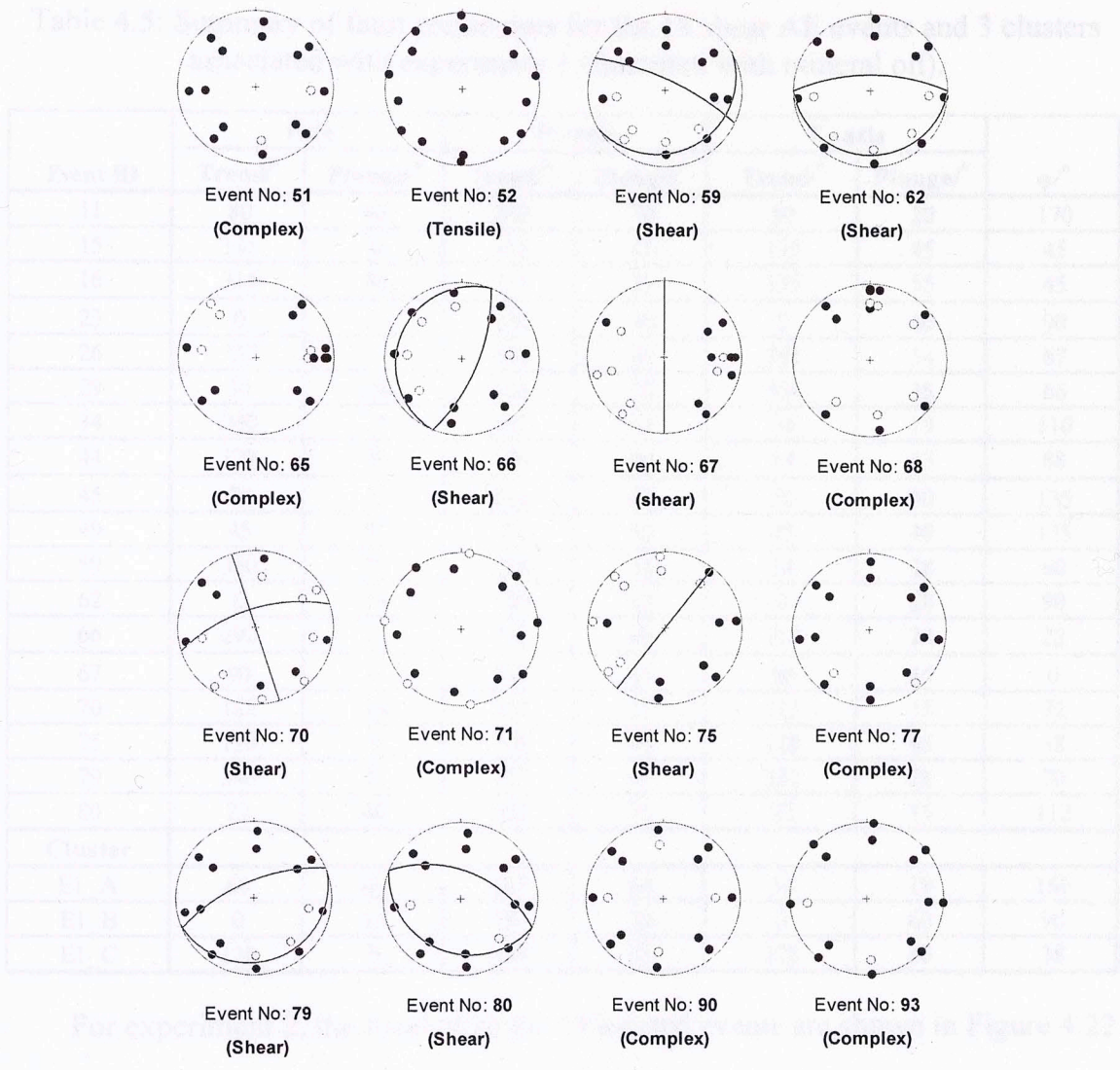


Figure 4.20: continued

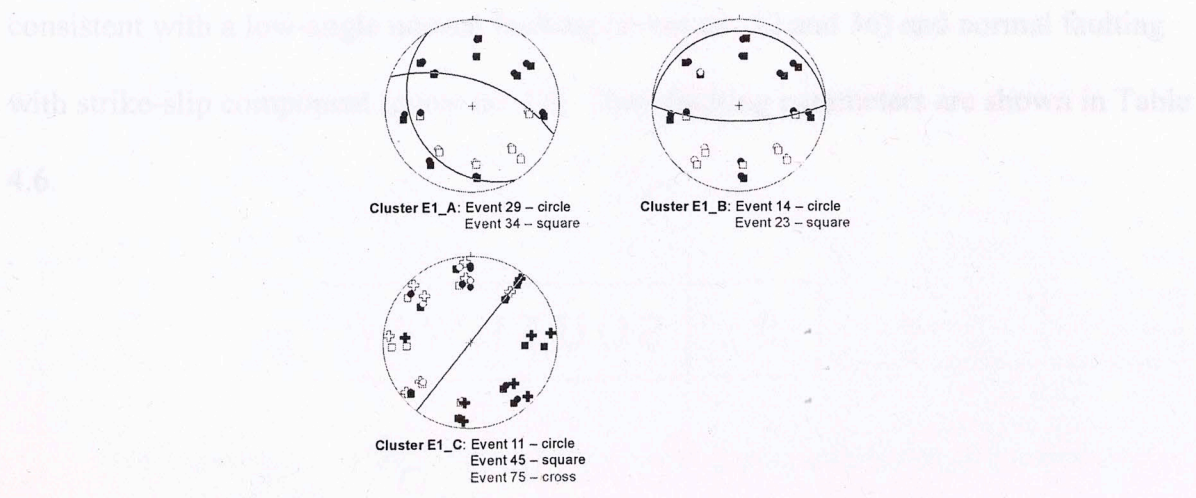


Figure 4.21: Composite focal mechanism solutions of AE events from sample E1 (fractured with mineral oil) showing normal, thrust and dip-slip faulting for clusters E1_A, E1_B and E1_C, respectively.

Table 4.5: Summary of fault parameters for the 18 shear AE events and 3 clusters associated with experiment 1 (fractured with mineral oil).

Event ID	Pole		P - axis		T - axis		$\phi/^\circ$
	Trend/ $^\circ$	Plunge/ $^\circ$	Trend/ $^\circ$	Plunge/ $^\circ$	Trend/ $^\circ$	Plunge/ $^\circ$	
11	80	65	260	70	80	20	170
15	135	0	315	45	135	45	45
16	315	80	315	35	135	55	45
23	0	15	180	30	0	60	90
26	337	9	142	44	355	54	67
29	10	156	126	55	354	36	66
34	200	24	167	64	34	19	110
44	178	30	126	66	14	13	88
45	75	45	214	60	50	30	135
49	45	85	225	50	45	40	135
59	330	70	228	58	14	28	60
62	0	73	180	62	0	28	90
66	292	21	292	66	112	24	22
67	90	0	270	45	90	45	0
70	162	18	212	15	112	15	72
75	128	0	308	45	128	45	38
79	340	72	157	63	337	28	70
80	22	60	202	75	22	15	112
Cluster							
EI_A	60	60	167	64	34	19	150
EI_B	0	15	180	30	0	60	90
EI_C	128	0	308	45	128	45	38

For experiment 2, the focal plots for 13 located events are shown in Figure 4.22.

FMS can be grouped into 3 shear, 2 tensile and 8 complex events. The shear events are consistent with a low-angle normal faulting (event no. 12 and 36) and normal faulting with strike-slip component (event no. 15). Their faulting parameters are shown in Table 4.6.

Event ID	Pole		P - axis		T - axis		$\phi/^\circ$
	Trend/ $^\circ$	Plunge/ $^\circ$	Trend/ $^\circ$	Plunge/ $^\circ$	Trend/ $^\circ$	Plunge/ $^\circ$	
12	0	2	180	30	0	60	90
15	135	0	315	45	135	45	45
36	20	10	170	60	20	10	170

For experiment 3 (fractured with water), the focal plots for its 10 located AE events are shown in Figure 4.23. It consists of 3 shear and 7 tensile events. The shear

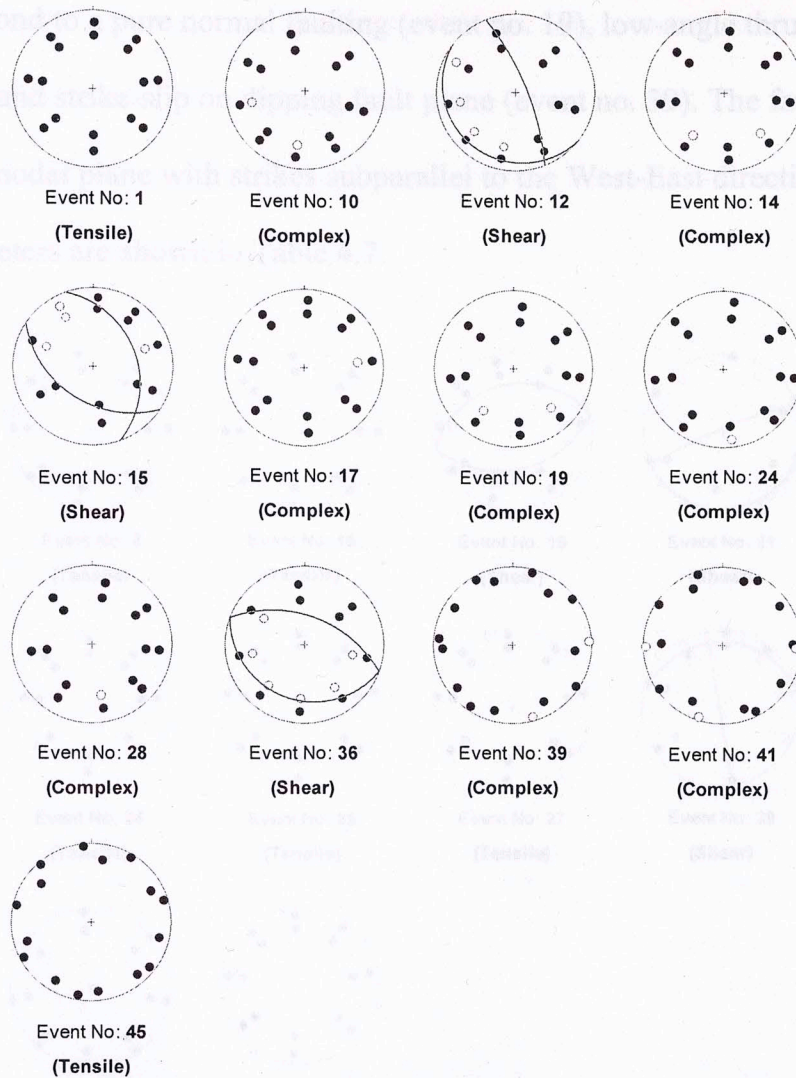


Figure 4.22: Focal mechanism solutions of AE events (13) from sample E2 (fractured with water) showing tensile (2), shear (3) and complex (8) events. Filled circles show compressional while open circles show dilatation first motion p-wave arrivals.

Table 4.6: Summary of fault parameters for 3 shear AE events associated with experiment 2 (fractured with oil)

Event ID	Pole		P - axis		T - axis		$\phi/^\circ$
	Trend/ $^\circ$	Plunge/ $^\circ$	Trend/ $^\circ$	Plunge/ $^\circ$	Trend/ $^\circ$	Plunge/ $^\circ$	
12	37	76	257	59	63	34	127
15	33	37	121	72	234	6	123
36	20	60	200	75	20	15	110

For experiment 3 (fractured with water), the focal plots for its 10 located AE events are shown in Figure 4.23. It consists of 3 shear and 7 tensile events. The shear

events correspond to a pure normal faulting (event no. 19), low-angle thrust faulting (event no. 21) and strike-slip on dipping fault plane (event no. 39). The fault plane could be seen as the nodal plane with strikes subparallel to the West-East direction. Their faulting parameters are shown in Table 4.7.

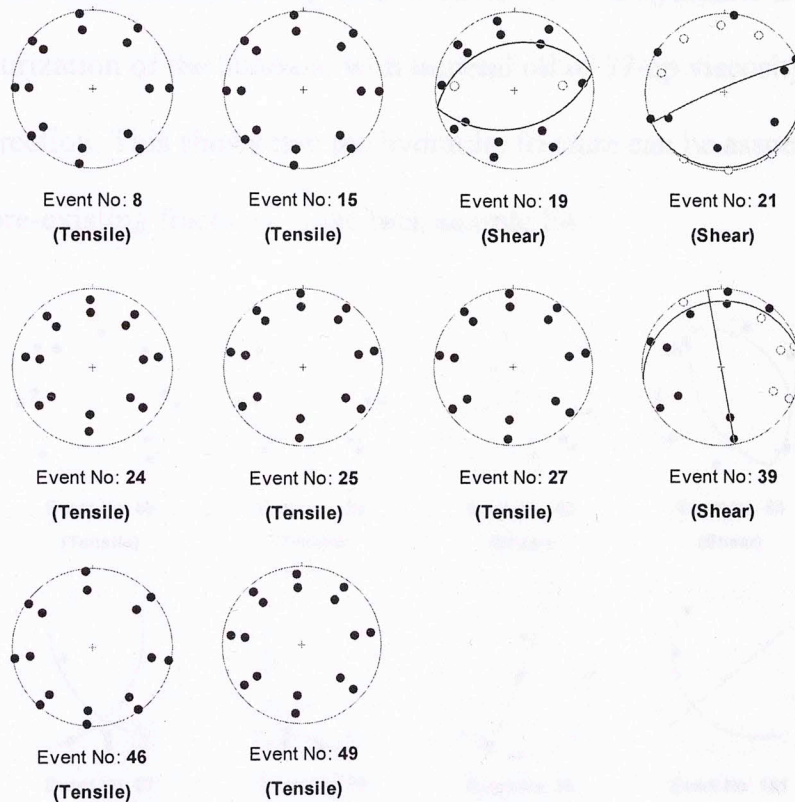


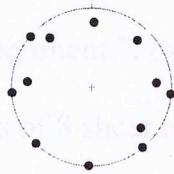
Figure 4.23: Focal mechanism solutions of AE events (10) from experiment 3 (fractured with water) showing tensile (7) and shear (3) events. Filled circles show compressional while open circles show dilatation first motion p-wave arrivals.

Table 4.7: Summary of fault parameters for 3 shear AE events associated with experiment 3 (fractured with water)

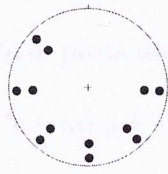
Event ID	Pole		P - axis		T - axis		$\phi/^\circ$
	Trend/ $^\circ$	Plunge/ $^\circ$	Trend/ $^\circ$	Plunge/ $^\circ$	Trend/ $^\circ$	Plunge/ $^\circ$	
19	347	40	347	85	167	5	77
21	337	85	337	40	157	50	67
39	170	73	92	45	250	45	80

For experiment 4, the focal plots for its 14 located AE events are shown in Figure 4.24. It consists of 9 shear, 2 tensile and 3 complex events. The shear events have fault

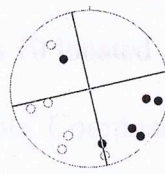
planes with strike angles ranging from 85° to 167° except the pure dip-slip events (no. 76 and 102). The fault planes were chosen as the nodal plane which strike angles are more closely aligned with the strike angles of the pre-existing fractures in sample E4 which have strike angles ranging from 80° to 130° as seen in the CVA result. The fault parameters of the shear events are depicted in Table 4.8. The hydraulic fracture created from the pressurization of the borehole with mineral oil of 37-cp viscosity is aligned in the NW-SE direction. This shows that the hydraulic fracture can be associated with a reopening of pre-existing fractures in the rock sample E4.



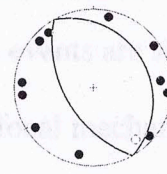
Event No: 58
(Tensile)



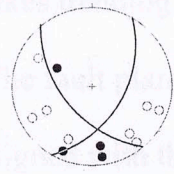
Event No: 60
(Tensile)



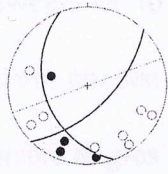
Event No: 63
(Shear)



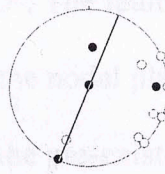
Event No: 65
(Shear)



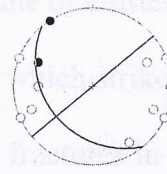
Event No: 67
(Shear)



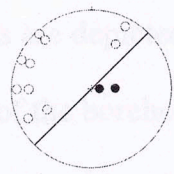
Event No: 74
(Shear)



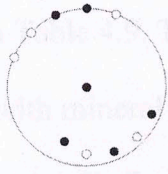
Event No: 76
(Shear)



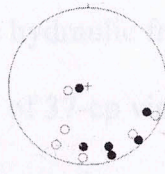
Event No: 101
(Shear)



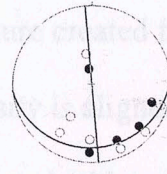
Event No: 102
(Shear)



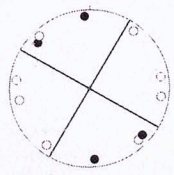
Event No: 104
(Complex)



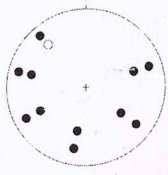
Event No: 107
(Complex)



Event No: 108
(Shear)



Event No: 109
(Shear)



Event No: 111
(Complex)

Figure 4.24: Focal mechanism solutions of AE events (14) from experiment 4 (fractured with mineral oil) showing tensile (2), shear (9) and complex (3) events. Filled circles show compressional while open circles show dilatation first motion p-wave arrivals.

Table 4.8: Summary of fault parameters for 9 shear AE events associated with experiment 4 (fractured with mineral oil)

Event ID	Pole		P - axis		T - axis		$\phi/^\circ$
	Trend/ $^\circ$	Plunge/ $^\circ$	Trend/ $^\circ$	Plunge/ $^\circ$	Trend/ $^\circ$	Plunge/ $^\circ$	
63	167	0	302	0	122	0	77
65	60	30	60	75	240	15	150
67	50	30	80	3	356	46	140
74	70	45	108	14	3	51	160
76	292	0	112	45	292	45	22
101	50	50	103	37	353	35	140
102	315	0	315	45	135	45	45
108	355	70	285	45	66	43	85
109	30	0	75	0	165	0	120

For experiment 7, the focal plots for its 10 located AE events are shown in Figure 4.25. It consists of 8 shear and 2 complex events. Composite focal mechanism of events 10 and 13, separated by 8 mm is plotted in Figure 4.25. The shear events have fault planes with strikes trending between 35° to 135° . The fault plane of cluster E7_1 has a trend of 70° . The fault planes were chosen as the nodal plane which strike angles are more closely aligned with the strike angles of the pre-existing fractures in sample E7 which have strike angle of about 35° as seen in the CVA result. The fault parameters of the shear events are depicted in Table 4.9. The hydraulic fracture created from the pressurization of the borehole with mineral oil of 37-cp viscosity is aligned in the SW-NE direction. This shows that the hydraulic fracture can be associated with a reopening of pre-existing fractures just like in sample E4.

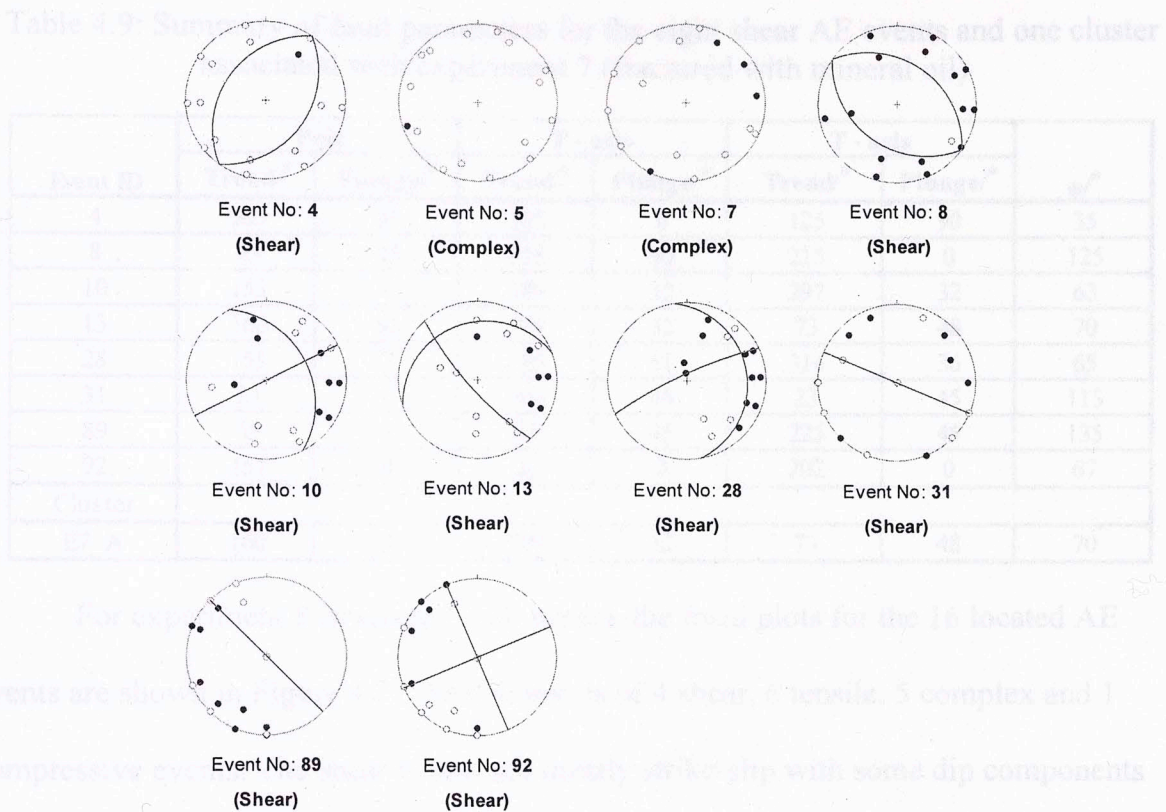
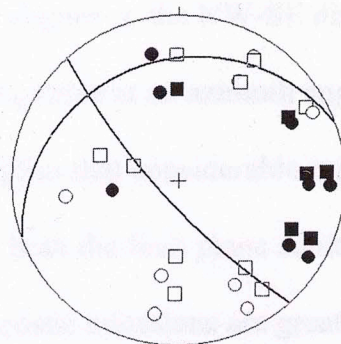


Figure 4.25: Focal mechanism solutions of AE events (10) from sample E7 (fractured with mineral oil) showing shear (8) and complex (2) events. Filled circles show compressional while open circles show dilatation first motion p-wave arrivals.



Cluster E7_1: Event 10 – circle
Event 13 – square

Figure 4.26: Composite focal mechanism solutions of two AE events (no. 10 and 13) from experiment 7 (fractured with mineral oil), separated by a distance of 8 mm, showing left-lateral strike-slip with thrust faulting component.

Table 4.9: Summary of fault parameters for the eight shear AE events and one cluster associated with experiment 7 (fractured with mineral oil)

Event ID	Pole		P - axis		T - axis		$\phi/^\circ$
	Trend/ $^\circ$	Plunge/ $^\circ$	Trend/ $^\circ$	Plunge/ $^\circ$	Trend/ $^\circ$	Plunge/ $^\circ$	
4	305	45	125	0	125	90	35
8	45	45	215	90	215	0	125
10	153	0	189	32	297	32	63
13	160	62	209	32	73	48	70
28	155	7	186	51	314	36	65
31	23	0	203	45	23	45	113
89	45	0	45	45	225	45	135
92	157	0	22	0	202	0	67
Cluster							
E7_A	160	62	209	32	73	48	70

For experiment 8 (fractured with water), the focal plots for the 16 located AE events are shown in Figure 4.27. FMS consists of 4 shear, 6 tensile, 5 complex and 1 compressive events. The shear events are mostly strike-slip with some dip components and have fault planes with strike angles ranging from 50° to 80° . The fault planes are chosen as those that are subparallel to the event locations of Figure 4.14 which reveals the hydraulic fractures as being aligned in the NW-SE direction. A close examination of the CVA results shows a peak V_p value at an azimuth angle of 230° (i.e. 130° in clockwise convention). This implies that considerable number of cracks is trending 130° . This result is in agreement with both the fault plane solutions and event locations and also bolsters the fact that the acoustic emissions are greatly influenced by pre-existing fractures in sample E8. The fault parameters of the shear events are depicted in Table 4.10.

Event ID	Trend/ $^\circ$	Plunge/ $^\circ$	Trend/ $^\circ$	Plunge/ $^\circ$	Trend/ $^\circ$	Plunge/ $^\circ$	$\phi/^\circ$
10	153	0	189	32	297	32	63
13	160	62	209	32	73	48	70
28	155	7	186	51	314	36	65
31	23	0	203	45	23	45	113
89	45	0	45	45	225	45	135
92	157	0	22	0	202	0	67

In summary, the focal plots reveal four classes of fracturing mechanisms at play: tensile, shear, compressive and complex. Given the burst nature of AE recorded, located and plotted,

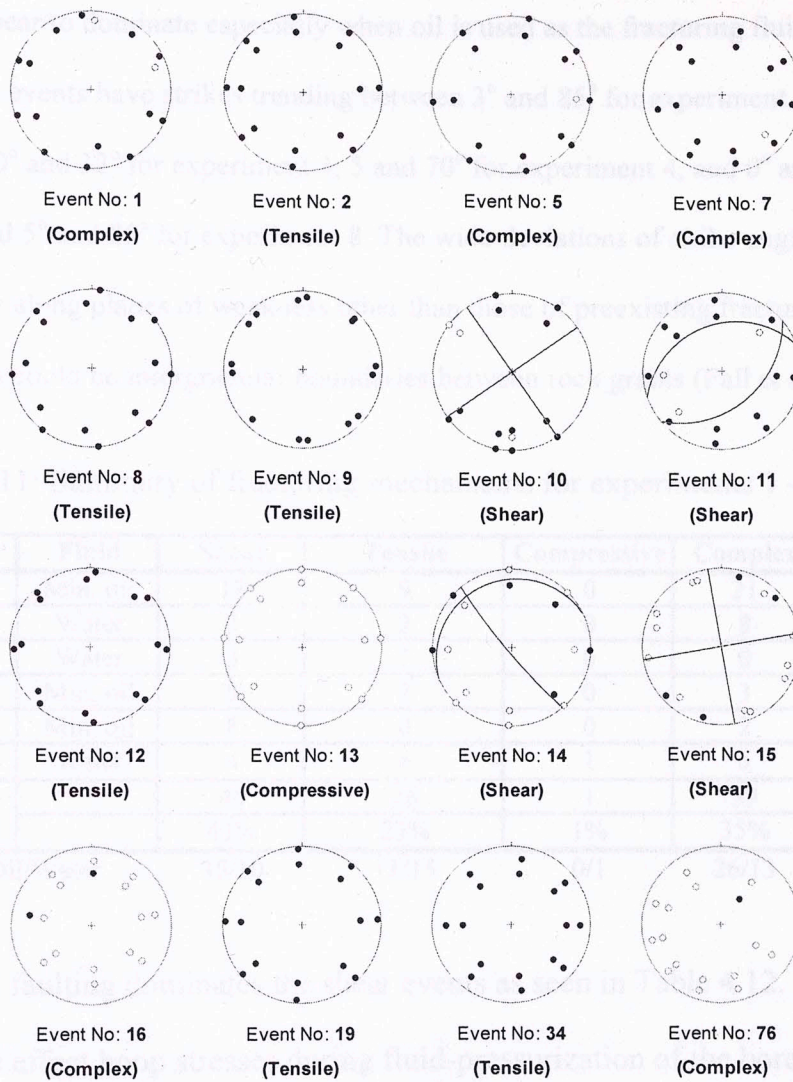


Figure 4.27: Focal mechanism solutions of AE events (16) from sample E8 (fractured with water) showing tensile (6), shear (4) and complex (5) and compressive events. Filled circles show compressional while open circles show dilatation first motion p-wave arrivals.

Table 4.10: Summary of fault parameters for the four shear AE events associated with experiment 8 (fractured with water)

Event ID	Pole		P - axis		T - axis		$\phi/^\circ$
	Trend/ $^\circ$	Plunge/ $^\circ$	Trend/ $^\circ$	Plunge/ $^\circ$	Trend/ $^\circ$	Plunge/ $^\circ$	
10	55	0	10	0	100	0	145
11	160	50	35	79	150	10	50
14	50	5	215	40	67	46	140
15	80	0	125	0	35	0	170

In summary, the focal plots reveal four classes of fracturing mechanisms at play: tensile, shear, compressive and complex. Giving the burst nature of AE recorded, located and plotted,

shear events appear to dominate especially when oil is used as the fracturing fluid (see Table 4.11). The shear events have strikes trending between 3° and 85° for experiment 1, 23° and 40° for experiment 2, 20° and 33° for experiment 3, 5 and 70° for experiment 4, and 0° and 100° for experiment 7 and 5° and 85° for experiment 8. The wide deviations of strike angles show that shear slip occurs along planes of weakness other than those of preexisting fractures. Such weakness planes could be intergranular boundaries between rock grains (Fall et al., 1992).

Table 4.11: Summary of fracturing mechanisms for experiments 1 – 4, 7 & 8

Sample ID	Fluid	Shear	Tensile	Compressive	Complex	Total
E1	Min. oil	18	9	0	21	48
E2	Water	3	2	0	8	13
E3	Water	3	7	0	0	10
E4	Min. oil	9	2	0	3	14
E7	Min. oil	8	0	0	2	10
E8	Water	4	6	1	5	16
Combined		45	26	1	39	111
	Ratio: Oil/Water	35/10	11/15	0/1	26/13	72/39

Normal faulting dominates the shear events as seen in Table 4.12. This is a clear evidence of the effect hoop stresses during fluid-pressurization of the borehole. The hoop stresses are tensile and act horizontally and tangential to the boreholes.

Table 4.12: Summary of faulting mechanisms of shear events

Sample ID	Fluid	Normal	Thrust	Dip-slip	Strike-slip	Total
E1	Min. oil	11	3	3	1	18
E2	Water	3	0	0	0	3
E3	Water	1	1	0	1	3
E4	Min. oil	1	2	2	4	9
E7	Min. oil	2	2	2	2	8
E8	Water	1	1	0	2	4
Combined		19	9	7	10	45
	Ratio: Oil/Water	14/5	7/2	7/0	7/3	35/10

When all the located AE events are plotted together as shown in Figure 4.29, the focal plots do not fit a simple shear, tensile, or compressive source model. This underscores the fact that the acoustic emissions are due to complicated combinations of different fracturing mechanisms.

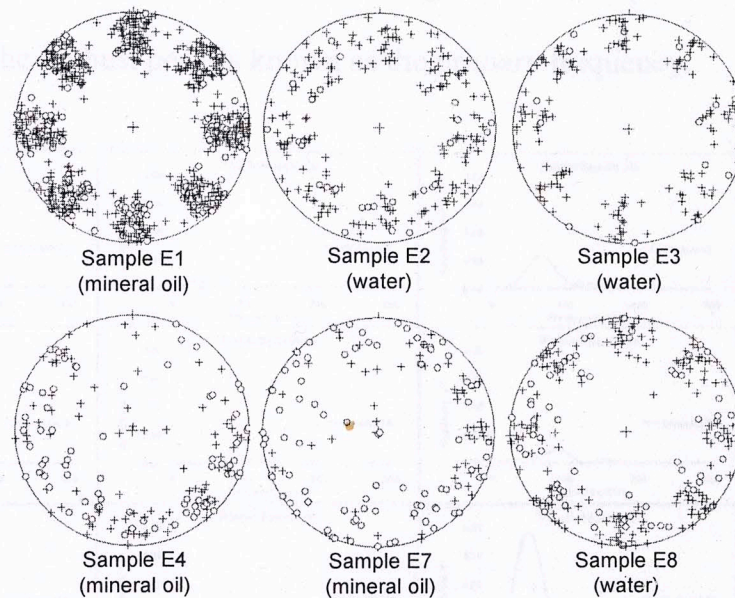


Figure 4.28: Composite focal mechanism solutions of all the AE events associated with the hydraulic fracturing of samples E1 – E4, E7 and E8. The ‘plus’ signs signify compressional while open circles show dilatation first motion P-wave arrivals. None of the plots fits a simple double couple source.

4.2.4 Spectral Analyses of AE Signals

A growing aspect of AE work is the spectra analysis of the AE signals which is aimed at determining the frequency contents. Ohnaka and Mogi (1981) suggested that different cracking mechanisms possess different frequency content. Spasova and Ojovan (2007) used the primary frequencies of AE power spectra to characterize AE sources in cementitious wastefoms with encapsulated aluminum as being due to cement matrix hardening (> 2 MHz), cracking (> 100 KHz) and aluminum corrosion (< 40 KHz).

In our study, the power spectra are determined for the P-wave portions of AE events associated with experiments 1 – 4, 7 and 8. They are computed as squares of the amplitudes of the frequency spectra derived from the Fast Fourier Transformation of the time-domain AE signals. Examples of power spectra of an AE event are shown in Figure 4.29. The spectra show a peak or peaks occurring at certain frequencies. The frequency associated with the highest peak is known as the primary frequency.

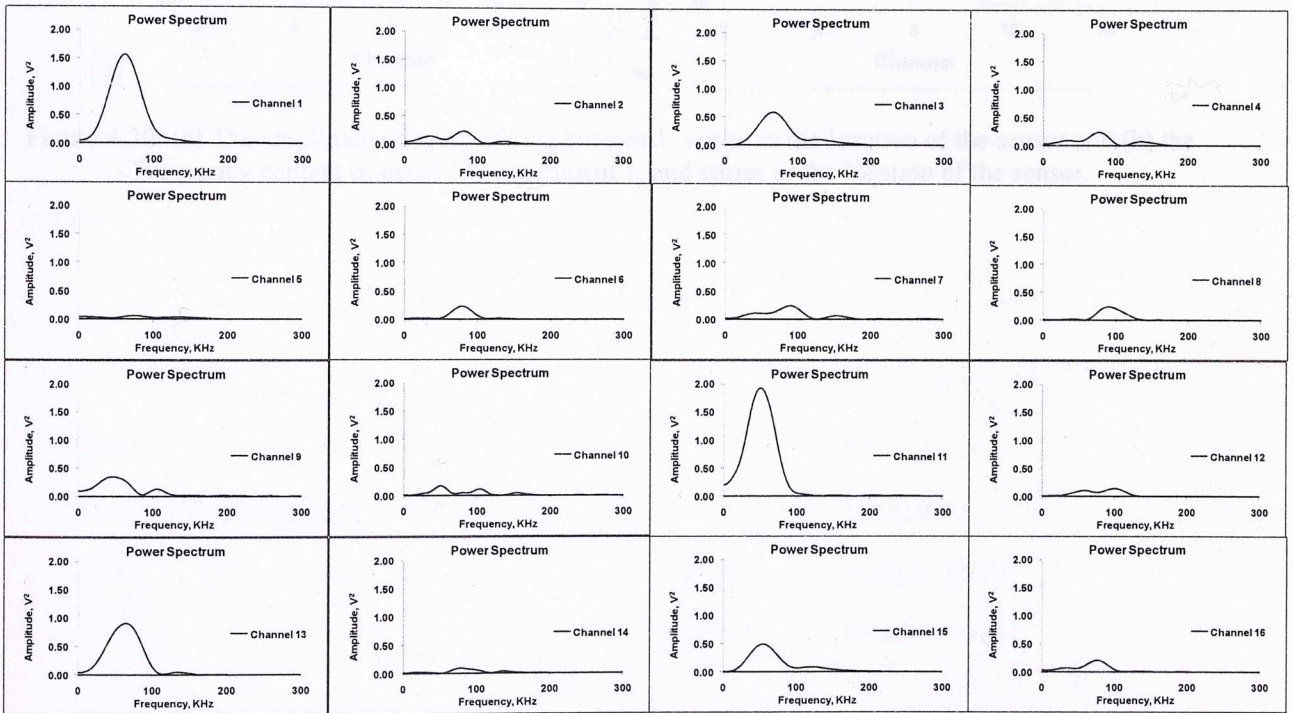


Figure 4.29: Power spectra of early portions of event 8 of experiment 1 on all 16 channels. They show spectra peaks and associated primary frequencies.

A close examination of the power spectra shows a variation of both the highest peak amplitude and the primary frequency with respect to the sensor position. An example is shown in Figure 4.30. This dependence of frequency content on azimuth could be due to the presence of very small and localized regions of intense microfracturing or the radiation pattern of the AE source (Sondergeld and Estey, 1982). In Figure 4.31, we see that microfracturing mechanisms possess overlapping primary

frequencies. A characteristic of the spectra is that the peak amplitude (in decibel) decreases linearly with primary frequency (in KHz) for all the AE signals associated with the hydraulic fracturing experiments. This is shown in Figure 4. 32.

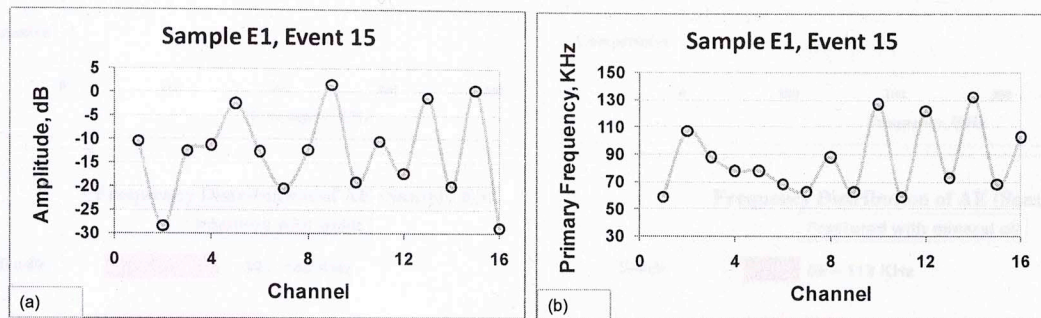


Figure 4.30: (a) The amplitude of event 15, experiment 1, varies as the location of the sensor and (b) the frequency content of event 15, experiment 1, and varies as the location of the sensor.

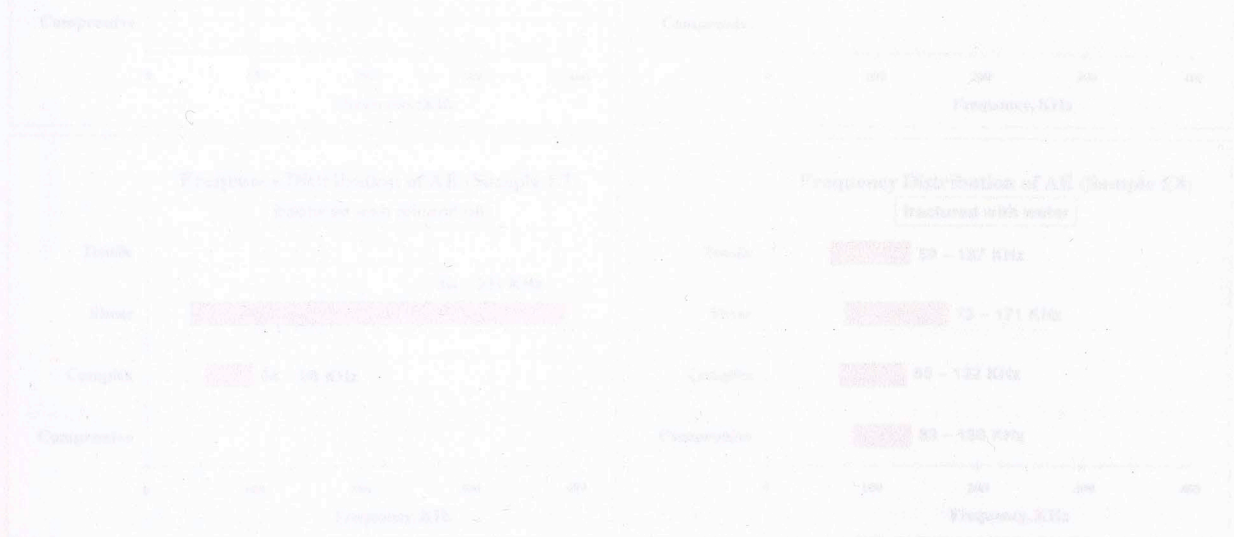


Figure 4.31: Frequency content of power spectra of the P wave portion of AE induced during the hydraulic fracturing of Samples E1, E4, E7 and E8.

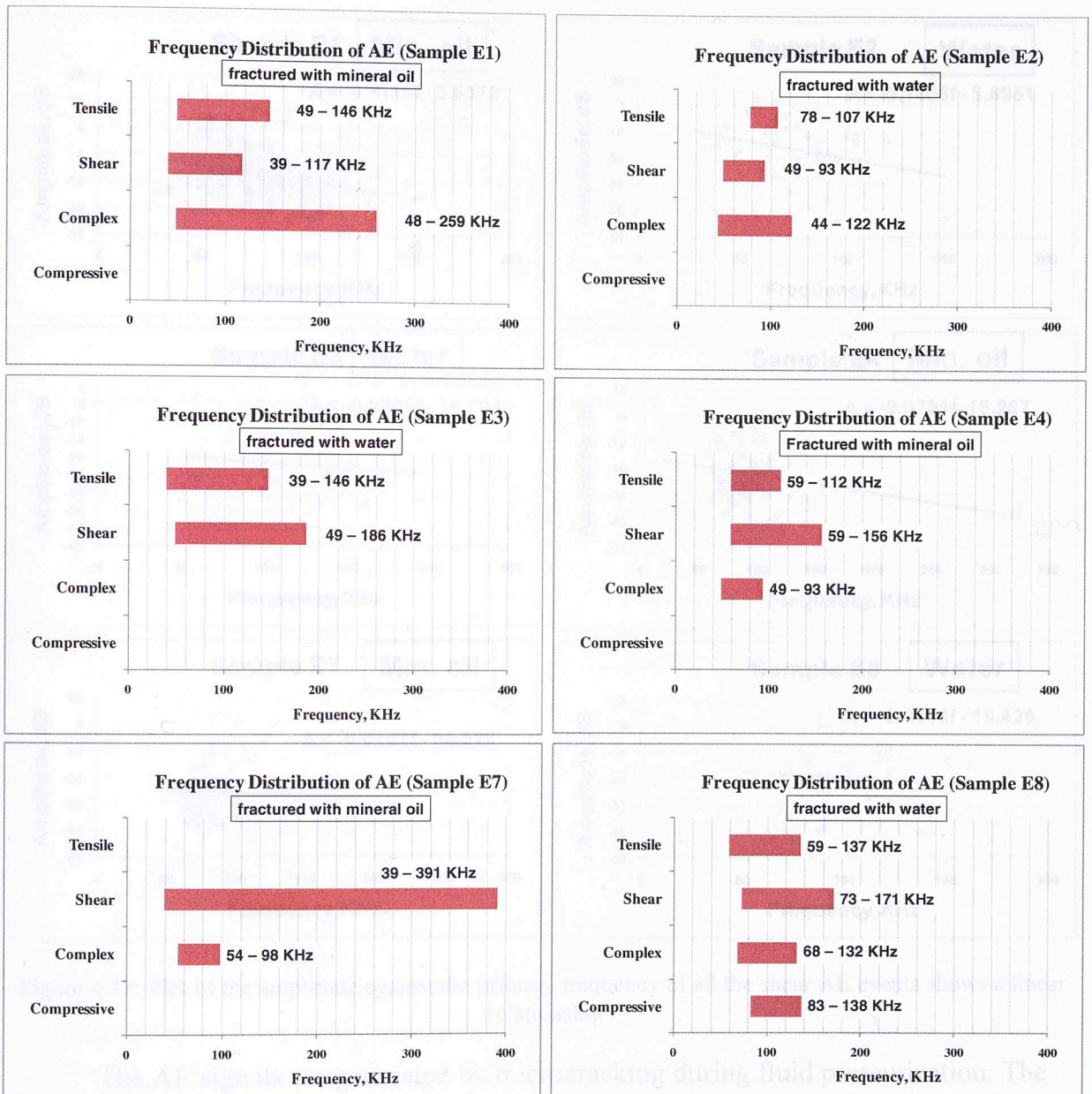


Figure 4.31: Frequency content of power spectra of the P-wave portion of AE induced during the hydraulic fracturing of samples E1-E4, E7 and E8.

associated with the shear events. The displacement amplitudes show exponential dependence on peak power spectra (dB) and are plotted in Figure 4.33.

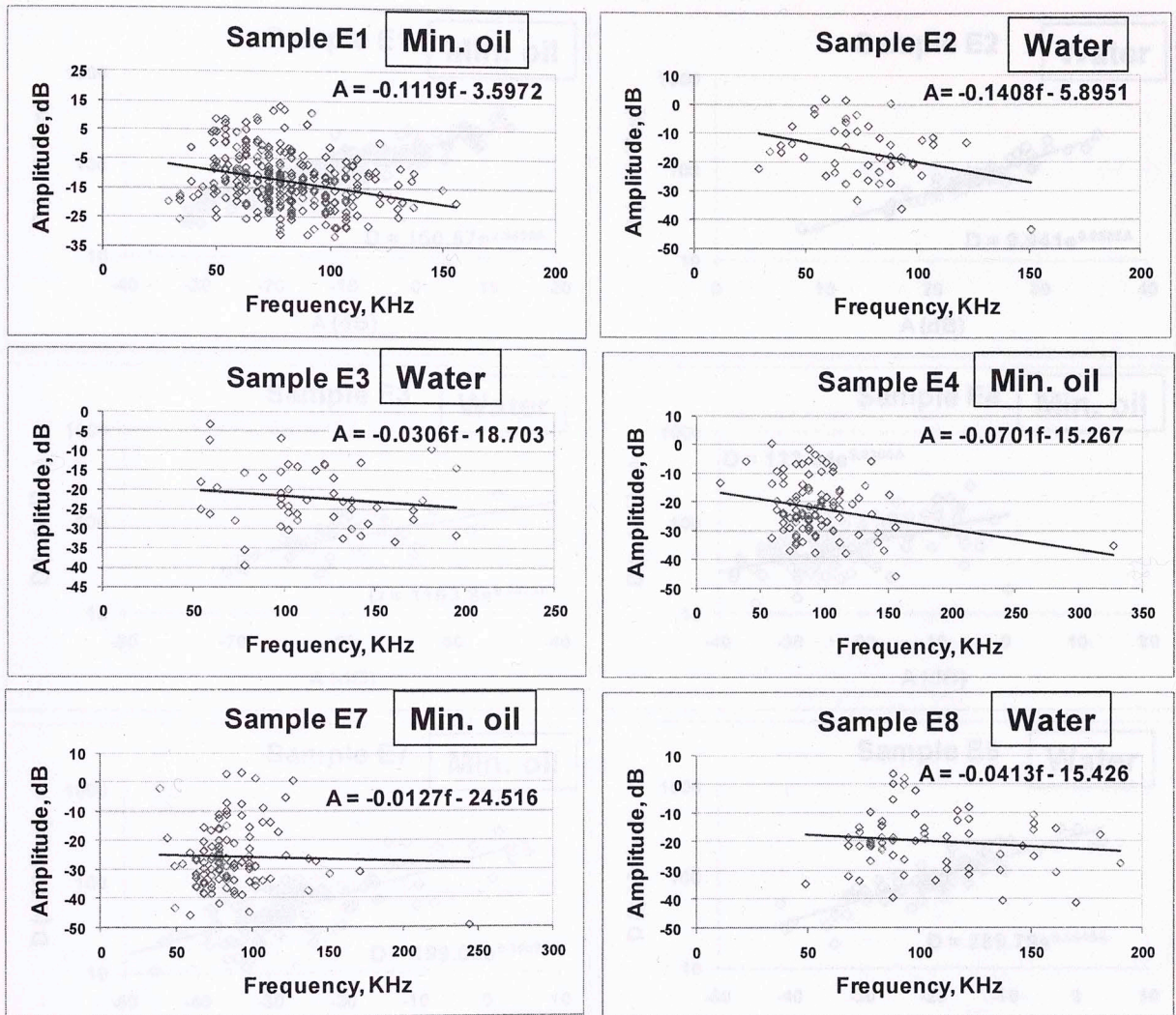


Figure 4.32: Plot of the amplitude against the primary frequency of all the shear AE events shows a linear relationship

The AE signals are generated by microcracking during fluid pressurization. The amplitudes are correlated with the displacements (calculated using equation 4.14) associated with the shear events. The displacement amplitudes show exponential dependence on peak power spectra (dB) and are plotted in Figure 4.33.

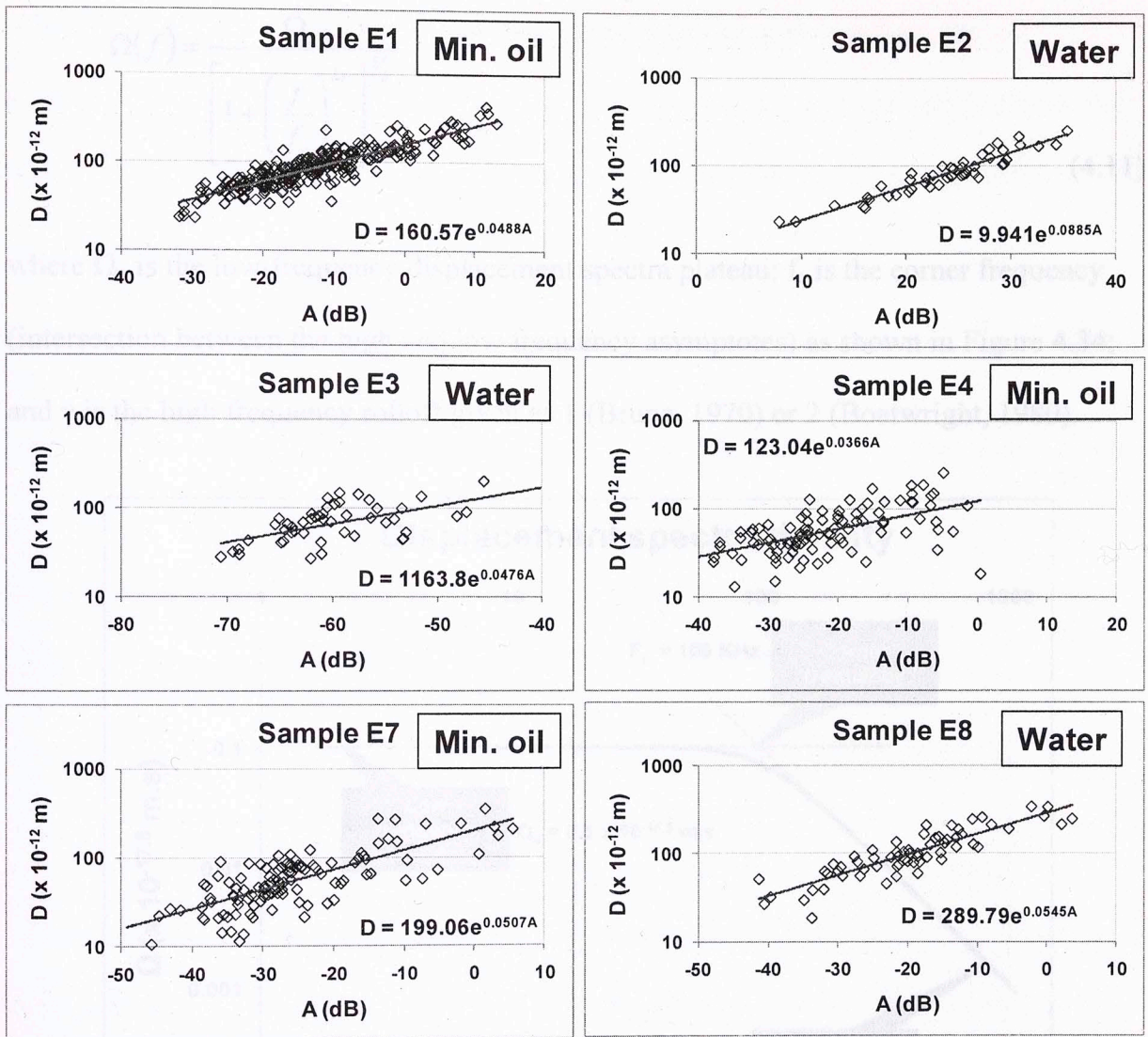


Figure 4.33: Plot of displacement against peak amplitude of all the shear AE events shows an exponential relationship

4.2.5 Source Parameters of Acoustic Emissions

The determination of source parameters (source radius, seismic moment, average displacement, moment magnitude and stress drop) is used in seismology to assess the strength and dimensions of earthquakes. A similar concept has been adopted here to characterize the shear AE events associated with hydraulic fracturing experiments.

Boatwright (1980) gives a relationship between the displacement spectral density and frequency

$$\Omega(f) = \frac{\Omega_o}{\left[1 + \left(\frac{f}{f_c}\right)^{2\gamma}\right]^{1/2}} \quad (4.11)$$

where Ω_o is the low-frequency displacement spectra plateau; f_c is the corner frequency (intersection between the high and low frequency asymptotes) as shown in Figure 4.34; and γ is the high frequency rolloff given as 1 (Brune, 1970) or 2 (Boatwright, 1980).

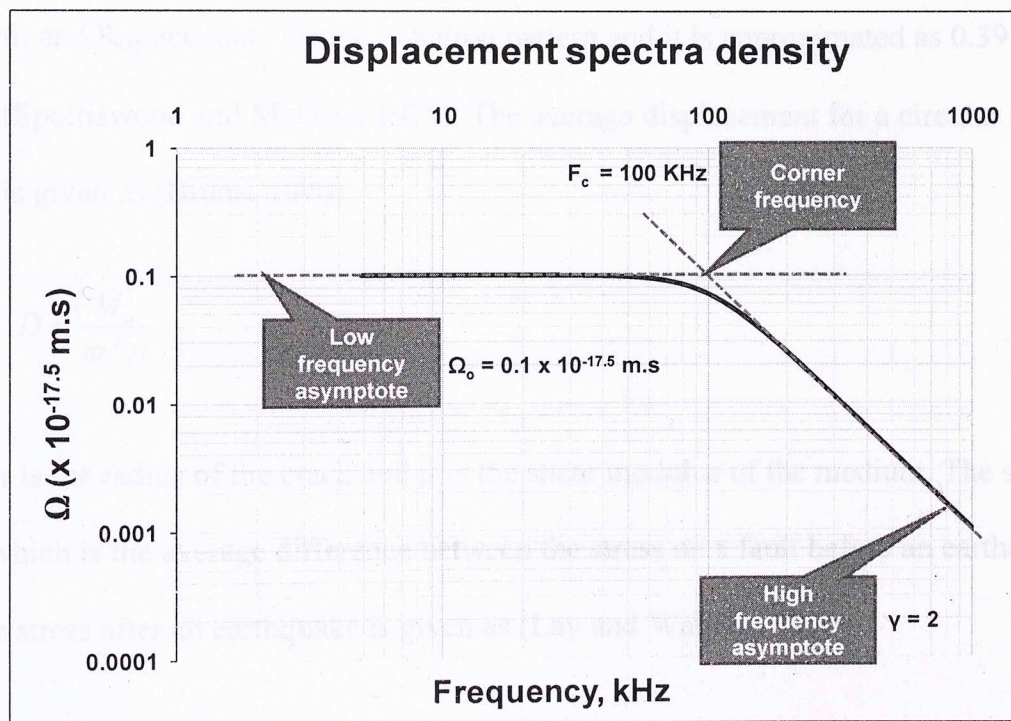


Figure 4.34: Theoretical displacement spectral density showing high and low frequency asymptotes.

Assuming a circular crack, the average source radius is a function of the corner frequency (Brune, 1970). Applying this to P-waves (Hanks and Wyss, 1972) give the following expression relating source radius, r , and the corner frequency, f_c :

$$r = \frac{2.34V_p}{2\pi f_c} \quad (4.12)$$

where V_p is the p-wave velocity. The seismic moment, M_o which defines the microcracking process in terms of the rigidity of the medium, average displacement and area of the fault (Stein and Wysession, 2003) is given as (Aki and Richard, 2002)

$$M_o = \frac{\Omega_o}{R_{o\phi}} 4\pi\rho R V_p^3 \quad (4.13)$$

where R is the distance between the event source and the receiver; ρ is the density of the medium; and $R_{o\phi}$ accounts for the radiation pattern and it is approximated as 0.39 for P-waves (Spottiswood and McGarr, 1975). The average displacement for a circular crack model is given as (Brune, 1970)

$$D = \frac{M_o}{\pi r^2 \mu} \quad (4.14)$$

where r is the radius of the crack and μ is the shear modulus of the medium. The stress drop, which is the average difference between the stress on a fault before an earthquake and the stress after an earthquake is given as (Lay and Wallace, 1995)

$$\Delta\sigma = \frac{7}{16} \frac{M_o}{r^3} \quad (4.15)$$

The size of the micro-earthquakes are given in terms of the moment magnitude as (Stein and Wysession, 2003)

$$M_w = \frac{\log_{10} M_o - 9.1}{1.5} \quad (4.16)$$

where the seismic moment, M_o is given in Nm.

One of the most important considerations in computing source parameters is the physical quantity being recorded by the AE system. From private communication with a representative of Digital Wave, Inc., the AE recording system was calibrated to yield displacement as a function of time. This was verified by computing the spectra densities for all the AE signals associated with the shear events. Figure 4.35 shows the spectral densities of 16 channels in event 15 of experiment 1. The spectra agree well with a typical displacement spectra density plot (see Figure 4.34). The corner frequency and low-frequency displacement spectra plateau are then read off the log-log plot of displacement spectra density versus frequency and used to calculate other source parameters, taking the total signal amplification (70 dB) and sensor displacement sensitivity (100 V/ μm) into account. The plots are matched with theoretical displacement spectral densities from equation (4.9) using optimum values of corner frequencies, low frequency spectral plateau and rolloff.

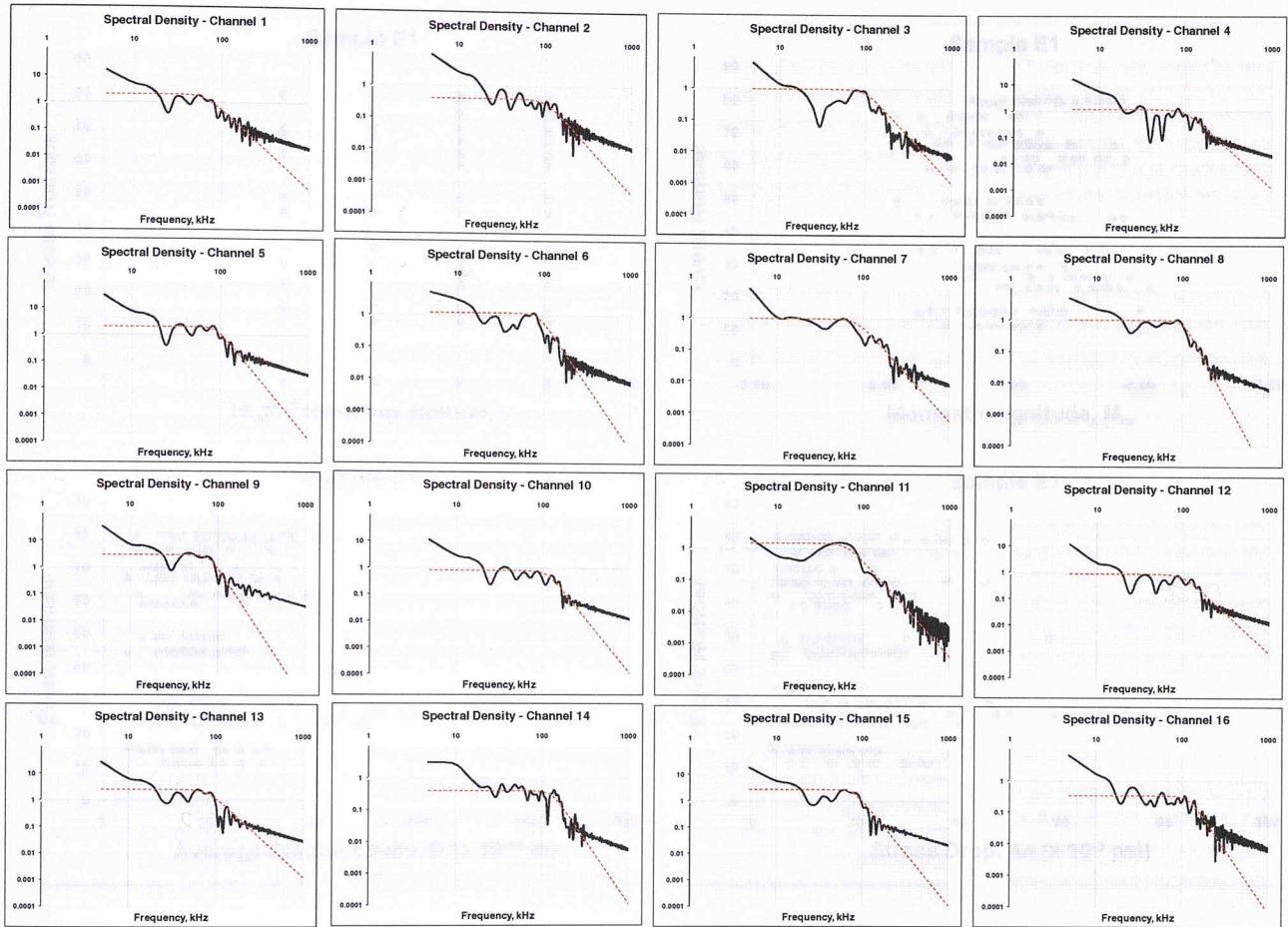


Figure 4.35: Spectral densities of AE signals associated with event 15 of experiment 1. The curves (black continuous lines) compare well with a typical displacement spectra density. The red dash lines are the spectra density models with varying corner frequencies, low-frequency amplitudes and high frequency rolloffs (2 to 5).

The source parameters for the located shear AE events of experiment 1 are plotted in Figure 4.36. The high frequency rolloff varies between 2 and 5 with radius of circular dislocation ranging from 10 to 31 mm, seismic moment ranging from 3 to 84×10^{-4} Nm, moment magnitude ranging from -8.5 to -7.5, average displacement ranging from 23 to 434 pm and stress drop ranging from 3 to 81×10^{-3} psi.

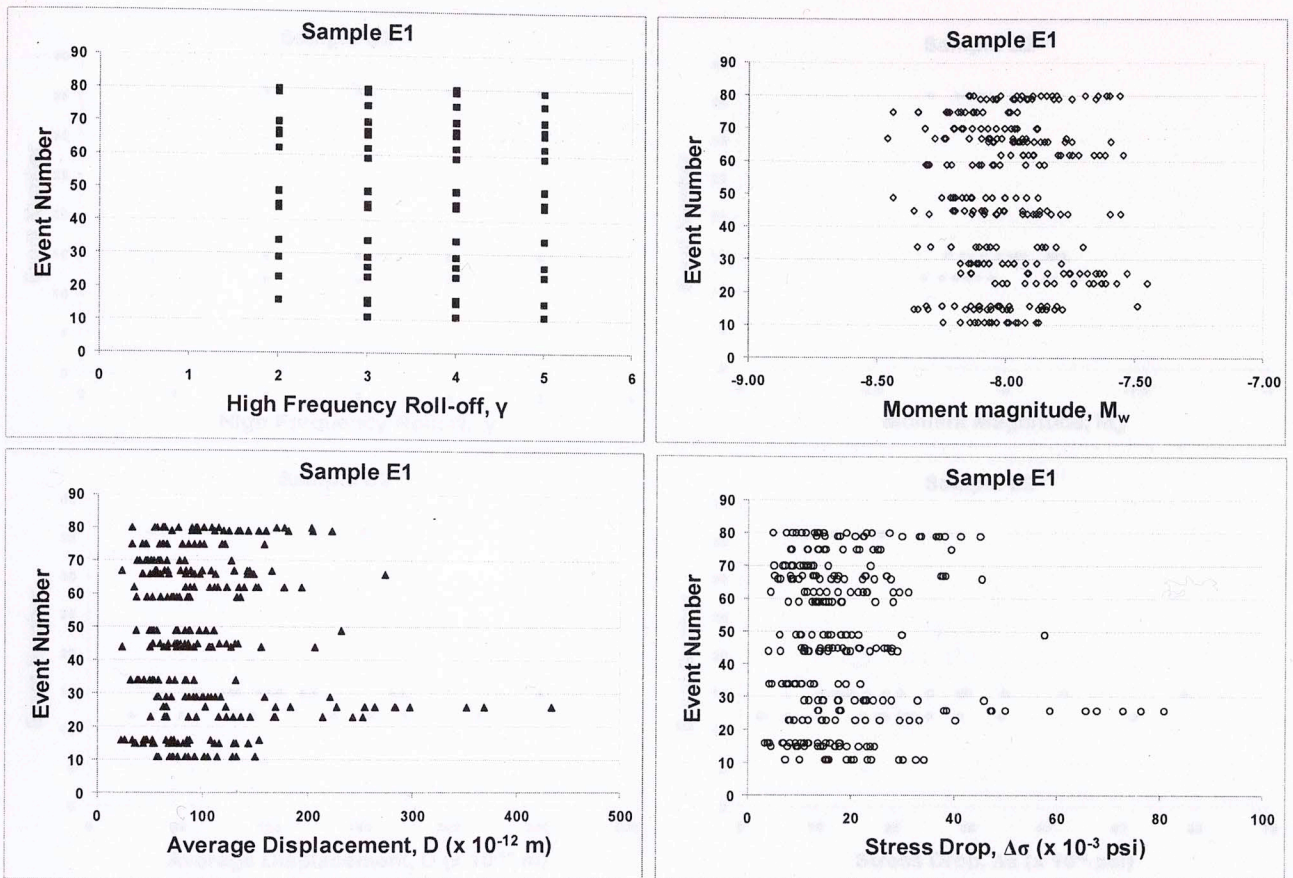


Figure 4.36: Plots of AE against source parameters of AE shear events associated with experiment 1 (fractured with mineral oil)

The source parameters for the located shear AE events of experiment 2 are plotted in Figure 4.37. The high frequency rolloff varies between 2 and 5 with radius of circular dislocation ranging from 11 to 30 mm, seismic moment ranging from 5 to 45 $\times 10^{-4}$ Nm, moment magnitude ranging from -8.3 to -7.6, average displacement ranging from 23 to 252 pm and stress drop ranging from 2 to 59 $\times 10^{-3}$ psi.

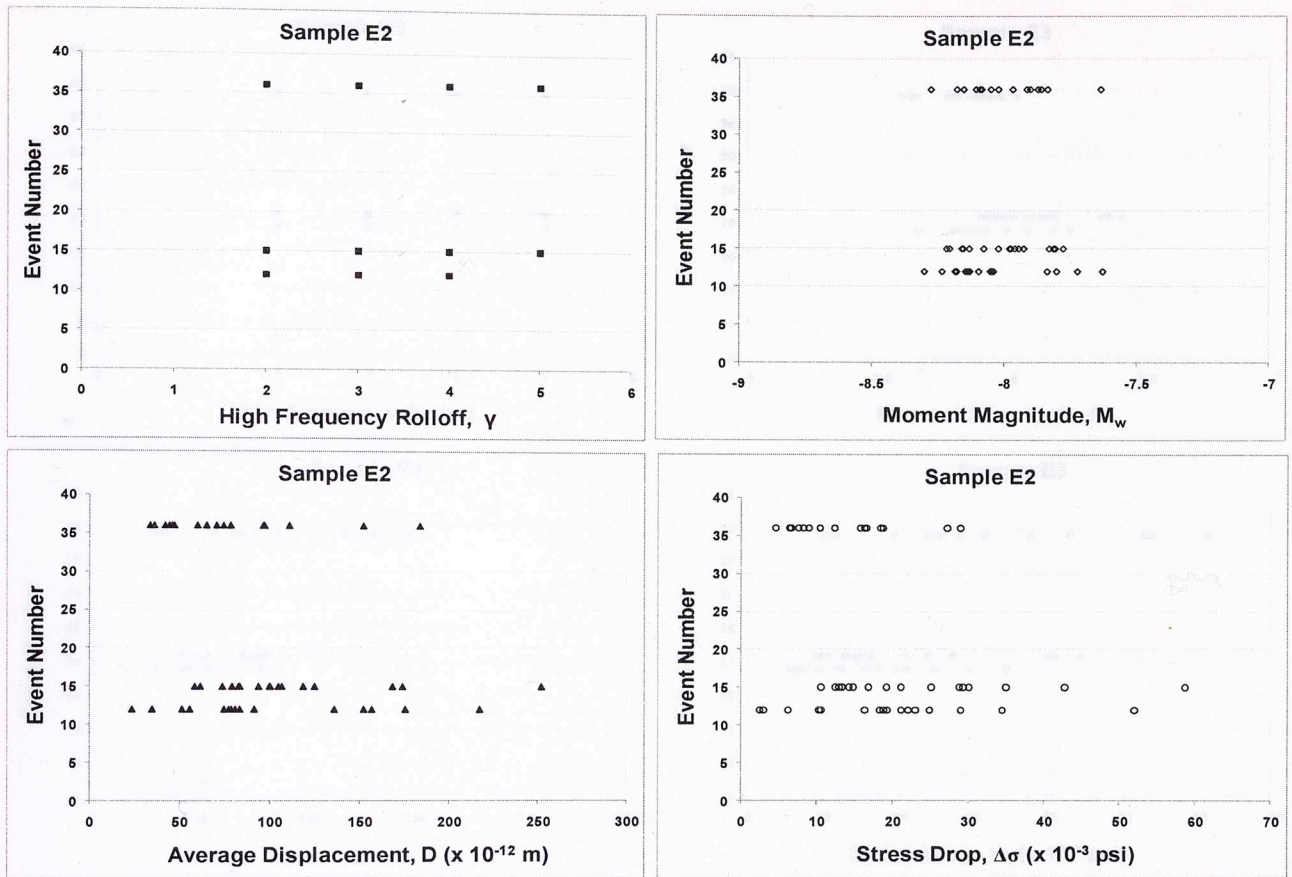


Figure 4.37: Plots of AE against source parameters of AE shear events associated with experiment 2 (fractured with water).

The source parameters for the located shear AE events of experiment 3 are plotted in Figure 4.38. The high frequency rolloff varies between 2 and 5 with radius of circular dislocation ranging from 10 to 27 mm, seismic moment ranging from 3 to 53×10^{-4} Nm, moment magnitude ranging from -8.4 to -7.6, average displacement ranging from 26 to 203 pm and stress drop ranging from 6 to 61×10^{-3} psi.

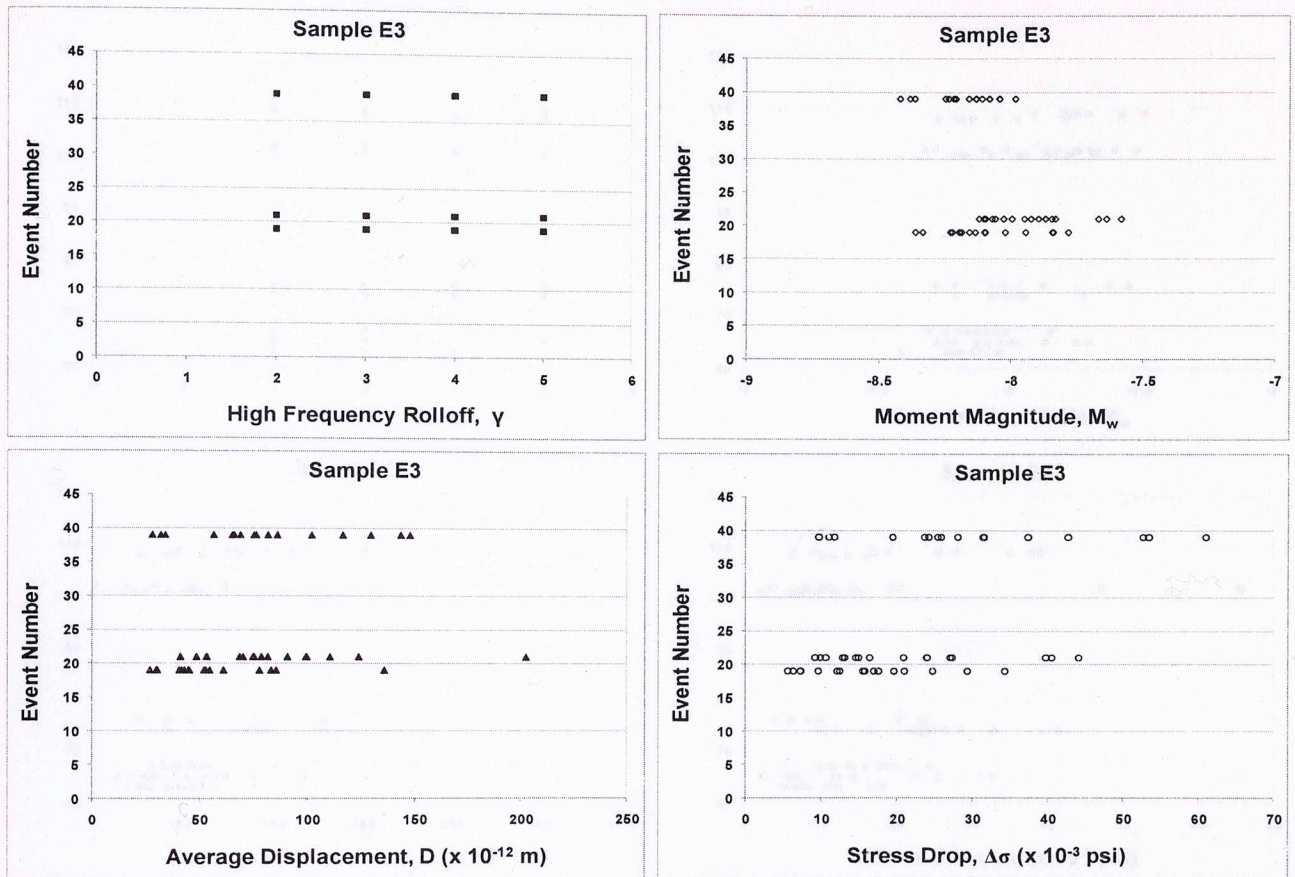


Figure 4.38: Plots of AE against source parameters of AE shear events associated with experiment 3 (fractured with water).

The source parameters for the located shear AE events of experiment 4 are plotted in Figure 4.39. The high frequency rolloff varies between 2 and 5 with radius of circular dislocation ranging from 12 to 37 mm, seismic moment ranging from 3 to 74×10^{-4} Nm, moment magnitude ranging from -8.4 to -7.5, average displacement ranging from 13 to 260 pm and stress drop ranging from 2 to 66×10^{-3} psi.

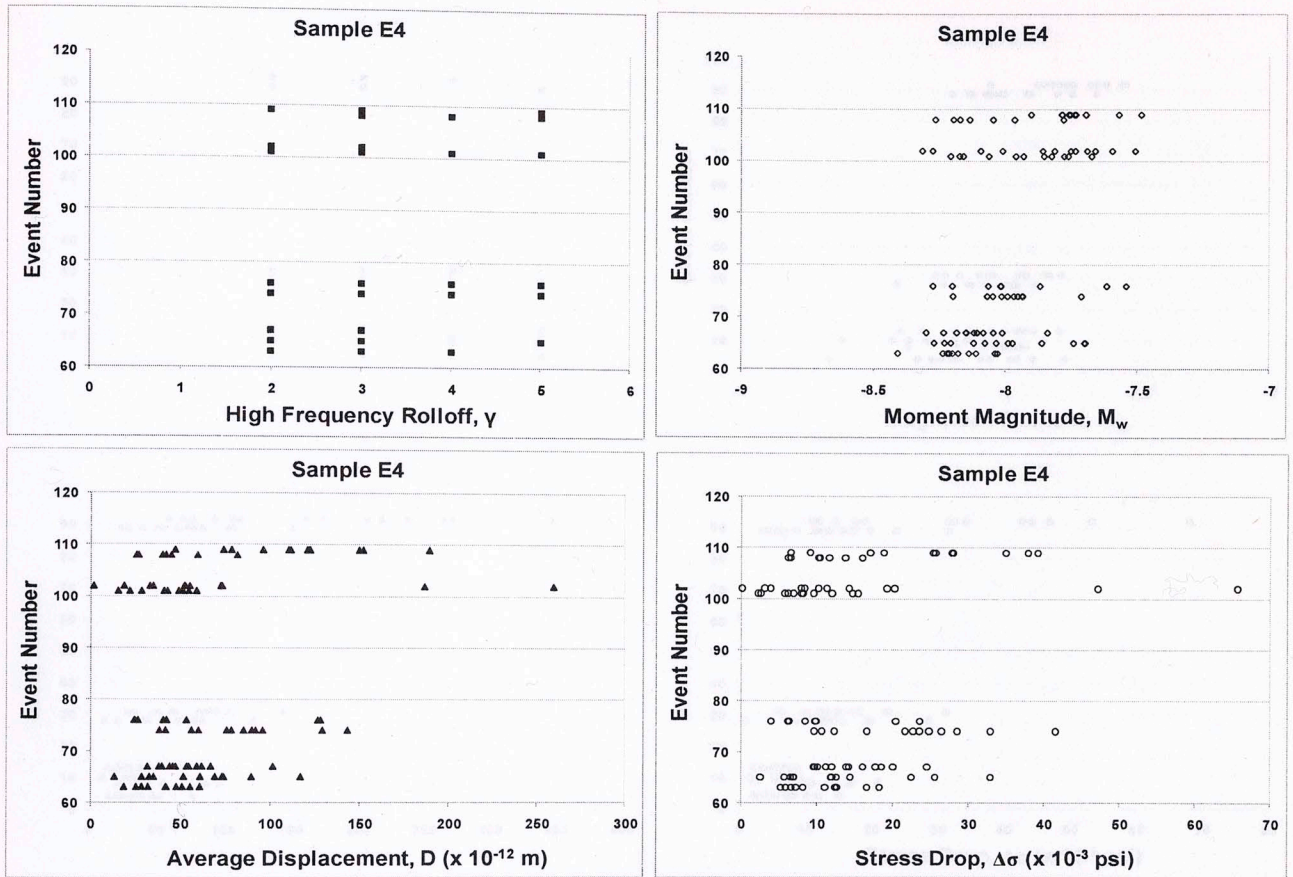


Figure 4.39: Plots of AE against source parameters of AE shear events associated with experiment 4 (fractured with mineral oil).

The source parameters for the located shear AE events of experiment 7 are plotted in Figure 4.40. The high frequency rolloff varies between 2 and 5 with radius of circular dislocation ranging from 12 to 35 mm, seismic moment ranging from 1 to 60×10^{-4} Nm, moment magnitude ranging from -8.7 to -7.6, average displacement ranging from 9 to 348 pm and stress drop ranging from 1 to 68×10^{-3} psi.

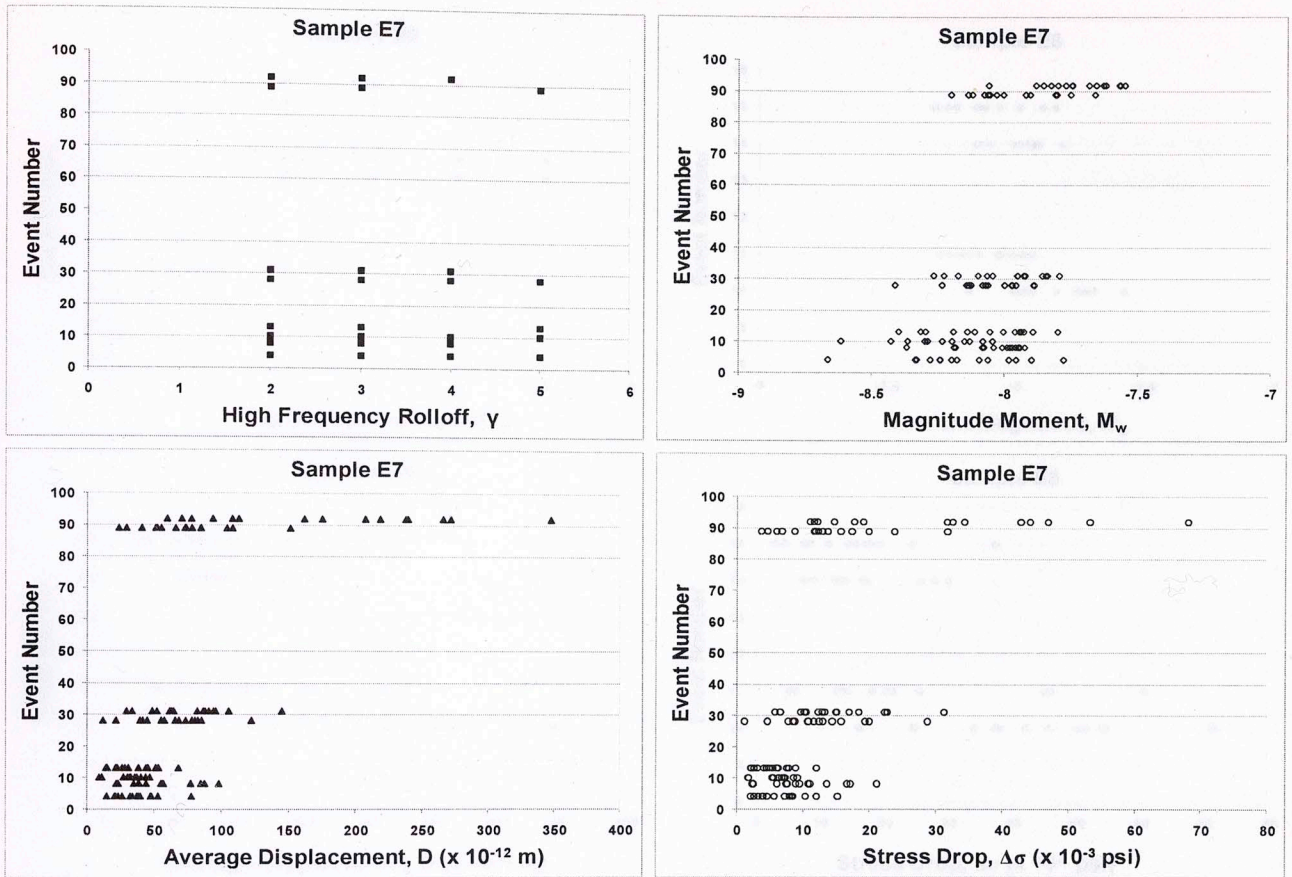


Figure 4.40: Plots of AE against source parameters of AE shear events associated with experiment 7 (fractured with mineral oil).

The source parameters for the located shear AE events of experiment 8 are plotted in Figure 4.41. The high frequency rolloff varies between 2 and 5 with radius of circular dislocation ranging from 9 to 31 mm, seismic moment ranging from 4 to 54×10^4 Nm, moment magnitude ranging from -8.3 to -7.6, average displacement ranging from 19 to 346 pm and stress drop ranging from 3 to 71×10^3 psi.

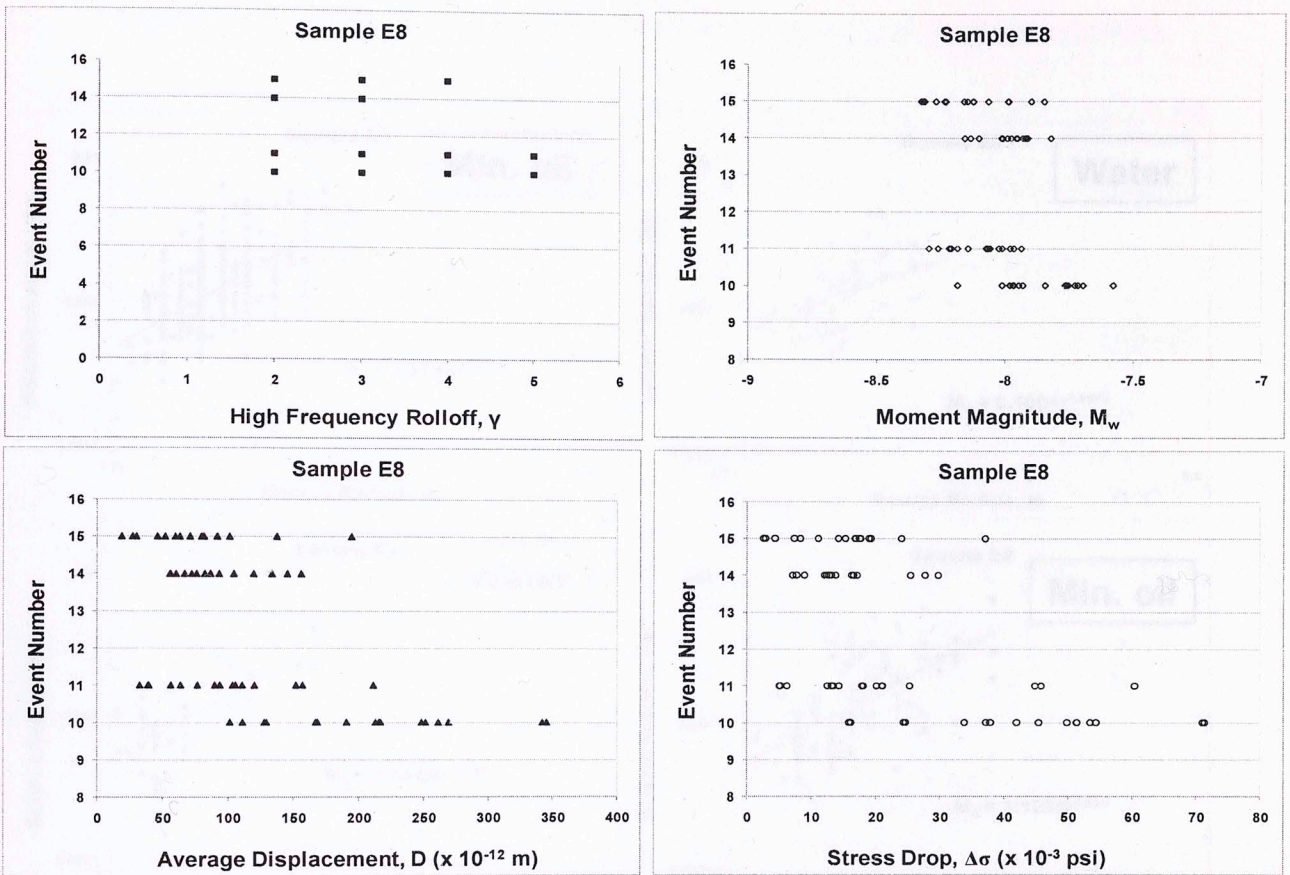


Figure 4.41: Plots of AE against source parameters of AE shear events associated with experiment 8 (fractured with water).

In summary, although there is a considerable amount of scatter in the correlations between the source parameters and cumulative shear AE, a careful examination shows some degree of consistency in their values. The high frequency rolloff for all the spectra densities varies between 2 and 5; the stress drop has an average value of about 0.02 psi; and the moment magnitude averages -8. This indicates that shear events are similar in size. Independently computed parameters like the seismic moment and radius of circular dislocation are determined to have a power law relationship in the form of $M_0 = Ar^B$ (where A and B are real number constants) as shown in Figure 4.42. The exponent, B has values between 0.75 and 1.88 which is more consistent with the model for average displacement ($B = 2$) than stress drop ($B = 3$).

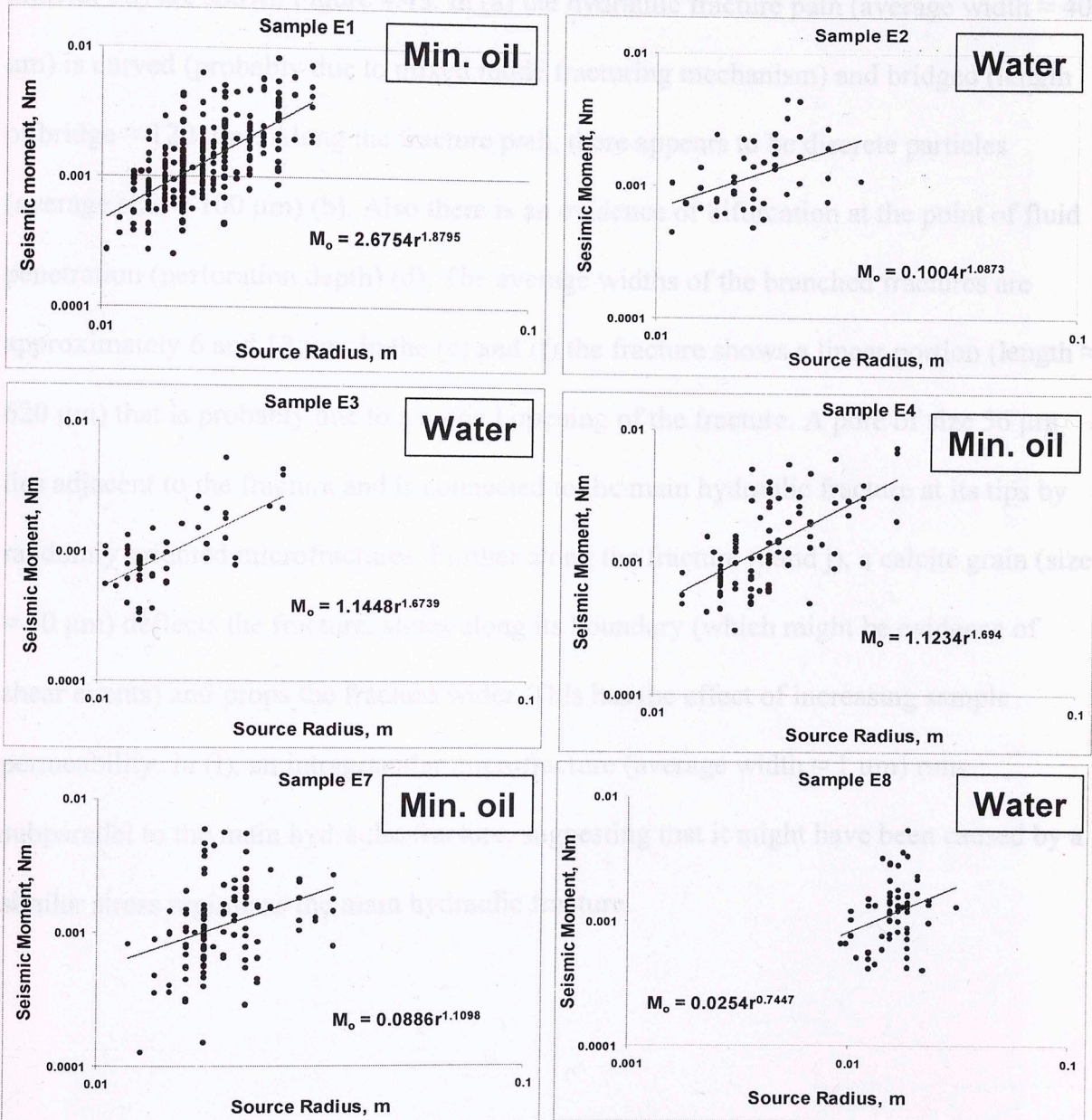
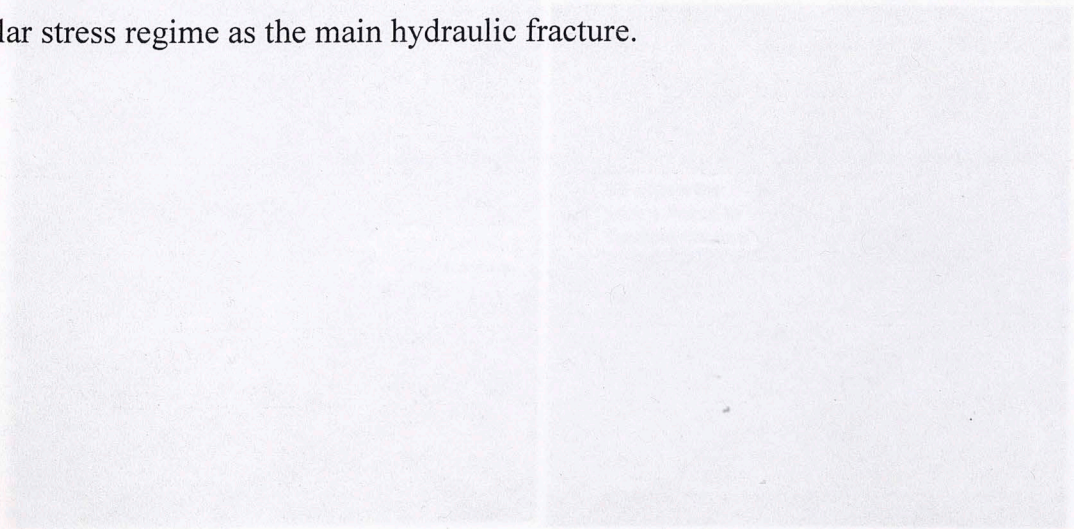


Figure 4.42: Relationship between seismic moments and source radii of AE shear events associated with experiments 1 – 4, 7 and 8. The value of the exponent is less than the predicted value of 3.

4.2.6. Hydraulic Fracture Morphology (SEM)

Hydraulic fractures intersecting the outer diameter of the 1” over-cored plug were studied in an SEM. (FEI Quanta 200TM) using both backscatter and secondary electron detectors.

Several aspects of hydraulic fracture morphology of sample E1 (fractured with mineral oil) are shown Figure 4.43. In (a) the hydraulic fracture path (average width $\approx 40 \mu\text{m}$) is curved (probably due to mixed mode fracturing mechanism) and bridged (length of bridge $\approx 120 \mu\text{m}$). Along the fracture path, there appears to be discrete particles (average size $\approx 100 \mu\text{m}$) (b). Also there is an evidence of bifurcation at the point of fluid penetration (perforation depth) (d). The average widths of the branched fractures are approximately 6 and 12 μm . In the (e) and (f) the fracture shows a linear portion (length $\approx 620 \mu\text{m}$) that is probably due to a mode I opening of the fracture. A pore of size 56 μm lies adjacent to the fracture and is connected to the main hydraulic fracture at its tips by randomly oriented microfractures. Further along the fracture (i and j), a calcite grain (size $\approx 50 \mu\text{m}$) deflects the fracture, slides along its boundary (which might be evidence of shear events) and props the fracture wider. This has the effect of increasing sample permeability. In (l), an intragranular microfracture (average width $\approx 1 \mu\text{m}$) runs subparallel to the main hydraulic fracture, suggesting that it might have been caused by a similar stress regime as the main hydraulic fracture.



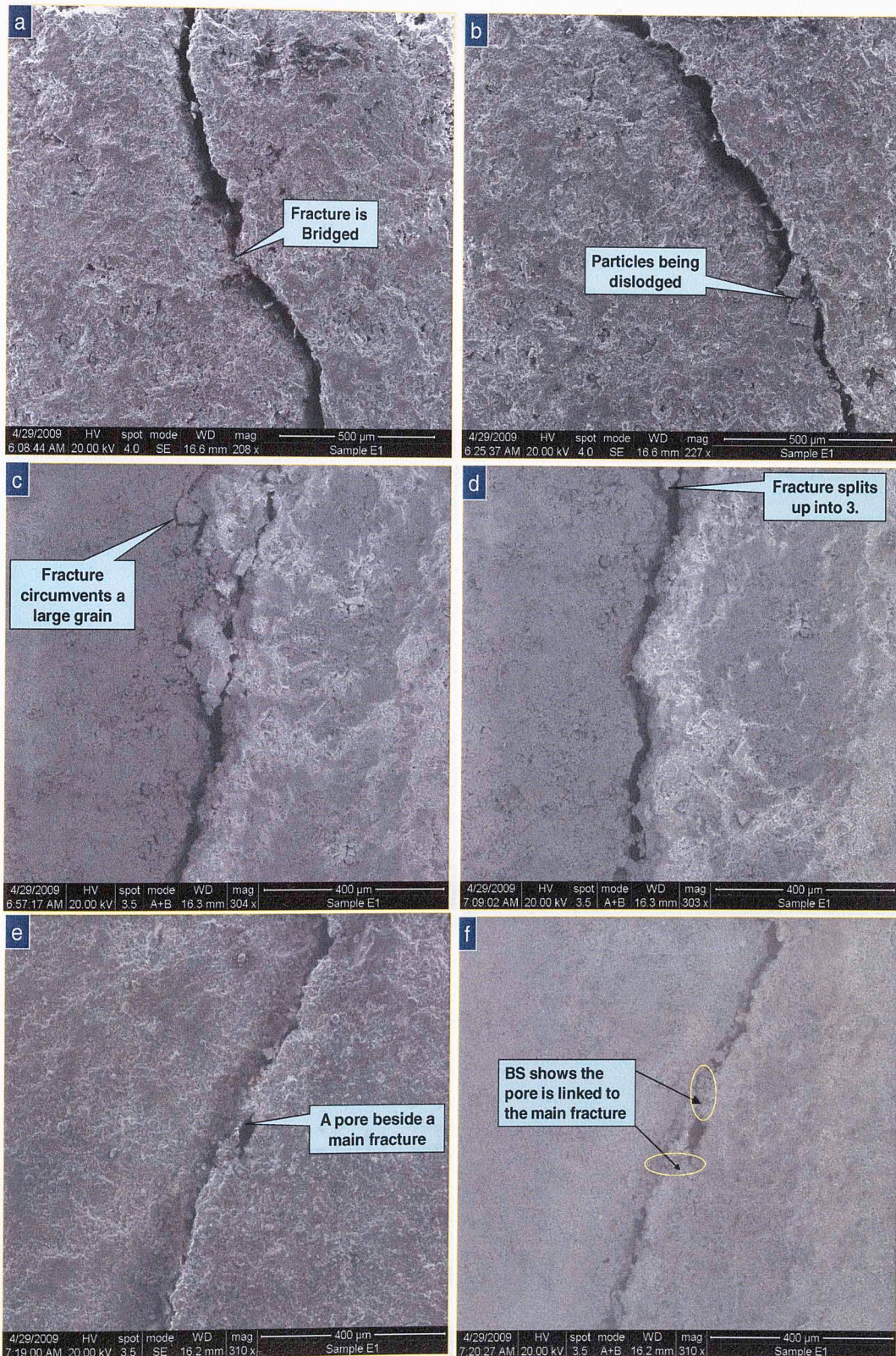


Figure 4.43: Post-fracture SEM images of Experiment 1 (Sample E1 is fractured with mineral oil). Images are from the outer surface of a 1-inch core plug drilled through the center of the fractured sample, along the length of the wellbore. This view is parallel to the fracture propagation direction. Fracture is non-planar and displays complicated bifurcations.

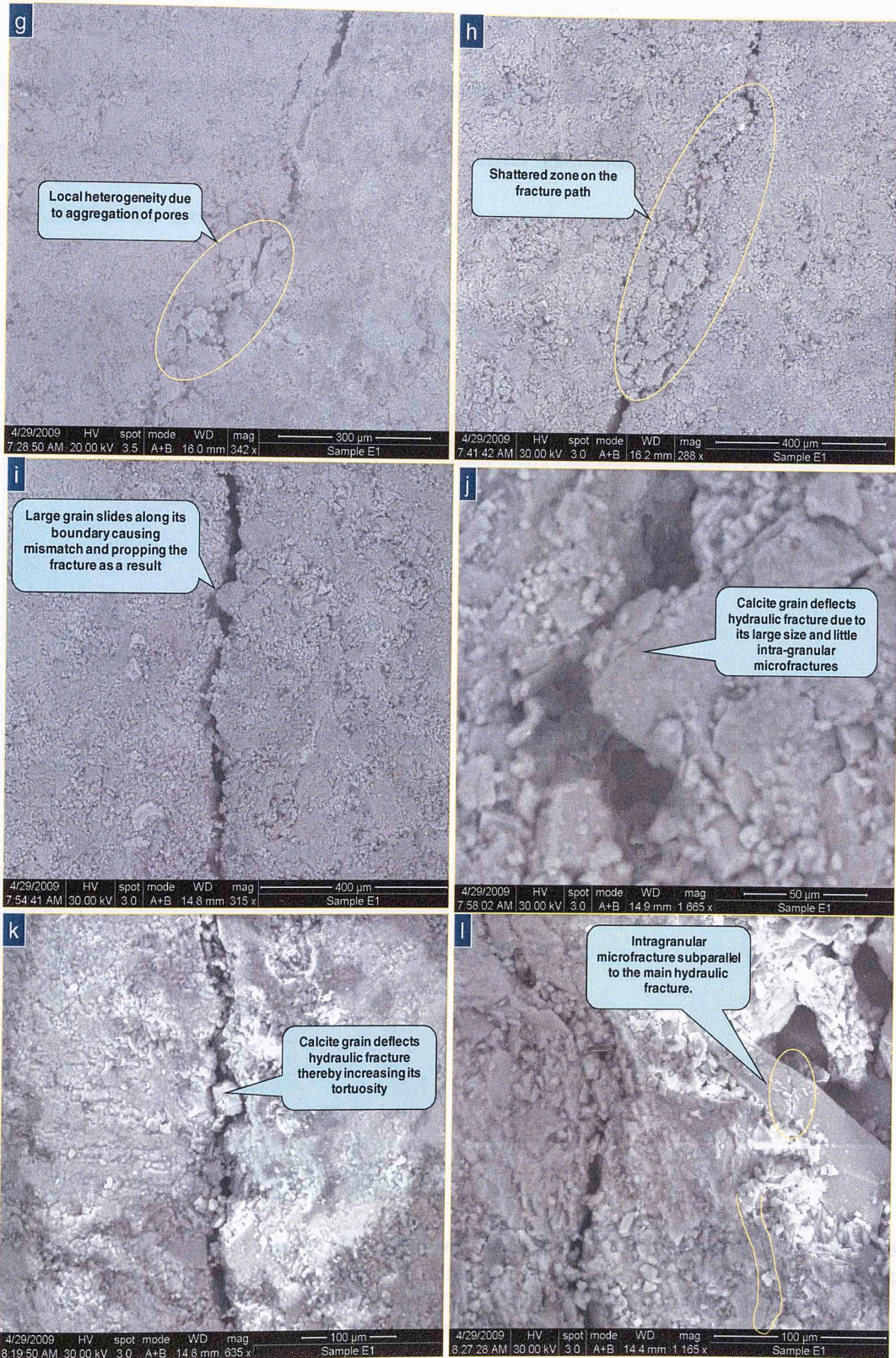


Figure 4.43: Continued

Similar phenomena of microfractures within and around grains are observed in sample E3 (fractured with water) although its preexisting flaws (mainly pores of diameter between 20 and 100 μm) appeared to have been enlarged (see Figure 4.45).

Virgin texture of sample E2 (fractured with water) depicts a set of parallel microcracks (average width $< 1\mu\text{m}$) as shown in Figure 4.44. However, there is no visible hydraulic fracture. But at high magnifications, inter-granular and intra-granular microfractures that are less than $0.5\mu\text{m}$ could be seen.

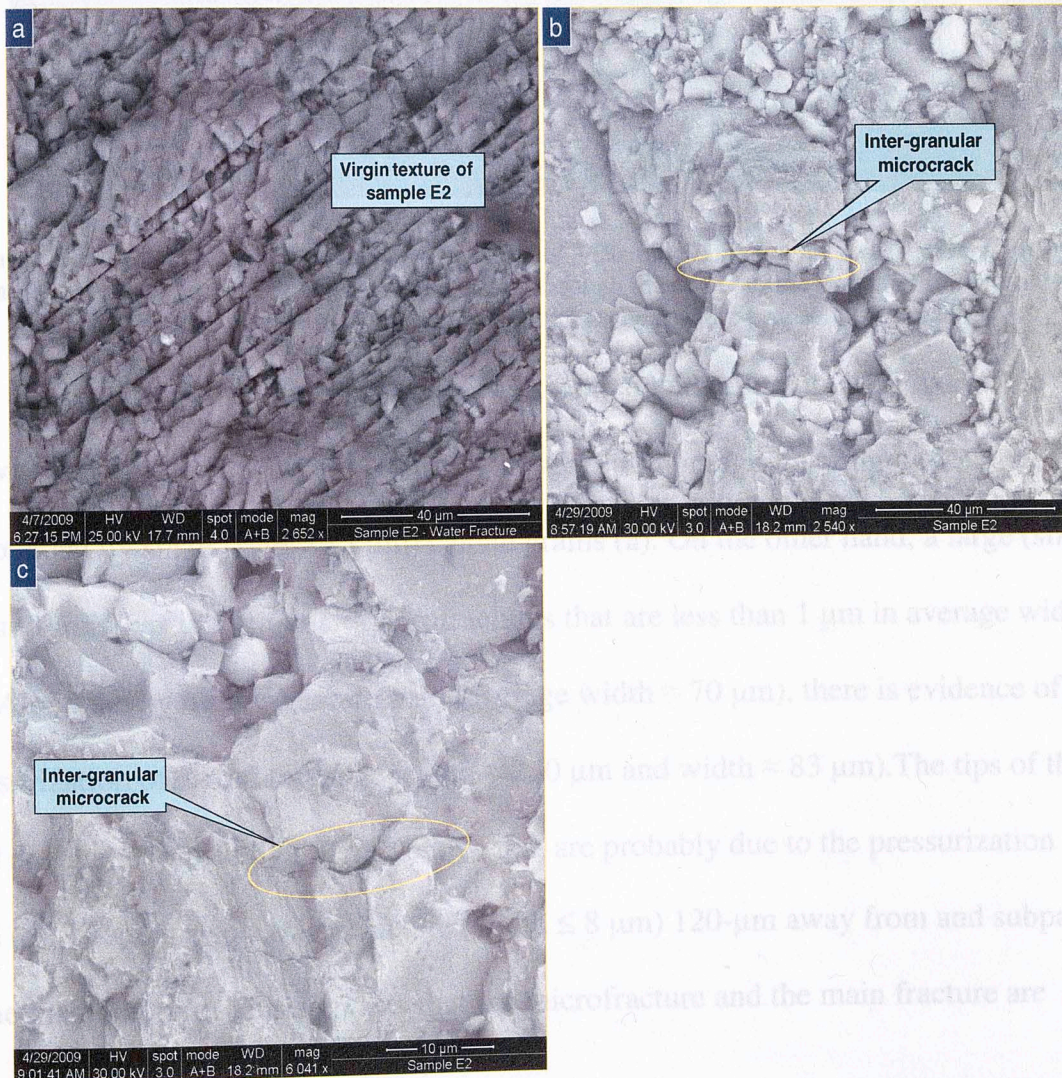


Figure 4.44: Post-fracture SEM images of Experiment 2 (Sample E2 is fractured with water). Images are from the outer surface of a 1-inch core plug drilled through the center of the fractured sample, along the length of the wellbore. This view is parallel to the fracture propagation direction. Inter-granular microcracks are observed.

Similar phenomena of microfractures within and around grains are observed in sample E3 (fractured with water) although its preexisting flaws (mainly pores of diameter between 20 and $100\mu\text{m}$) appeared to have been enlarged (see Figure 4.45).

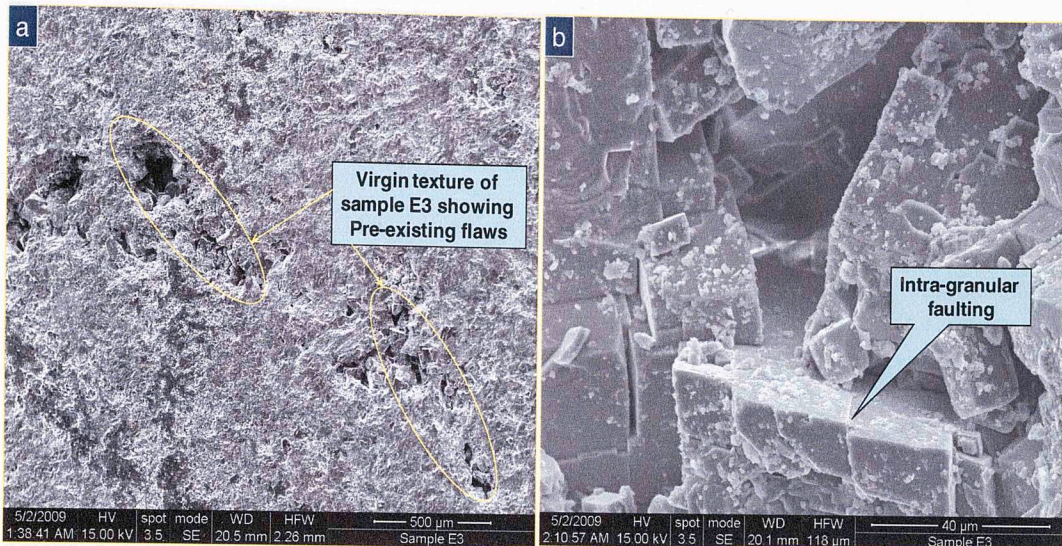


Figure 4.45: Post-fracture SEM images of Experiment 3 (Sample E3 is fractured with water). Images are from the outer surface of a 1-inch core plug drilled through the center of the fractured sample, along the length of the wellbore. This view is parallel to the fracture propagation direction.

The unfractured part of sample E4 (fractured with mineral oil) (Figure 4.46) shows a dolomite grain (size $\approx 70 \mu\text{m}$) with very little intragranular microfracture surrounded by small (size $\approx 15 \mu\text{m}$) calcite grains (a). On the other hand, a large (size $\approx 63 \mu\text{m}$) grain has intragranular microfractures that are less than $1 \mu\text{m}$ in average width (b). Along the hydraulic fracture path (average width $\approx 70 \mu\text{m}$), there is evidence of fluid pressurization of a void (average length $\approx 280 \mu\text{m}$ and width $\approx 83 \mu\text{m}$). The tips of the void are characterized by microfractures that are probably due to the pressurization of the void (c). There is also a microfracture (width $\leq 8 \mu\text{m}$) 120- μm away from and subparallel to the main fracture. This suggests that the microfracture and the main fracture are formed by similar stress regime.

Figure 4.46: Post-fracture SEM images of Experiment 4 (Sample E4 is fractured with mineral oil). Images are from the outer surface of a 1-inch core plug drilled through the center of the fractured sample, along the length of the wellbore. This view is parallel to the fracture propagation direction.

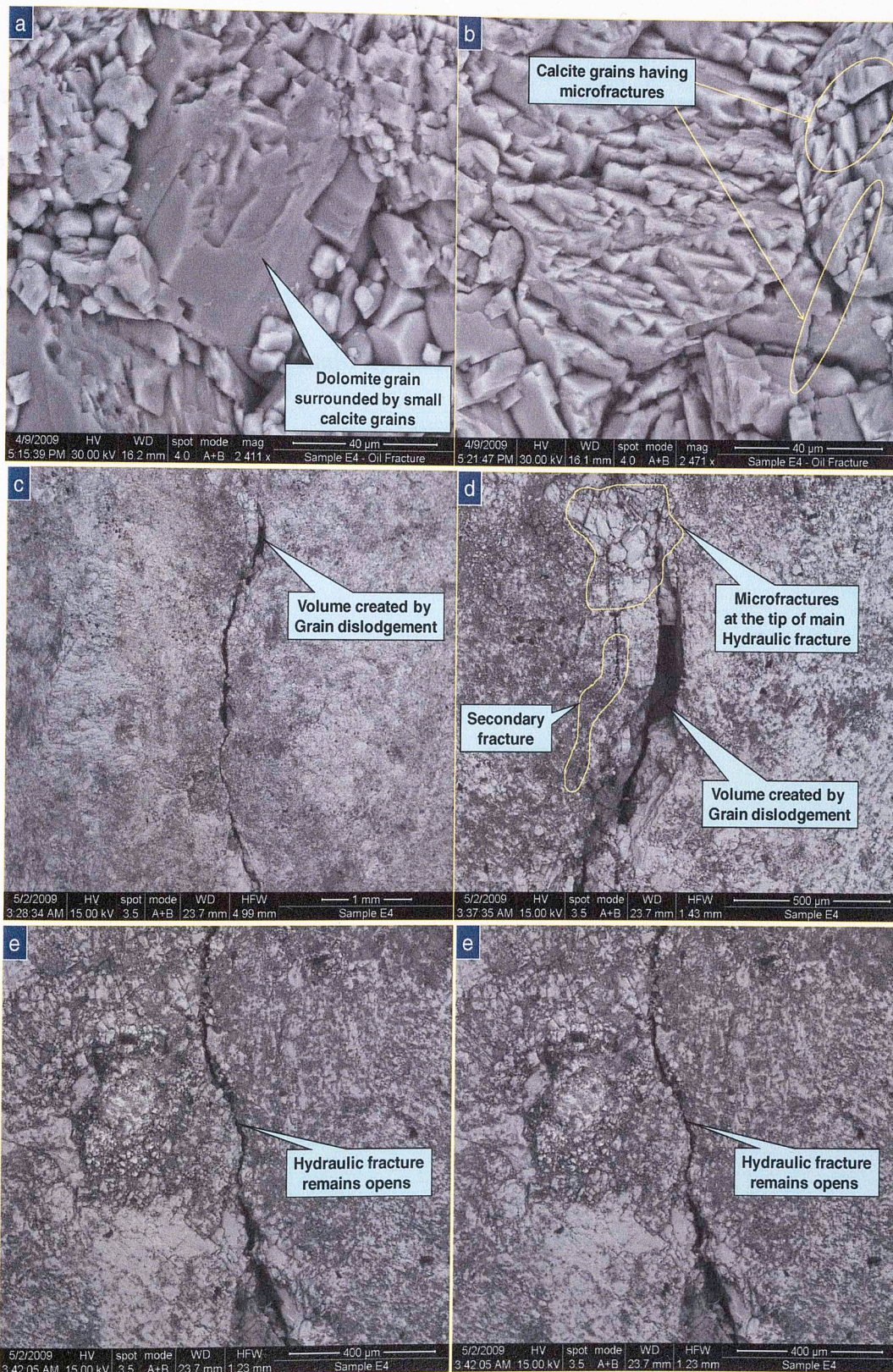


Figure 4.46: Post-fracture SEM images of Experiment 4 (Sample E4 is fractured with mineral oil). Images are from the outer surface of a 1-inch core plug drilled through the center of the fractured sample, along the length of the wellbore. This view is parallel to the fracture propagation direction.

Similar observations are made in samples E7 (fractured with mineral oil) hydraulic fracture as shown in Figure 4.47. There is a tensile opening (on a curved path) of approximately $5\ \mu\text{m}$ in width. A large portion of the hydraulic fractures is filled with rock particles with size $\leq 7\ \mu\text{m}$. Also, in (c) - (f), the hydraulic fracture paths are deflected by relatively larger particles (size $\leq 37\ \mu\text{m}$) giving rise to microcracks (size $\leq 2\ \mu\text{m}$) that are subparallel to the main hydraulic fracture.

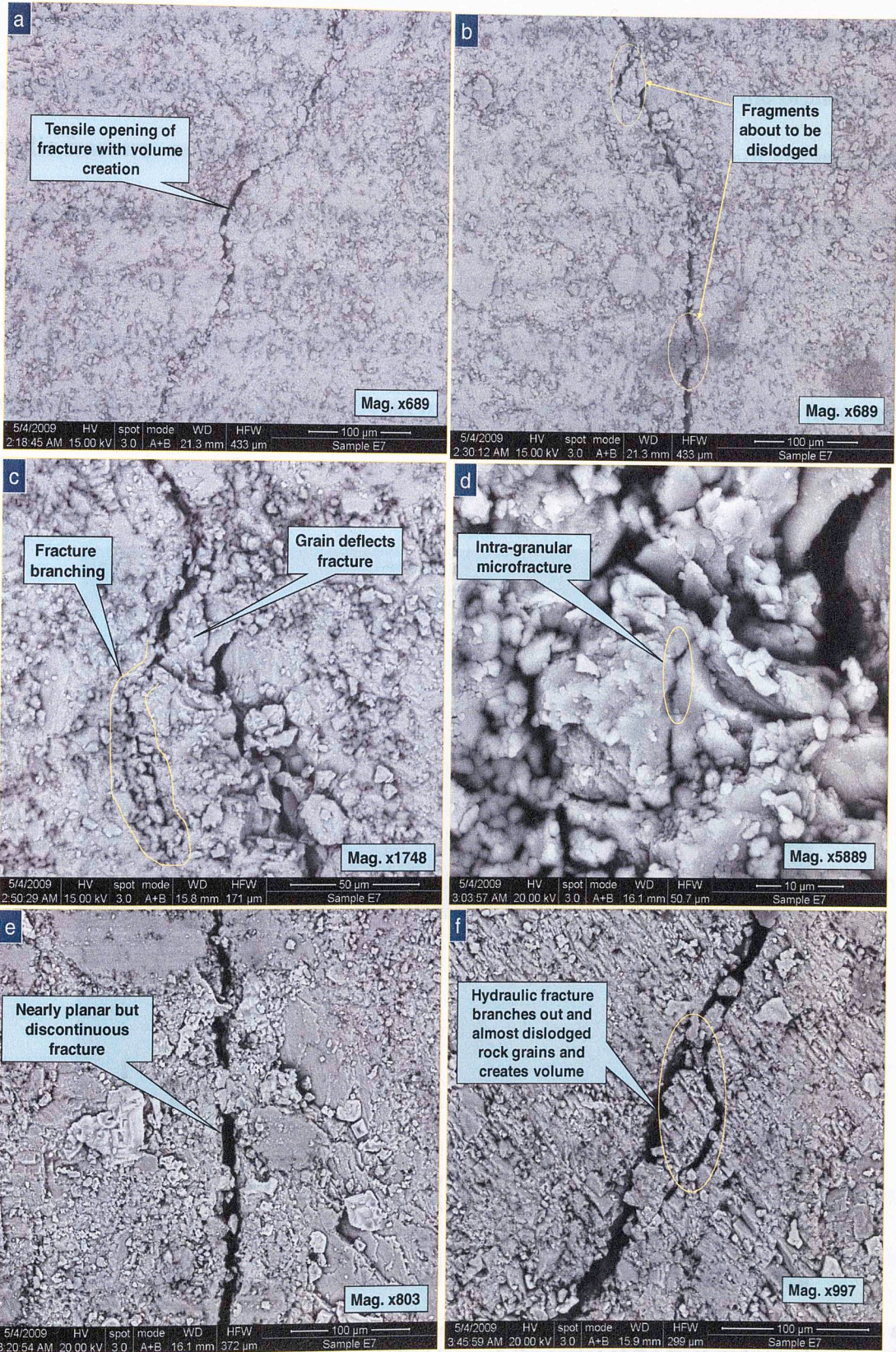


Figure 4.47: Post-fracture SEM images of Experiment 7 (Sample E7 is fractured with mineral oil). Images are from the outer surface of a 1-inch core plug drilled through the center of the fractured sample, along the length of the wellbore. This view is parallel to the fracture propagation direction.

In experiment 8, the hydraulic fracture of sample E8 (fractured with water) splits at the perforation depth as shown in Figure 4.48. The average width of the branched hydraulic fractures ranged from 14 to 28 μm . There is also an evidence of shearing and a degree of mismatch between the fractures surfaces which has the tendency of enlarging, propping the fracture aperture wider, thereby increasing its bulk permeability. An interesting phenomenon can be seen in (c) and (d) where a propagating microcrack (average width $\approx 85 \text{ nm}$) is arrested by an intragranular relatively larger pore (average width $\approx 400 \text{ nm}$).

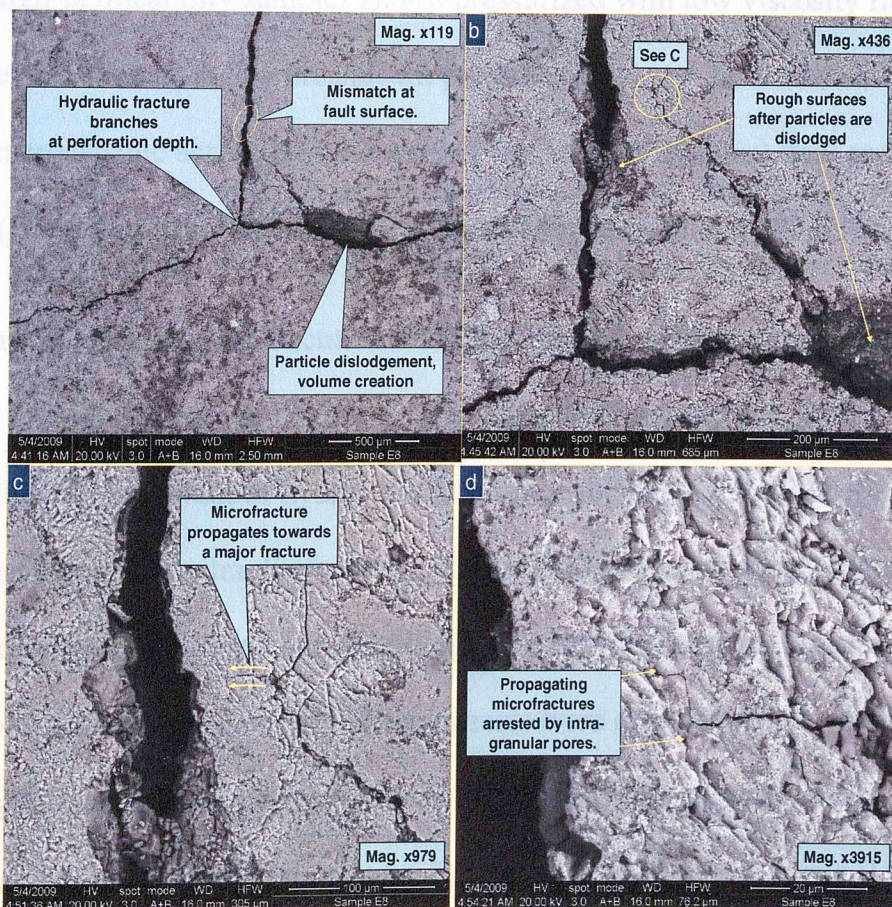


Figure 4.48: Post-fracture SEM images of Experiment 8 (Sample E8 is fractured with water). Images are from the outer surface of a 1-inch core plug drilled through the center of the fractured sample, along the length of the wellbore. This view is parallel to the fracture propagation direction.

In summary, the hydraulic fractures imaged from the surface trace of 1-inch core samples can be qualitatively classified into 2 groups. Group A (samples E1, E4, E7 and E8) have clearly defined fractures while group B (sample E2 and E3) do not. Group A are low-permeability samples and/or pressurized with high viscosity fluid. They are created at high breakdown pressures (between 2634 and 3355 psi), low fluid pump rate (2 cc/min), and have high microseismic activities (between 80 and 120 events in less than 10 minutes) and frequency content between 39 and 391 KHz. On the other hand, group B (sample E2 and E3) do not have clearly defined hydraulic fractures. They are from relatively high-permeability samples and/or pressurized with low viscosity fluid (1-cp water). They are created at low breakdown pressures (between 1229 and 1895 psi) and have low microseismic activities (50 events in less than 10 minutes), low and high fluid pump rate (2 and 4 cc/min) and frequency content between 39 and 186 KHz.

Some of the hydraulic fractures are either bridged or filled with rock particles which tend to reduce effective fracture permeability. Rock particles of relatively larger sizes than the average width of hydraulic fractures have the potential of deflecting and changing the course of hydraulic fractures. This contributes enormously to the non-planarity of hydraulic fractures and greatly impacts hydraulic fracture treatments as most models assume planar geometries. Fracture arrests were also noticeable when propagating microcracks encounter wider hydraulic fractures or pores. The non-planarity of the hydraulic fractures suggests that neither pure mode I nor pure mode II can explain the fracturing mechanisms (Cosgrove and Engelder, 2004).

CONCLUSION

Some of the most important conclusions from this study are stated as follows:

- a. The hydraulic fractures created from the fluid-pressurization of sample boreholes are mostly contained within the samples and resulted from the reactivation of preexisting cracks. Containment resulted from the simple laboratory procedure we developed.
- b. The induced hydraulic fractures fall into two groups. Group A have clearly defined hydraulic fractures ($w_f \approx 5 - 70 \mu\text{m}$) at $\frac{1}{2}$ inch from the center of the wellbore. They are low-permeability samples and/or pressurized with high-viscosity fluid. The breakdown pressures and AE activities are relatively high and frequency content of associated AE signal range between 39 and 391 KHz. On the other hand, group B do not have clearly defined hydraulic fractures and are associated with relative low breakdown pressures, low AE activity and frequency content of AE signals in the range, 39 – 186 KHz. Thus, the results from this study suggest that breakdown pressures of hydraulic fractures are often associated with a certain level of AE activity and breakdown pressure is a function of treatment fluid viscosity as well as formation permeability.
- c. Focal plots of the AE events suggest that the processes responsible for the hydraulic fractures are complex and not simple mode I, tensional fractures. At some scale, that causes the non-planarity of the resultant hydraulic fractures. The shear events show mixed faulting mechanisms with normal faulting dominating, thereby suggesting a prevalence of extensional deformation.

- d. Analysis of source mechanisms shows that the stress drops and displacements associated with individual events are small. The displacements are much smaller than the grain dimensions. However, the source radius (equivalent to the area of fracture events) is relatively large (many grain diameters). These observations are consistent with the reactivation of pre-existing flaws.

REFERENCES

- Aki, K., 1980: "Quantitative Seismology of Reservoir Rocks Using Fourier Transform Inverted Spectra", paper (SPE 113023-STU) presented as part of the student paper contest associated with the SPE Annual Technical Conference and Exhibition, 1984 November, Anaheim, California, U.S.A.
- Ballard, B.D., 2002: "Quantitative Seismology of Reservoir Rocks Using Fourier Transform Inverted Spectra", paper (SPE 113023-STU) presented as part of the student paper contest associated with the SPE Annual Technical Conference and Exhibition, 1984 November, Anaheim, California, U.S.A.
- Barree, R.D., 1985: "A Practical Numerical Simulator for Three-Dimensional Fracture Propagation in Heterogeneous Media", SPE paper 12273 presented at the SPE Reservoir Simulation Symposium, San Francisco, California, U.S.A.
- Bennett, C.O., Rosato, N.D., Reynolds, A.C. and R. Raghavan, 1983: "Influence of Fracture Heterogeneity and Wing Length on the Response of Vertically Fractured Wells", SPE Journal (April), 219 - 250.
- Boatwright, J., 1980: "A Spectral Theory for Circular Seismic Sources: Simple Estimates of Source Dimension, Dynamic Stress Drop, and Radiated Seismic Energy", Bull. Seism. Soc. Am. 70, No. 1, pp. 1-27.
- Brace, W.F., 1964, "Brittle fracture of Rocks", in State of Stress in the Earth Crust, Judd, W.R. ed., Elsevier, New York, pp. 111-174.
- Brune, J.N., 1970: "Tectonic Stress and the Spectra of Seismic Shear Waves from Earthquakes", Journal of Geophysical Research, Vol. 75, No. 26, pp. 4997 - 5009.

REFERENCES

- Aki, K. and P.G. Richards, 2002: "Quantitative Seismology", 2nd Edition, University Science Books, Sausalito, California, U.S.A. pp. 27 – 62.
- Ballard, B.D., 2007: "Quantitative Mineralogy of Reservoir Rocks Using Fourier Transform Infrared Spectroscopy", paper (SPE 113023-STU) presented as part of the student paper contest associated with the SPE Annual Technical Conference and Exhibition, 11-14 November, Anaheim, California, U.S.A.
- Barree, R.D., 1983: "A Practical Numerical Simulator for Three-Dimensional Fracture Propagation in Heterogeneous Media", SPE paper 12273 presented at the SPE Reservoir Simulation Symposium, San Francisco, California, U.S.A.
- Bennett, C.O., Rosato, N.D., Reynolds, A.C. and R. Raghanvan, 1983: "Influence of Fracture Heterogeneity and Wing Length on the Response of Vertically Fractured Wells", SPE Journal (April), 219 – 230.
- Boatwright, J. 1980: "A Spectral Theory for Circular Seismic Sources; Simple Estimates of Source Dimension, Dynamic Stress Drop, and Radiated Seismic Energy", Bull. Seism. Soc. Am. 70, No. 1, pp. 1-27.
- Brace, W.F., 1964: "Brittle fracture of Rocks", in State of Stress in the Earth Crust, Judd, W.R. ed., Elsevier, New York, pp. 111-174.
- Brune, J.N., 1970: "Tectonic Stress and the Spectra of Seismic Shear Waves from Earthquakes", Journal of Geophysical Research, Vol. 75, No. 26, pp. 4997 – 5009.

- Clark, J.B., 1949: "A Hydraulic process for Increasing the Productivity of Wells",
Petrol. Trans. AIME., v. 186, pp. 1-8.
- Clifton, R.J. and A.S. Abou-Sayed, 1979: "On the Computation of the Three-
Dimensional Geometry of Hydraulic Fractures", SPE paper 7943, presented at the
SPE/DOE Low Permeability Gas Reservoirs Symposium, Denver, Colorado,
U.S.A.
- Cone, M.P., and D.G. Kersey, 1992: "Porosity, Part-5, Laboratory Methods", Core
Laboratories, Division of Western Atlas Int'l, Inc., Houston, Texas, U.S.A.
- Coretest Systems, Incorporated, 2002: "Product Overview, AP-608, Automatic
Klinkenberg permeameter/porosimeter", Coretest Systems, Incorporated,
Morgan Hill, California, U.S.A.
- Cornet, F.H. and P.H. Julien, 1989: "Stress Determination From Hydraulic Test Data and
Focal Mechanisms of Induced Seismicity", Int. J. Rock. Mech. Min. Sci. &
Geomech. Abstr. Vol. 26, No. 34, pp. 235-248.
- Cosgrove, J.W. and T. Engelder (eds), 2004: "The initiation, Propagation, and Arrest of
Joints and Other Fractures", Geological Society, London, Special Publications.
pp. 231, 223 – 242.
- Coulomb, C.A., 1773: "Application of the Rules of Maxima and Minima to some
Problems of Statics Related to Architecture", Acad. Roy. Sci. Mem. Math. Phys.,
7, pp. 343 -82.
- Cronin, V., 2004: "A Draft Primer on Focal Mechanism Solutions for Geologists",
Baylor University, Baylor, Texas.

- Daneshy, A.A., 1973: "A Study of Inclined Hydraulic Fractures", SPE Paper 4062, Society of Petroleum Engineers Journal.
- Daneshy, A.A., 1974: "Hydraulic Fracture Propagation in the Presence of Planes of Weakness", SPE Paper 4852, American Institute of Mining, Metallurgical, and Petroleum Engineers, Inc.
- DaqScribe Technology, Inc., 2003: "ICS-645: High-Speed, High-Precision, and High-Density ADC Board", DaqScribe Technology, Inc.
- Detournay, E., McLennan, J.D. and J.-C. Roegiers, 1986: "Poroelastic Concepts Explain Some of the Hydraulic Fracturing Mechanisms", SPE paper 15262.
- Digital Wave Corp., 2004: "FM-1™ User Manual", Digital Wave Corp., Colorado, U.S.A.
- Digital Wave Corp., 2005: "FM-1™ System Assembly", Digital Wave Corp., Colorado, U.S.A.
- Digital Wave Corp., 2009: "Acoustic Emission Sensors", Online at http://www.digitalwavecorp.com/mae_sensors.html
- Fall, S.D., Young, R.P., Carlson, S.R., and T. Chow, 1992: "Ultrasonic Tomography and Acoustic Emission in Hydraulically Fractured Lac du Bonnet Grey Granite", Journal of Geophysical Research, Vol. 97, No. B5, pp. 6867-6884, May 1992.
- Gautschi, G., 2002: "Piezoelectric Sensorics: Force, Strain, Pressure, Acceleration and Acoustic Emission Sensors, Materials and Amplifiers", Springer-Verlag, Berlin, Germany. pp. 1-3.

- Gidley, J.L., Holditch, S.A., Nierode, D.E., and W. Ralph, 1989: "Recent Advances in Hydraulic Fracturing" SPE monograph volume 12, Richardson, Texas, U.S.A., pp. 81-94.
- Gross, C., 2002: "Hsu Nielsen Source", Online at <http://www.ndt.net/ndtaz/ndtaz.php>
- Grechka, V., Mazumdar, P., and S.A. Shapiro, 2009: "Predicting Permeability and Gas Production of Hydraulically Fractured Tight Sands from Microseismic Data", Geophysics.
- Haimson, B. and C. Fairhurst, 1969: "Hydraulic Fracturing in Porous Permeable Materials", J. Pet. Tech., pp. 811 – 817.
- Hanks, T.C. and M. Wyss, 1972: "The Use of Body Wave Spectra in the Determination of Seismic-Source Parameters", Bull. Seism. Soc. Am. 62, 561 – 581.
- Hardy, H.R., 2003: "Acoustic Emission/Microseismic Activity: Principle. Techniques, and Geotechnical Applications", A.A. Balkema Publishers, Swets and Zeitlinger B.V., Lisse, The Netherlands, Vol. 1, pp. 1-21.
- Hill, R.E., Peterson, R.E., Warpinski, N.R., Lorenz, J.C., Teufel, L.W. and J.K. Aslakson, 1994: "Techniques for Determining Subsurface Stress Direction and Assessing Hydraulic Fracture Azimuth", paper SPE 29192 presented at the Eastern Regional Conference and Exhibition, Charleston, WV, U.S.A., 8 -10 November.
- Hubbert, M.K. and D.G. Willis, 1957: "Mechanics of Hydraulic Fracturing", Tran. AIME, Vol. 210, pp. 153 – 168.
- Howard, G.C. and C.R. Fast, 1970, Hydraulic Fracturing, SPE Monograph Series, Society of Petroleum Engineers, Richardson, Texas, USA.

- Irwin, G.R., 1957: "Analysis of Stresses and Strains Near the End of a Crack Traversing a Plate", J. Appl. Mech., 24, pp. 361 – 364.
- Ishida, T., Chen, Q., Mizuta, Y., and J.C. Roegiers, 2004: "Influence of Fluid Viscosity on Hydraulic Fracture Mechanism", Journal of Energy Resources Technology, Vol. 126, September, 2004.
- Jaeger, J.C., Cook, N.G.W. and R.W. Zimmerman, 2007, Fundamentals of Rock Mechanics, 4th Edition, Blackwell Publishing Limited, Malden, MA, USA., pp. 400, 401.
- Jones, S.C., 1971: "A Rapid Accurate Unsteady-State Klinkenberge Permeameter", paper (SPE 3535) first presented at the SPE 46th Annual Fall Meeting, held in New Orleans, Oct. 3-6.
- Kayal, J.R., 2008: "Microearthquake Seismology and Seismotectonics of South Asia", Capital Publishing Co., New Delhi, India., pp. 152-163.
- Kirsch, G., 1898: "Die Theorie der Elastizität und die Bedürfnisse der Festigkeitslehre", Zeitschrift des Vereines deutscher Ingenieure, 42, 797–807
- Lamb, H. 1932: "Hydrodynamics", Cambridge University Press, pp. 738.
- Lay, T., and T.C. Wallace, 1995: "Modern Global Seismology", International Geophysics Series, vol. 58, Academic Press, Inc., San Diego, California, U.S.A.
- Mack, M.G., and N.R. Warpinski, 2000: "Chapter 3: Mechanics of Hydraulic Fracturing", Reservoir Stimulation, 3rd Ed., Edited by Economides and Nolte, Schlumberger Educational Services, Houston, Texas, USA.
- Martin, T. and P. Valkó, 2007: "Chapter 4: Hydraulic Fracture Design for Production

Enhancement”, Modern Fracturing: Enhancing Natural Gas Production, Edited by Economides and Martin, Energy Tribune Publishing, Inc., Houston, Texas, U.S.A.

Matsunaga, I., Kobayashi, H., Sasaki, S. and T. Ishida, 1993: “Studying Hydraulic Fracturing Mechanism by Laboratory Experiments with Acoustic Emission Monitoring”, Int. J. Rock Mech. Min. Sci. & Geomech. Abstr. Vol.30, No. 7, pp. 909-912.

McCabe, W.M., 1978: “Acoustic Emission in Coal: A Laboratory Study”, 2nd Conference on Acoustic Emission/ Microseismic Activity in Geological Structures and Materials – The Pennsylvania State University, November 13 – 15.

Mohr, O., 1900: “What are the Conditions for the Elastic Limit and the Fracturing of a Material?”, Z. Ver. Dt. Ing., 44.

Nordgren, R.P., 1972: “Propagation of a Vertical Hydraulic Fracture”, SPEJ, pp. 306 – 314, Trans., AIME, 253.

Obert, L., 1977: “The Microseismic Method: Discovery and Early History”, Proceedings, First Conference in Acoustic Emission/Microseismic Activities in Geological Structures and Materials, The Pennsylvania State University, June 1975, Trans Tech Publications, Clausthal-Zellerfeld, Germany, pp 11-12.

Ohnaka, M. and K. Mogi, 1981: “Frequency Dependence of Acoustic Emission Activity in Rocks under Incremental, Uniaxial Compression”, Bull. Earthquake Res. Inst. Vol. 56, pp. 67-89.

PAC (Physical Acoustics Corporations), 2004: “AEwin™ Software, User’s Manual, Rev 1.9”, Physical Acoustics Corporations, Princeton, New Jersey, U.S.A. pp 66

- Papanastasiou, P., Thiercelin, M., Cook, J. and D. Durban, 1995: "The Influence of plastic Yielding on Breakdown Pressure in Hydraulic Fracturing", Proc., 35th U.S. Symposium on Rock Mechanics, Reno, Nevada, U.S.A. pp. 281 – 286.
- Parvez, I.A., 2003: "Seismic Sources", available online at http://www.cmmacs.ernet.in/cmmacs/pdf/parvez_lec4.pdf
- Perkin, T.K. and L.R. Kern, 1961: "Widths of Hydraulic Fractures", JPT, pp. 937 – 949, Trans., AIME, 222.
- Pinnacle Technologies, Inc., 2007: "Microseismic Source Mechanisms and Source Parameters", Tech Update, 04 MS.
- Quizix, Incorporated, 1999: "Pump Works User's Manual, Version April 2003", Quizix, Incorporated, North Highlands California, USA.
- Reid, H.F., 1910: "The California Earthquake of April 18, 1906: The Mechanics of the Earthquakes", vol. 2, Carnegie Inst., Washington, D.C.
- Roegiers, J. –C., 2000: "Chapter 3: Elements of Rock Mechanics", Reservoir Stimulation, 3rd Ed., Edited by Economides and Nolte, Schlumberger Educational Services, Houston, Texas, USA., pp. 3.1 – 3.35.
- Sasaki, S., 1998: "Characteristics of Microseismic Events during Hydraulic Fracturing Experiments at the Hijiori Hot Dry Rock Geothermal Energy Site, Yamagata, Japan", Tectonophysics 289 (1998) 171-188.
- Serdyukov, S.V., 2000: "Estimation of Rock Resistance to Hydraulic Fracturing from Data of Laboratory Investigations", Journal of Mining Science, Vol. 36, No. 3.
- Shapiro, S.A., Dinske, C. and E. Rothert, 2006: "Hydraulic-Fracturing Controlled

- Dynamics of Microseismic Clouds”, Geophysical Research Letters, Vol. 33.
- Shearer, P.M., 1999: “Introduction to Seismology”, Cambridge University Press, Cambridge, United Kingdom, pp. 167.
- Sleefe, G.E., Warpinski, N.R. and B.P. Engler, 1995: “The Use of Broadband Microseisms for Hydraulic Fracture Mapping”, paper SPE 26485 first presented at the 1993 SPE Annual Technical Conference and Exhibition held in Houston, Oct. 3-6.
- Sneddon, I.N., 1946: “The Distribution of Stress in the Neighbourhood of a Crack in an Elastic Solid”, Proc. Royal Soc. London, Series A, 187, pp. 229 – 260.
- Sneddon, I.N. and A.A. Elliot, 1946: “The Opening of a Griffith Crack Under Internal Pressure”, Quarterly of Appl. Math. 4, 262 – 268.
- Sondergeld, C.H. and C.S. Rai, 1993: “A new Concept in Quantitative Core Characterization”, The Leading Edge, July, pp. 774 -779.
- Sondergeld, C.H. and L.H. Estey, 1982: “Source Mechanism and Microfracturing during Uniaxial cycling of Rock”, PAGEOPH, Vol. 120.
- Spasova, L.M., and M.I. Ojovan, 2007: “Frequency Characteristics of Acoustic Emission Signals from Cementitious Wastefoms with Encapsulated Al”, Mater. Res. Soc. Symp. Proc. Vol. 985.
- Spottiswoode, S.M. and A. McGarr, 1975: “Source Parameters of tremors in a Deep Level Gold Mine”, Bull. Seismol. Soc. Am. 65: 93 – 112.
- Stein, S. and M. Wysession, 2003: “An Introduction to Seismology, Earthquakes, and

Earth Structure”, Blackwell Publishing Ltd., Malden, MA, pp. 221, 228, 266.

Timoshenko, S.P., and J Guder, 1975: “Theory of Elasticity”, Nauka, Mosco, Russia. pp. 448 – 451.

Warpinski, N.R., 1999, “Hydraulic Fracture diagnostics” paper SPE 36361, Technology Today Series, JPT, October.

Warpinski, N.R., Schmidt, R.A. and D.A. Northrup, 1982: “In Situ Stresses: the Predominant Influence on Hydraulic Fracture Containment”, J. Petrol. Tech., Vol. 34, pp. 653 – 664.

Warpinski, N.R. and L.W. Teufel, 1987: “Influence of Geological Discontinuity on Hydraulic Fracture Propagation”, Journal of Petroleum Technology (February).

Weijers, L., Wright, C.A., Sugiyama, H., Sato, K. and L. Zhigang, 2000: “Simultaneous Propagation of Multiple Hydraulic Fractures – Evidence, Impact and Modeling Implications”, SPE paper 28077.

Zeng, Z. 2002: “Laboratory Imaging of Hydraulic Fractures using Microseismicity”, PHD Dissertation, University of Oklahoma, Norman, Oklahoma, USA., pp. 2, 6-8, 35-44, 86.

APPENDIX A

The procedure for the construction of lower hemisphere focal plots (beach balls) is outlined as follows (Parvez, 2003):

- a. Determine the polarities of P-wave first motion arrival from seismograms at all the stations. Upward break is positive while downward break is negative.
- b. Compute the source-to-station azimuth, α , and the take-off angle, i (as shown in Figure A1) for the seismic P-wave ray leaving the event hypocenter and traveling towards each station. Where the ray intersects the focal sphere from the upper hemisphere, 180° is added to the station azimuth (Aki and Richards, 1980).

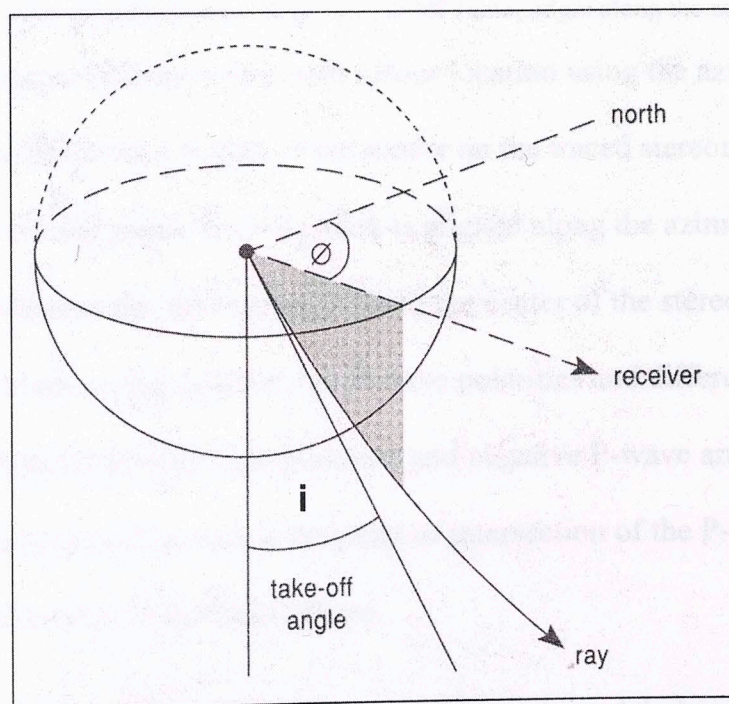


Figure A1: Azimuth and take-off angle of a seismic source with respect to a receiver (sensor).

- c. Set up an equal area stereonet as shown in Figure A2 overlain with a transparent paper pinned to the center of the stereonet. On the transparent paper, trace out the

perimeter of the stereonet and mark off, on the circumference, the North (0°), East (90°), South (180°) and West (270°).

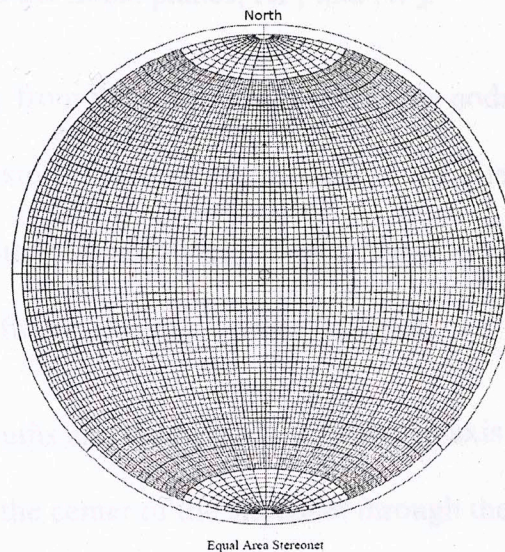


Figure A2: An equal area stereonet. The azimuth is from the 0° (North) to 360° around the stereonet circumference. The take-off angle is from 0° (center) to 90° (outer edge) along the equator (Cronin, 2004).

- d. On the transparent paper, plot each sensor location using the azimuth and take-off angle data. Mark the azimuth of the sensor on the traced stereonet perimeter and rotate the tracing paper until the mark is aligned along the azimuth of 0° , 90° , 180° or 270° . Measure the take-off angle from the center of the stereonet along the azimuth. Mark on this position the P-wave polarities and differentiate between positive P-wave arrivals (compression) and negative P-wave arrivals (dilatation). The position of each sensor is the point of intersection of the P-wave ray with the lower hemisphere of the focal sphere.
- e. Construct two perpendicular great circles known as nodal planes (NP_1 and NP_2) that separate compressional and dilatational marks into four quadrants. One of the nodal planes is the fault plane on which slippage actually occurs while the other is the auxiliary plane which has little significance in fault studies.

- f. Draw another great circle known as the equatorial plane (EP) such that it passes through the poles, P_1 and P_2 , of NP_1 and NP_2 , respectively. The pole, P_3 of EP is at the intersection of the nodal planes, NP_1 and NP_2 .
- g. Along EP, 45° away from the intersection of the two nodal planes and EP, plot the pressure (P) and tension (T) axes in the middle of the dilatational and compressional quadrants, respectively. P-axis points towards the center while the T-axis points away from the center of the stereonet.
- h. Determine the azimuths and plunges of the P- and T-axis. The azimuth is that of the line connecting the center of the stereonet through the P or T points to the perimeter of the stereonet while the plunge is the respective dip angles of the vectors against the horizontal.
- i. Determine the strike angles of nodal planes as measured clockwise against North between the directional vectors connecting the center of the stereonet with the end-point of the projected fault trace lying towards the right of the center of the stereonet.
- j. Determine the dip angles of the nodal planes by putting their projected traces on a great circle and measuring the difference angle, δ , from the outermost great circle.

APPENDIX B

Specifications for 5660B Panametrics-NDT™ wide band pre-amplifiers

- Very low noise (5 μ V peak-to-peak noise referred to the input)
- Ability to drive long coaxial cables – > 500 feet
- Power requirement is 16 +/- 2 volts
- Gain: 40/60 dB
- Bandwidth (-3 dB): 20 – 2000 KHz
- Input Resistance: 1 M ohm
- Input Capacitance: 320 pF
- Output Voltage: 5 V (peak-to-peak)
- Output Impedance: 50 ohms in series with 4.7 F
- Current Consumption: 28 mA
- Operating Temperature: 0 – 50 degree Celsius

This volume is the property of the University of Oklahoma, but the literary rights of the author are a separate property and must be respected. Passages must not be copied or closely paraphrased without the previous written consent of the author. If the reader obtains any assistance from this volume, he must give proper credit in his own work.

I grant the University of Oklahoma Libraries permission to make a copy of my thesis upon the request of individuals or libraries. This permission is granted with the understanding that a copy will be provided for _____ and that requestors will be informed of these restrictions.

NAME _____

DATE _____

A library which borrows this thesis for use by its patrons is expected to secure the signature of each user.

This thesis by IROH ISAAC ASO has been used by the following persons, whose signatures attest their acceptance of the above restrictions.

NAME AND ADDRESS

DATE